SMART SENSING IN ADVANCED MANUFACTURING PROCESSES: STATISTICAL MODELING AND IMPLEMENTATIONS FOR QUALITY ASSURANCE AND AUTOMATION

A Dissertation

by

ZIMO WANG

Submitted to the Office of Graduate and Professional Studies of
Texas A&M University
in partial fulfillment of the requirements for the degree of

DOCTOR OF PHILOSOPHY

Chair of Committee,	Satish T.S. Bukkapatnam
Committee Members,	Yu Ding
	Zhijian Pei
	Wayne NP Hung
Head of Department,	Lewis Ntaimo

August 2020

Major Subject: Industrial Engineering

ABSTRACT

With recent breakthroughs in sensing technology, data informatics and computer networks, smart manufacturing with intertwined advanced computation, communication and control techniques promotes the transformation of conventional discrete manufacturing processes into the new paradigm of cyber-physical manufacturing systems.

The cybermanufacturing systems should be predictive and instantly responsive to incident prevention for quality assurance. Thus, providing viable in-process monitoring approaches for real-time quality assurance is one essential research topic in cybermanufacturing system to allow a closed-loop control of the processes, ensure the quality of products, and consequently improve the whole shop floor efficiency. However, thus far, such in-process monitoring tools are still underdeveloped on the following counts:

- For precision/ultraprecision machining processes, most sensor-based change detection approaches are reticent to the anomalies since they largely root in the stationary assumption whilst the underlying dynamics under precision machining processes exhibit intermittent patterns. Therefore, existing approaches are feeble to detect subtle variations which are detrimental to the process;
- For shaping processes that realize complicated geometries, currently there is no viable tool to allow a noncontact monitoring on surface morphology evolution that measures critical dimensioning criteria in real time.
- For precision machining processes, we aim to present advanced smart sensing approaches towards characterizations of the process, specifically, microdynamics

reflecting the fundamental cutting mechanisms as well as variations of microstructure of the material surfaces.

To address these gaps, this dissertation achieves the following contributions:

- For precision and ultraprecision machining processes, an in-situ anomaly detection approach is provided which allows instant prevention from surface deterioration. The method could be applied to various (ultra)precision processes of which most underlying systems are unknow and always exhibit intermittency. Extensive experimental studies suggest that the developed model can detect in-situ anomalies of the underlying dynamic intermittency;
- For shaping processes that require noncontact in-process monitoring, a vision-based monitoring approach is presented which rapidly measures the geometric features during forming process on sheet-based workpieces. Investigations into laser origami sheet forming processes suggest that the presented approach can provide precise geometric measurements as feedback in real time for the control loop of the sheeting forming processes in cybermanufacturing systems.
- As for smart sensing for precision machining, an advanced in-process sensing/ monitoring approach [including implementations of Acoustic Emission (AE) sensor, the associated data acquisition system and developed advanced machine/deep learning methods] is introduced to connect the AE characteristics to microdynamics of the precision machining of natural fiber reinforced composites. The presented smart sensing framework shows potentials towards real-time

estimations/predictions of microdynamics of the machining processes using AE features.

ACKNOWLEDGEMENTS

I wish to thank my committee members who were more than generous with their expertise and precious time. I would like to send my deep gratitude to Dr. Bukkapatnam, my advisor and committee chairman for his countless hours of reading, encouraging and most of all patience throughout the entire process. Thank you, Dr. Ding, Dr. Hung and Dr. Pei, for serving on my committee. A special thanks to Dr. Li Zeng who helped to serve as a substitute for the committee member for my proposal.

I would also like to thank my colleagues, department faculty, and staff from the Department of Industrial and Systems Engineering for keeping me motivated and enjoying my time at Texas A&M University. Many thanks to all my friends, including my college classmates, my graduate school friends, and all the friends I met during my Ph.D. program.

At last, I would like to send my deepest gratitude to my loving parents for their encouragement and support.

CONTRIBUTORS AND FUNDING SOURCES

Contributors

This work was supported by a dissertation committee consisting of Professor Satish T.S. Bukkapatnam [advisor], Professor Yu Ding, and Professor Zhijian Pei of the Department of Industrial and Systems Engineering and Professor Wayne Hung of the Department of Engineering Technology and Industrial Distribution.

The analyses and data presented in Chapter III were conducted in part by Vivekananda Kovvuri from the Department of Industrial and Systems Engineering at Texas A&M University as part of the collaboration between Prof. Bukkapatnam and Prof. Hung. The firmware imaged, the software developed and the experiment conducted in Chapter IV were with the collaboration with Mr. Ashif Sikandar Iquebal from the Department of Industrial and Systems Engineering, Dr. Vu Nguyen and Dr. Zhujiang Wang from the Department of Mechanical Engineering and Dr. Woo-Hyun Ko from the Department of Electrical & Computer Engineering at Texas A&M University as part of the collaboration among Prof. Bukkapatnam with Prof. Kumar and Prof. Srinivasa. The experiment conducted and the associated collected data presented in Chapters V & VI were from the collaborative effort of Prof. Bukkapatnam, Dr. Faissal Chegdani, Dr. El Mansori from ENSAM (Arts et Métiers ParisTech) at France, and Dr Bruce Tai from Mechanical Engineering Department at Texas A&M University.

All other work conducted for the dissertation was completed by the student independently.

Funding Sources

Graduate study was supported by the NSF foundation (CMMI-#1432914, CMMI-#1437139, CMMI# 1538501, S&AS: INT #1849085, IIP#1543226 and IIP-#1355765).

TABLE OF CONTENTS

Page

LIST OF FIGURES

Page

LIST OF TABLES

Page

CHAPTER I

INTRODUCTION

Background

The Industry 4.0 essentially cultivates a smart manufacturing platform that revolutionizes the manufacturing infrastructure by digitizing multiple sectors across many integrations within this smart factory, such as material preparing, manufacturing processes, the smart sensing and the integration of big data and/or artificial intelligence (AI) to realize smart and autonomous manufacturing processes as well as smart logistics/ material handling. By the year of 2023, the Industry 4.0 that integrates most advanced computation, communication and control techniques, transforms conventional discrete manufacturing processes into the new paradigm of cyber-physical manufacturing systems, creating market more than 20 billion dollars with a compound annual growth rate (CAGR) of 20% [1, 2].

A cyber-physical system (CPS) allows a process under monitored and controlled with the implementation of computer-based algorithms [3], and the whole system is tightly integrated with Internet for communications with users. The cybermanufacturing systems should be predictive and instantly responsive to incident prevention for quality assurance. Thus, providing viable in-process monitoring approaches for real-time quality assurance is one essential research topic in cybermanufacturing system to allow a closed-loop control of the processes, ensure the quality of products, and consequently improve the whole shop

floor efficiency. However, thus far, such in-process monitoring tools are still underdeveloped.

As the principle foundation in cybermanufacturing systems, the smart sensing bridges the gaps between the traditional machining and cyber physical manufacturing by providing statistical/machine learning approaches to allow a self-recognition, change detection, and closed-loop control of the processes (as shown in Figure I-1), and it has been gaining interests among researchers and industrial [4]. This is mainly due to the dramatic increase in the availability of data from the machine to the enterprise using advanced sensor monitoring techniques. As for various machining processes, different suitable monitoring schemes and associated modeling tools should be provided accordingly. For instance, as for material removal processes, understanding the system dynamics of the process under stable and nonstationary conditions is essential for developing sensor-based modeling approaches to diagnose incipient anomalies that may lead to variations in cutting forces, subsurface damages on machined workpiece.

One related topic for the sensor-based monitoring approaches mainly sit in the ultra-precision machining processes. Level of precision and sensitivity of sensors is one of the main considerations of the sensor-based monitoring scheme. The issue is to not only design an adequate sensor monitoring scheme but also provide effective conversion from signal into useful information that allows detecting in-situ anomalies.

Most conventional sensors may have limited signal-to-noise ratio (SNR) and is insensitive to monitor the subtle variations in cutting processes at ultraprecision level, of which the cutting force is several orders of magnitudes smaller than those in conventional machining processes. Acoustic emission (AE) sensor, on the other side, has high sensitivity required to ultraprecision level for characterizing cutting processes and surface finish as it could gather the elastic stress waves from the plastic deformation during the material removal process at ultraprecision level.

However, thus far, most sensor-based change detection approaches that are largely rooted in the stationary assumption are reticent to the anomalies since the underlying dynamics of AE signals under ultraprecision machining processes (UPM) and chemical mechanical planarization (CMP) exhibit intermittent patterns. Therefore, existing approaches are feeble to detect subtle variations which are detrimental to the process. Therefore, an in-situ anomaly detection approach is needed to enable instant prevention from surface deterioration. The method should be applied to various (ultra)precision processes of which most underlying systems are unknown and always exhibit intermittency.

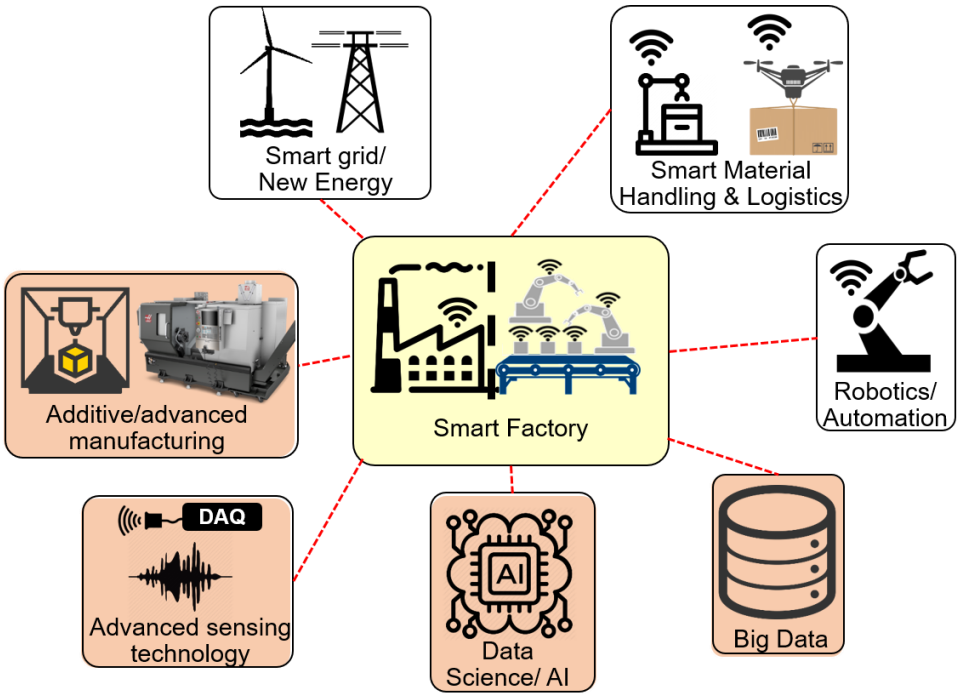

Figure I-1. Smart manufacturing for Industry 4.0.

Other than material removal mechanism, processes such as laser bending processes apply defocused laser ray on sheet-form workpiece to initiate thermal-plastic deformation. Such processes require non-contact sensing schemes for monitoring the workpiece geometric evolution. However, thus far, such a monitoring tool is still underdeveloped. It is necessary to provide an image-based monitoring scheme to capture the workpiece evolution during sheet forming processes and generate real-time quantifiers for surface geometric features as well as the dimension tolerancing.

The final goal is to implement the cyber-physical system into the conventional discrete manufacturing processes, which would demonstrate the merits of

cybermanufacturing platform towards qualification of advanced manufacturing technologies (such as additive manufacturing and laser origami sheet forming) to meet the functionality specified by industry.

Dissertation Structure

The dissertation consists of five papers. The research objectives of the dissertation include the following tasks (which is also summarized in Figure I-2):

1. For ultraprecision machining processes, an in-situ anomaly detection approach needs to be provided which allows incipient anomalies detection for instant prevention from surface deterioration. The method could be applied to various (ultra)precision processes of which most underlying systems are unknow and always exhibit intermittency. Extensive experimental studies suggest that the developed model can detect in-situ anomalies of the underlying dynamic intermittency. A simulation model needs to be presented to capture the dynamics of the ultraprecision machining process (UPM). It suggests that using the in-process monitoring system, the extract features from collected sensor signals could be applied for forecasting the surface finish in real time for ultraprecision machining processes[5-8];

2. For sheet forming processes that require noncontact in-process monitoring, a vision-based monitoring approach should be presented to rapidly measure the geometric features during forming process on sheet-based workpieces. Investigations into applications of real processes such as laser origami sheet forming should be conducted to demonstrate that the presented approach can provide precise geometric

measurements as feedback in real time for the control loop of the sheeting forming processes in cybermanufacturing systems [9, 10];

3. For the micromilling processes, the surface characterizations based conventional prediction model fails to capture the variations of the surface characteristics. Experimental investigations into micromilling processes suggest that the finished surface deteriorates due to multiple effects, of which the build-up edge (BUE) on the smeared surfaces plays a significant role on such surface variations[11]. An image-based approach is therefore needed to 1) capture the BUE on the surface finish, 2) provide a quantitative analysis based on captured surface morphology with BUE, and 3) extract valid features from images and integrate them into the prediction approach to allow an accurate estimation of the surface characteristics;

4. The implementation of the real-time monitoring and control approaches into smart manufacturing systems needs to be provided for demonstration the capability of the smart sensing in several cybermanufacturing applications [12];
5. The smart sensing configurations along with the implemented advanced machine learning and deep learning approaches for characterizations of the manufacturing processes for novel composite materials (i.e., natural fiber reinforced composites) [13, 14].

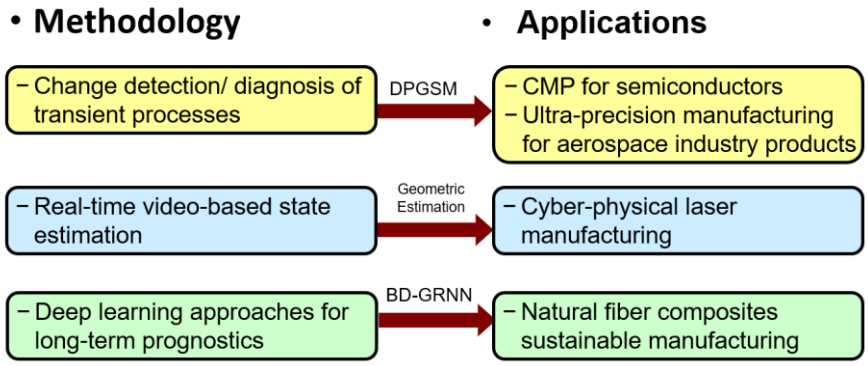

Figure I-2. A schematic diagram listing all research objectives for both methodology and application merits.

The remaining chapters of this dissertation are organized as follows: in Chapter 2, we present an advanced nonparametric approach of anomalies detection for quality assurance in ultraprecision manufacturing processes. Chapter 3 includes a comprehensive study of micromilling process and presented image-based analytic framework towards characterizations of the subsurface deterioration due to the emergence of the build-up edge (BUE) during micromilling. Next, Chapter 4 reviews current status of vision-based monitoring scheme and presents the vision-based monitoring approach for assuring quality in real time for origami bending processes. Chapters 5 and 6 include the implementation of Acoustic Emission sensors into the real-time monitoring on the fiber reinforced composite cuttings using presented machine learning (and deep learning) approaches to connect the AE characteristics to the different failure modes in the cutting mechanisms. Extensive experimental investigations show potentials towards characterizing the

subsurface finish as well as microstructure using smart AE sensing approaches. Finally, a summary of the contributions for this dissertation is provided in Chapter VII.

References

[1] Kim, K.-D., and Kumar, P. R., 2012, "Cyber–physical systems: A perspective at the centennial", Proceedings of the IEEE, **100**, pp: 1287-1308.

[2] Lee, J., Bagheri, B., and Jin, C., 2016, "Introduction to cyber manufacturing", Manufacturing Letters, **8**, pp: 11-15.

[3] Monostori, L., 2014, "Cyber-physical production systems: Roots, expectations and R&D challenges", Procedia CIRP, **17**, pp: 9-13.

[4] Jeschke, S., Brecher, C., Meisen, T., Özdemir, D., and Eschert, T., 2017, "Industrial internet of things and cyber manufacturing systems", Industrial internet of things, Springer, Cham, pp: 3-19.

[5] Wang, Z., Bukkapatnam, S. T. S., Kumara, S. R. T., Kong, Z., and Katz, Z., 2014, "Change detection in precision manufacturing processes under transient conditions", CIRP Annals - Manufacturing Technology, **63**(1), pp: 449-452. http://dx.doi.org/10.1016/j.cirp.2014.03.123.

[6] Wang, Z., and Bukkapatnam, S. T., 2018, "A Dirichlet process Gaussian state machine model for change detection in transient processes", Technometrics, **60**(3), pp: 373--385. https://doi.org/10.1080/00401706.2017.1371079.

[7] Iquebal, A. S., El Amri, S., Shrestha, S., Wang, Z., Manogharan, G. P., and Bukkapatnam, S., 2017, "Longitudinal milling and fine abrasive finishing operations to improve surface integrity of metal am components", Procedia Manufacturing, **10**, pp: 990-996.

[8] Cheng, C., Wang, Z., Hung, W., Bukkapatnam, S. T., and Komanduri, R., 2015, "Ultra-precision machining process dynamics and surface quality monitoring", Procedia Manufacturing, **1**, pp: 607-618.

[9] Wang, Z., Iquebal, A. S., and Bukkapatnam, S. T., 2018, "A vision-based monitoring approach for real-time control of laser origami cybermanufacturing processes", Procedia Manufacturing, **26**, pp: 1307-1317.

[10] Iquebal, A. S., Wang, Z., Ko, W.-H., Wang, Z., Kumar, P., Srinivasa, A., and Bukkapatnam, S. T., 2018, "Towards realizing cybermanufacturing Kiosks: quality assurance challenges and opportunities", Procedia Manufacturing, **26**, pp: 1296-1306.

[11] Wang, Z., Kovvuri, V., Araujo, A., Bacci, M., Hung, W., and Bukkapatnam, S., 2016, "Built-up-edge effects on surface deterioration in micromilling processes", Journal of Manufacturing Processes, **24**, pp: 321-327.

[12] Botcha, B., Wang, Z., Rajan, S., Gautam, N., Bukkapatnam, S. T., Manthanwar, A., Scott, M., Schneider, D., and Korambath, P., 2018, "Implementing the transformation of discrete part manufacturing systems into smart manufacturing platforms", Proc. of ASME

2018 13th International Manufacturing Science and Engineering Conference, College Station, Texas, USA, American Society of Mechanical Engineers Digital Collection.

[13] Wang, Z., Chegdani, F., Yalamarti, N., Takabi, B., Tai, B., Mansori, M. E., and Bukkapatnam, S. T., 2020, "Acoustic Emission (AE) characterization of natural fiber reinforced plastic (NFRP) composite machining using a random forest machine learning model", Journal of Manufacturing Science and Engineering, **142**(3), pp: 031003.

[14] Wang, Z., Dixit, P., Chegdani, F., Takabi, B., Tai, B. L., El Mansori, M., and Bukkapatnam, S., 2020, "Bidirectional Gated Recurrent Deep Learning Neural Networks for Smart Acoustic Emission Sensing of Natural Fiber–Reinforced Polymer Composite Machining Process ", Smart and Sustainable Manufacturing Systems (In press). https://doi.org/10.1520/SSMS20190042.

CHAPTER II

A DIRICHLET PROCESS GAUSSIAN STATE MACHINE MODEL FOR CHANGE DETECTION IN TRANSIENT PROCESSES[1]

Preface

The ability to detect incipient and critical changes in real world processes—essential for system integrity assurance—is currently impeded by the mismatch between the key assumption of stationarity underlying most change detection methods and the nonlinear and nonstationary (transient) dynamics of most real-world processes. The current approaches are slow or outright unable to detect qualitative changes in the behaviors that lead to anomalies. We present a Dirichlet process Gaussian state machine (DPGSM) model to represent dynamic intermittency, which is one of the most ubiquitous real-world transient behaviors. The DPGSM model treats a signal as a random walk among a Dirichlet process mixture of Gaussian clusters. Hypothesis tests and a numerical scheme based on this nonparametric representation were used to detect subtle changes in the transient (intermittent) dynamics. Experimental investigations suggest that the DPGSM approach can consistently detect incipient, critical changes in intermittent signals some 50-2000 ms (20-90%) ahead of competing methods in benchmark test cases as well as a variety of real-

[1] Reprinted with permission from "A Dirichlet process Gaussian state machine model for change detection in transient processes" by Z. Wang and S.T.S. Bukkapatnam, Technometrics, 2018, 60 (3): 373-385, Copyright [2018] by Taylor & Francis.

world applications, such as in alternation patterns (e.g., ragas) in a music piece and vibration signals capturing the initiation of product defects in an ultra-precision manufacturing process.

Introduction

Fast and accurate detection of incipient anomalies, such as damage in machinery and other physical systems, as well as pathological states in natural processes can allow timely intervention to prevent catastrophes [15]. Automated change detection methods employed currently for anomaly detection overwhelmingly assume the non-anomalous "regular" behavior to be (reduced to) a stationary process. Change detection involves testing a hypothesis on the parameters θ of the distribution or some other quantifiers of the stochastic process underlying the measured signals (e.g., H_o: $\theta = \theta_o$ against $H_a : \theta \neq \theta_o$). For example, θ can connote a parameter of an underlying probability distribution, such as mean, μ, or standard deviation, σ, of a Gaussian distribution, or a model parameter, such as a coefficient of a classical time series (e.g., an autoregressive in- tegrated moving average, ARIMA) model. However, real-world processes are often not in a steady state. They operate in a transient state, i.e., θ varies over time. Many of these processes, when considered over long time horizons can be assumed to be stationary [16]; however, anomalies and faults can occur when the system operation shifts from one such transient phase to another. The change points in such systems are, there- fore, not transition points

between two steady states or nary behaviors but between two transient phases, one capturing "normal" behavior (which can be assumed to be near- stationary when large time series samples are considered) before the anomaly or a fault sets in, and the other that can lead to a new abnormal, faulty, pathological, or otherwise anomalous behavior. For example, the first transient phase near a change point $t^* = 3127$ may consist of an AR(1) process with time varying coefficient $\varphi_t = \left(1 - 0.5cos\left(\frac{16t}{1024}\right)\right)$, and the process transitions due to the inception of an anomaly to the second transient phase, which is another AR(1) process with $\varphi_t = \left(1 - 0.5\ cos\left(\frac{8t}{1024}\right)\right)$.

As the current change detection methods are largely rooted in the stationarity assumption, they can only detect well-developed changes (i.e., over long time scales where consistency conditions for the estimates of θ are not violated) and are slow to detect incipient anomalies. Hence, considering the transient phases that separate the two behaviors will help reveal the change much earlier than when the system settles down into a normal behavior where the stationarity assumption holds.

$$dx/dt\ = F(x, \Xi, \epsilon) \tag{1}$$

that specifies the evolution of the state $x(t)$ from an initial condition $x(0)$. Here, Ξ is the process parameter vector, and ϵ is the system noise. The time series signal $y(t)$ gathered from this dynamic process is a function of the state $x(t)$; i.e., $y = \mathcal{F}(x)$. It must be noted that the system begins its evolution from an initial condition almost

always under transient (nonstationary) conditions. It evolves through a series of transient phases before asymptotically executing a stationary, steady state behavior [17].

The process is in a transient phase if $y(t)$ exhibits time-varying behaviors, such as varying moments, piecewise or modulated stationarity or a specific pattern (e.g., periodic or asymmetric cycling) of gradual or abrupt variations [17, 18]. The paucity of change detection methods for a transient process may be due to the challenges associated with quantifying the diverse forms of transient phases. For instance, detecting changes in first-order moments such as in mean shifts, shifting trendlines, and seasonality (e.g., Figure II-1 (a)) has received notable attention (e.g., Montes De Oca et al. in [19]). Last and Shumway [20] studied changes in the patterns of the time-varying covariance function, such as those induced when a modulated AR(1) process $x_t = \varphi_t x_{t-1} + \epsilon_t$, where $\varphi_t = \left(1 - 0.5 \cdot cos\left(\frac{6t}{1024}\right)\right)$ changes to an AR(2) process $x_t = \varphi_t \cdot x_{t-1} - 0.81x_{t-2} + \epsilon_t$ at $t = 666$ time units, as shown in Figure II-1 (b). Choi et al. [21] investigated the detection of changes in additional time-varying patterns, such as in an AR(1) process with slow time-varying coefficient $\varphi_t = 1.8[\frac{exp(50(t-512)/1024)}{1+\exp(50(t-512)/1024)} - \frac{1}{2}]$ at $t = 512$ time units, as in Figure II-1 (c). Some recent investigations on detecting changes under certain elementary forms of transients marked by shifting trends and periodicity, as well as piecewise constant and modulated

covariance structures have been reported [19, 21-24]. These limited representations of multifarious nonstationary behaviors impede timely detection of critical changes in many real-world systems.

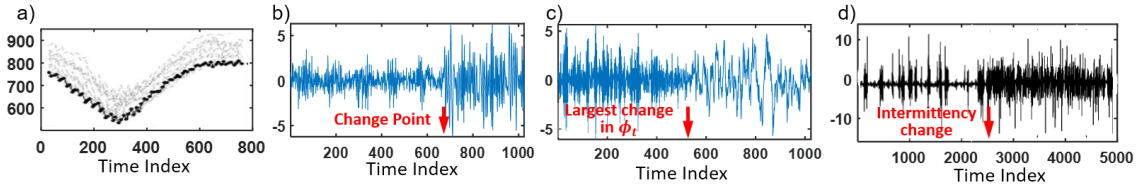

Figure II-1. Representative time-series traces showing different types of transient behaviors: a) drifting trendlines, b) modulated AR process, c) slow time-varying AR processes and d) (on-off type) intermittency [25].

Intermittency is one of the most common transient behaviors exhibited by real-world systems. Many complex nonstationary real-world behaviors, such as the evolution of financial prices, machine vibrations, and the biological processes that are not reducible to simple variations in the first few moments (e.g., trend, heteroskedasticity and seasonality), may be adequately described in terms of intermittency [26, 27]. Intermittency consists of irregular alternation of dynamic behaviors [28]as shown in Figure II-1 (d). This phenomenon has been studied extensively in the context of fluid flows near laminar-turbulence transitions. The behavioral regimes and their sojourn times are known to change, often dramatically, as the Reynold's number of the flow edges towards the transition point [29](Genc et al. 2012). None of the contemporary methods has been

reported to reliably detect such changes in the intermittency dynamics in real time from measured signals.

Although the engineering literature on this topic is fairly sparse, representation of simple forms of intermittencies, such as on-off and in-out, that exhibit multiple near-stationary regimes has received some attention in the dynamic systems theory literature [30-32](Wang 1989; Isola 1999; Sturman and Ashwin 2004). For example, a Markov transition matrix was employed to model a particular instance of intermittency [32](Sturman and Ashwin 2004). Similar representations have also been considered to capture transitions among well-defined finite states (e.g., the governing difference/differential equations are known) [18, 33, 34]. However, the larger issues of how to identify and quantify the stationary sets and transitions using time series data gathered from transient processes and develop suitable hypothesis tests for change detection remain to be addressed.

Intuitively speaking, change detection in an intermittency process is akin to discerning changes in music patterns, especially in note progressions. As can be gathered from the following sections, such changes can hardly be detected with traditional or contemporary methods, including those considered recently for detecting changes in near-stationary processes [20, 35].

We present a nonparametric Bayesian approach based on representing the transient stochastic process underlying measured time series data as a random,

Dirichlet process mixture of Gaussian clusters [36], with a specified nonlinear stationary process determining the internal evolution within each cluster. A Markov transition matrix is specified to determine the stationary transition between clusters. This representation, henceforth referred to as a Dirichlet process mixture of Gaussian state machine (DPGSM) can capture complex steady states (stationary behaviors) as well as various forms of intermittency and it is conducive to developing strategies for change detection.

We also present theoretical results that form the basis for a procedure to fit a DPGSM model to limited real-world data, and report the application of the model to capture transitions in real-world processes not discernible using the conventional and contemporary models tested. Apart from benchmark test cases, the performance of the approach was evaluated for detecting subtle changes in music pattern alternation, specifically transitions between two ragas in the Indian music system that have identical sets of notes and differ only in the alternation rules. The results indicate that only the DPGSM approach was able to consistently detect the changes with low latency. These results provide a theoretical basis and improve upon an earlier study that focused on the application of a similar approach to manufacturing process quality monitoring [5]. Experimental investigations also suggest that microscopic-scale defects on components created during ultra-precision manufacturing processes and not

identifiable using other competing methods can be detected 20-90% earlier than with other methods tested.

The remainder of this chapter is organized as follows: Sec.2 presents the DPGSM representation and change detection approach for intermittent processes followed by the investigations of parameter selection and change-detection performance; Sec.3 contains the results from various applications, including numerical test cases, music pattern changes and incipient anomaly detection in manufacturing processes; conclusions are presented in Sec.4.

Methodology

DPGSM Model

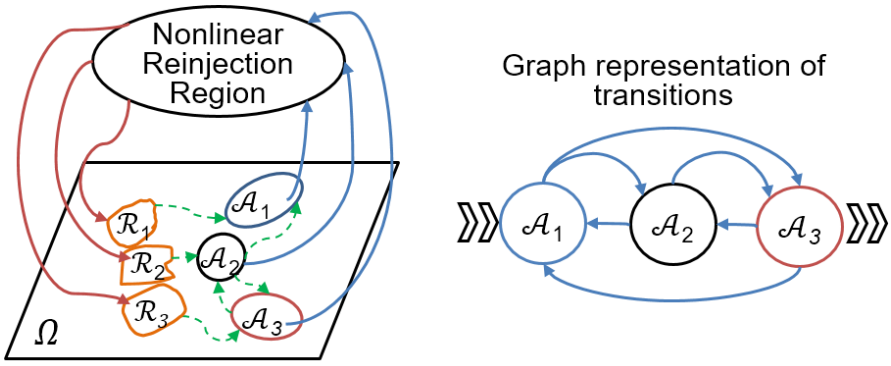

Figure II-2. Schematic diagram of an in-out dynamic intermittency [32]. $\boldsymbol{\Omega}$ is a linear subspace of a smooth map $\boldsymbol{\mathcal{F}}$. Any non-minimal attractor can be decom- posed into attracting subsets $\{\boldsymbol{\mathcal{A}_1}, \boldsymbol{\mathcal{A}_2}, \ldots\}$ and a set of repelling segments $\{\boldsymbol{\mathcal{R}_1}, \boldsymbol{\mathcal{R}_2}, \ldots\}$. The dotted lines represent trajectories of near-stationary sets within $\boldsymbol{\Omega}$. The nonlinear reinjection region completes the attractor as a 3-in and 3-out intermittent process. (reprinted with permission)

An intermittent process is characterized by finite-time sojourns of system trajectories in the state space about multiple *attractors* (i.e., stationary sets that cannot be decomposed into subsets with invariant non-negative measures). As noted in Figure II-2, a class of intermittency dynamics can be viewed as an intersection of attractor $\mathcal{A}$ and a linear subspace Ω. The intersect consists of multiple subsets $\mathcal{A}_k \subset \mathcal{A}$ with invariant measures such that they are attracting within Ω but transversely unstable and, similarly, multiple repelling subsets $\mathcal{R}_k$ (unstable within Ω but transversely stable). It

must be noted that the evolution of the trajectories in an attractor embedded in a d-dimensional state space [the embedding dimension d is usually estimated using the false nearest neighbor criterion [37, 38]] is a topological d-Markov process [39]. Consequently, the finite-time sojourns about, and transitions of the system trajectories over, the multiple attracting subsets can be represented as a Markov transition matrix [18, 33, 34].

For example, let us consider a simpler (reduced) case of intermittent behavior (known as Type 1 intermittency) given by a one-period Poincaré circle map [40]:

$$\begin{bmatrix} x_1(i+1) \\ x_2(i+1) \end{bmatrix} = \left\{ [V_{31} \quad V_{32}] \cdot \begin{bmatrix} x_1(i) \\ x_2(i) \end{bmatrix} + \begin{bmatrix} V_{13} \\ V_{23} \end{bmatrix} \right\}^{-1} \cdot \left\{ \begin{bmatrix} V_{11} & V_{12} \\ V_{21} & V_{22} \end{bmatrix} \cdot \begin{bmatrix} x_1(i) \\ x_2(i) \end{bmatrix} + \begin{bmatrix} V_{13} \\ V_{23} \end{bmatrix} \right\} \tag{2}$$

where the matrix V is defined as:

$$V \coloneqq \begin{bmatrix} v_1^2 - v_1 v_2^2 & -v_2^2 & v_1^2 v_2 - v_1 v_2 \\ 2v_1 v_2^2 - v_1^2 v_2^2 & v_1^2 - v_1 v_2^2 & v_1^3 v_2 - v_1^2 \\ v_1^2 v_2 + v_2^3 - v_1^3 v_2 & v_1 v_2 - v_1^2 v_2 & v_1^4 - 2v_1 v_2^2 \end{bmatrix} \tag{3}$$

such that v_1 :=sinh ζ and v_2 :=cosh ζ. Figure II-3 (a,b) show the phase portraits $\{\boldsymbol{x}(0), \boldsymbol{x}(1), \boldsymbol{x}(2), \dots\}$ generated from Eqs.(2 and 3) for ζ= 1.39 and 1.4, respectively (Liu 2007). This change is equivalent to a transition from a turbulent phase with power law coefficient κ = 1.012 to one with κ= 0.729 [25]. The points in the state space are marked with 8 distinct colors; each represents a cluster of (possibly singleton)

attracting sets. The system exhibits intermittency under both values of ζ although the patterns in the phase portraits are different.

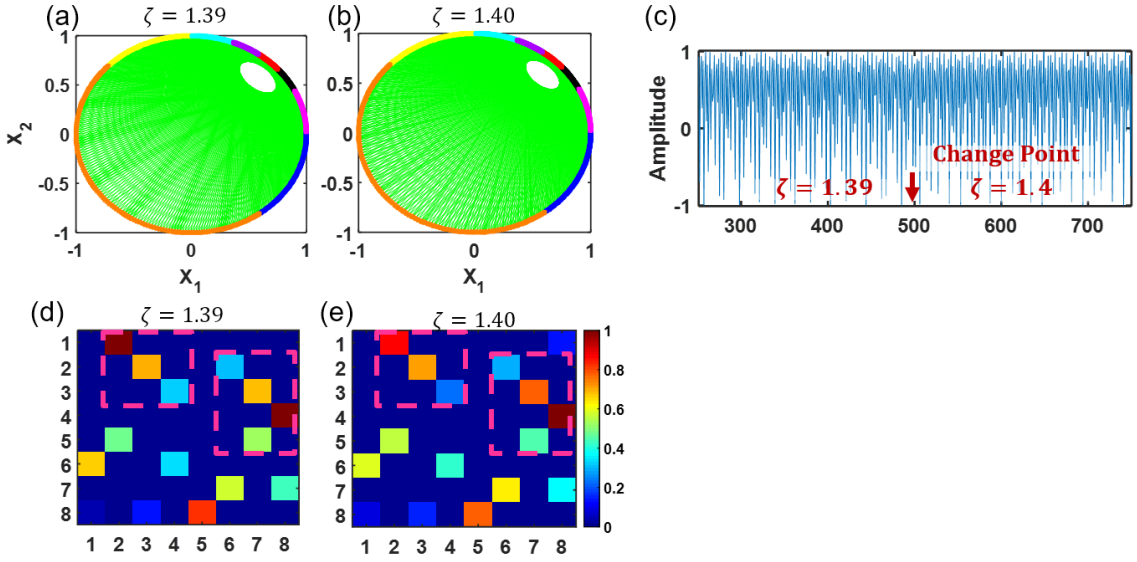

Figure II-3. Phase portraits of a circular iterative map (Liu 2007) at two different settings of a model parameter, (a) ζ=1.39 and (b) ζ =1.40 showing distinct differences in the intermittent patterns. The green lines indicate the trajectory of the map, and the colors along the perimeter of the circle denote clusters (in this case data points were clustered based on the *K* -means clustering technique). (c) Time portraits of $x_1(i)$ from the process in (a) juxtaposed with the process in (b), suggesting that the patterns at ζ=1.39 and 1.40 are not easy to distinguish in the time domain (and using contemporary change detection techniques). (d) & (e) are the Markov matrix representations of the transitions between clusters. (reprinted with permission)

The time series outputs from such intermittencies may be conveniently represented as a stochastic process $x_i|\theta_{c_i} \sim \mathcal{N}\left(\cdot\,\middle|\,\theta_{c_i}\right)$ with $c_i \sim CRP(\vartheta, c_{-i})$, where (c_i) is a random

sequence representing the "cluster" to which x_i is associated, θ_{c_i} is the parameter set of cluster c_i, and ϑ is the concentration parameter. The clusters are drawn according to a so-called Chinese restaurant process (CRP, a variant of the Dirichlet process), such that for any C previously realized clusters, we have the prior distribution as $P\ (c_i = k \leq C|c_{-i}) \propto \frac{I_k}{i-1+\vartheta}$ and $(c_i = k \leq C+1\ |c_{-i}) \propto \frac{\vartheta}{i-1+\vartheta}$, where the subscript $-i$ denotes the set $\{1, 2, \ldots, i\ -\ 1\}$, and I_k is the count of the realized $x - i$ assigned to cluster k (MacEachern and Mu¨ller 1998). Equivalently, the parameters of every Gaussian cluster are given by $\theta_c \sim G$ where $G \sim DP(\vartheta, G_0)$ is a random distribution drawn according to a Dirichlet process (*DP*) with a base measure G_0.

The posterior distribution for the clusters was estimated using a Gibbs sampling scheme [41] by noting that

$$P\big(c_i = k\big|c_{-i}, (x_i)\big) \propto I_k^- \phi(x_i|\theta_k), \text{ for } k = 1,2, \ldots, C$$

$$P\big(c_i = k\big|c_{-i}, (x_i)\big) \propto \vartheta \int \phi(x_i|\theta_k) dG_0(\theta) \quad (4)$$

where I_k^- represents the number of elements in cluster k when the observation x_i is removed; $\varphi(x_i|\theta_k)$ is the Gaussian likelihood of x_i with parameter $\theta = \{\mu, \Sigma\}$. Also, we define a transition matrix $\boldsymbol{\Pi} = \begin{bmatrix} \pi_{11} & \cdots & \pi_{1K} \\ \vdots & \ddots & \vdots \\ \pi_{K1} & \ldots & \pi_{KK} \end{bmatrix}$ among $k\ =\ 1, 2, \ldots K\ \leq\ C$ prominent clusters (i.e., states) such that each element π_{jk} presents the probability that the time

series data at time step i in state j, will move to cluster k at step $i+1$. Thus, π_{jk} at time step t can be estimated as [42]

$$\pi_{jk} = \frac{\sum_{i=1}^{N-1} P(c_i = j|x_i, \theta_j) P(c_{i+1} = k|x_{i+1}, \theta_j)}{\sum_{i=1}^{N-1} P(c_i = j|x_i, \theta_j)} \tag{5}$$

It may be noted that for each row of a transition matrix, we have $\sum_k \pi_{jk} = 1$. Also, the count vector z_j of transition samples from cluster j to every cluster (including itself) follows a multinomial distribution with the parameter vector $\boldsymbol{\pi_j} = \{\pi_{j1}, \pi_{j2}, \dots, \pi_{jk}\}$ [43]. Consequently, the Bayesian posterior distribution of the vector π_j for the counts $z_j^{(t)}$ up to time t may be stated as follows:

Proposition 1. *The Bayesian posterior distribution of row vector π_j for a given $\boldsymbol{z}_j^{(t)}$ follows a Dirichlet distribution, i.e. $Dir\left(z_{j1}^{(t)}, z_{j2}^{(t)}, \dots, z_{jK}^{(t)}\right)$:*

$$f\left(\boldsymbol{\pi}_j|\boldsymbol{z}_j^{(t)}\right) = \frac{1}{B(\boldsymbol{z}_j^{(t)})} \prod_{k=1}^{K} {\pi_{jk}}^{z_{jk}^{(t)}-1};\ B\left(\boldsymbol{z}_j^{(t)}\right) = \frac{\prod_{k=1}^{K} \Gamma(z_{jk}^{(t)})}{\Gamma(\sum_{k=1}^{K} z_{jk}^{(t)})} \tag{6}$$

Again, $\boldsymbol{z}_j^{(t)}$ can be updated as

$$z_{jk}^{(t)} = \sum_{i=t-L+1}^{t-1} P(c_i = j|x_i, \theta_j) \cdot P(c_{i+1} = k|x_{i+1}, \theta_j) + w_{jk} \tag{7}$$

where we set ω_{jk} as 1 for a non-informative prior, and L is the window length employed. The distribution of elements π_{jk} is given by the following result:

Proposition. *Individual* π_{jk} *follows a marginal beta distribution* $Beta(z_{jk}^{(t)}, \sum_{h\neq k} z_{jh}^{(t)})$*, i.e.*

$$Beta\left(\pi_{jk}\middle|\boldsymbol{z_j}^{(t)}\right) = \frac{\Gamma\left(\sum_k z_{jk}^{(t)}\right)}{\Gamma\left(z_{jk}^{(t)}\right)\Gamma\left(\sum_{h\neq k} z_{jh}^{(t)}\right)}\ \pi_{jk}^{z_{jk}^{(t)}-1}(1-\pi_{jk})^{\sum_{h\neq k} z_{jh}^{(t)}-1} \tag{8}$$

Pertinently, Figure II-3 (d) and (e) show the (color coded) Markov transition matrices $\widetilde{\Pi}$ the processes presented in Figure II-3 (a) and (b), respectively. The time portrait in Figure II-3 (c) consists of 500 data points from the time series output from process Figure II-3 (a) juxtaposed with 500 points from the time series from process Figure II-3 (b). Remarkably, most of contemporary change detection methods (see Sec.3) failed to detect the transition between the two intermittency behaviors (here, the time step at which the two segments were juxtaposed). The resulting average run length ARL_1 (a measure of the expected latency in detecting a change) was more than 500 time steps. However, the DPSGM was able to capture the change with an ARL_1 of 1.026 time steps as Markov matrices $\widetilde{\Pi}$'s exhibit noticeable differences. This example indicates that the pattern of the estimated matrix $\widetilde{\Pi}$ discern changes in intermittency dynamics.

Change Detection Method

Invoking the uniformly most powerful (UMP) hypothesis test, we have, for every cluster pair j and k, $H_o: \pi_{jk} = \pi_{jk}^0$; $H_a: \pi_{jk} \neq \pi_{jk}^0$, where π_{jk}^0 is the nominal value of a transition matrix element under hypothesis H_o. The null hypothesis, H_0, is rejected if the value of test $\widetilde{\pi}_{jk} = \pi_{jk}|z_j^{(t)} = \frac{z_{jk}^{(t)}}{\sum_{k=1}^{K} z_{jk}^{(t)}}$ does not lie within the interval $\left[F^{-1}\left(\frac{\alpha j}{2};\ z_{jk}^{(t)},\ \sum_{h\neq k} z_{jh}^{(t)}\right), F^{-1}\left(1-\frac{\alpha j}{2};\ z_{jk}^{(t)},\ \sum_{h\neq k} z_{jh}^{(t)}\right)\right]$. $\alpha_j = 1-(1-\alpha)^{\frac{w_j}{K}}$ is the significance level of row j, which is set based on the specification of the family-wise error rate (FWER) α, i.e., $P(rejecting\ at\ least\ one\ H_j | H_j \in H_o) = \alpha$, and $w_j \propto z_j^{(t)}$, the updated counts of each transition matrix row j.

Because of the interdependencies among $\pi_{jk}, k = 1 \ldots K$, the UMP test may lead to excessive type II error. Alternatively, a new statistic may be employed to detect the change in the transition rows under the hypothesis test $H_o: \pi_{jk} = \pi_{jk}^0$; $H_a: \pi_{jk} \neq \pi_{jk}^0$, where π_j^0 is the nominal transition row vector under the null hypothesis. For large n, row-wise distance $d_j^2 = \left(\boldsymbol{\pi_j} - \boldsymbol{\pi_j^0}\right)\boldsymbol{S_j}^{-1}\left(\boldsymbol{\pi_j} - \boldsymbol{\pi_j^0}\right)^{\top}$ follows a chi-square χ_K^2 distribution where S_j is the sample covariance matrix for estimating the true covariance matrix Σ_{π_j} given a large population. A 3σ limits ($\alpha \approx 0.0027$) may be set so that a change in intemittency is deemed wherenever the estimated $\widetilde{\pi_j}$ deviate from their expected values beyond these limits. Even though these 3σ limits usually treat the Gaussian distributed observations,

their setup is reasonable for a non-Gaussian process if the 3σ error is converted into a sequential equivalent: the average run length between false alarms (ARL0). Here $ARL_0 = \frac{1}{\alpha} \approx 370$ as type I error $\alpha \approx 0.0027$ in most cases tested. The overall procedure may be summarized as follows:

•Step 1: Determine DP cluster distributions $P(c_i = k|x_i, \theta_k)$ from Eq.4.

•Step 2: For every time t thereafter, estimate the transition matrix $\widetilde{\Pi}^{(t)}$ from Eq.5.

•Step 3: Set the significance level vector $\alpha = \{\alpha_1, \alpha_2, \ldots, \alpha_K\}$ such that $\alpha_j = 1 - (1 - \alpha)^{\omega_j/K}$ is the significance level of row j.

•Step 4: Calculate the statistic d^2 and the control limits for each row j.

•Step 5: Monitor the process and estimate ARL_1.

Choice of Window Length

The window length L is a crucial parameter that highly affects the change-detection performance of the DPGSM. A proper choice of L is needed to ensure the consistency of the estimator of the transition matrix. In this context, we conducted a numerical study to investigate the convergence rate of the posterior distribution of the DPGSM and provide a statistical scheme to estimate L. We also present numerical studies to evaluate the power of the DPGSM model for change detection.

Convergence rates of the DPGSM model

The convergence rates of posterior Dirichlet mixtures have been studied by multiple research groups [44-48]. The following results, based on [48], provide one of the most conservative convergence rates of the posterior distributions of independent samples of length L drawn from a Dirichlet process mixture of Gaussians:

Proposition 3. *The density ρ of a Dirichlet process mixture of Gaussians converges in probability to the true density p_0 at a rate $\varsigma_L = L^{-\frac{1}{2}}(logL)^{\frac{3}{2}}$, i.e.,*

$$G\left(\{p: \rho_H(p, p0) > M\varsigma_L\} | x_1, x_2, \ldots, x_L\right) \rightarrow 0, \ \forall M > 0 \tag{9}$$

where $\rho_H(p, p_0)$ is the Hellinger distance and $G(.|x_1, x_2, \ldots, x_L)$ denotes the posterior measure estimated with L observations.

However, the actual convergence rate may be highly sensitive to the cluster concentrations and the number of components as well as the dependency among the samples [44]. For example, whenever the clusters are highly concentrated (i.e., high concentration prior), and the number of clusters is < 8, the convergence rates can exceed polynomial rates, and Proposition 3 may offer a loose bound [47, 49] for the convergence rate of a posterior mixture. The effect of window length L on the transition matrix estimation was studied further using the following numerical study, which employed a multi-dimensional time series realized from a DPGSM model such that $x_t \sim \mathcal{N}(\cdot|\theta_{c_t})$.

Two factors, namely, the concentration of the clusters, and the dependency among realized samples, have been considered in this study. The Gaussian covariance was adjusted to change the cluster concentration and study its influence on the convergence rate [44]. The dependency among the samples was adjusted by changing the order of the autoregressive (AR) process generated from the independent sample realization. This study allows us to investigate the convergence rate of posterior Dirichlet with autocorrelated observations.

In the first study, five levels of cluster overlap were investigated. The overlap among clusters was adjusted by scaling the covariance matrix structures on all cluster components. Specifically, DPGSM model $x_t|c_t \sim \mathcal{N}(\cdot|\theta_{c_t})$, where $\theta_{c_t} = \{\mu_{c_t}, \xi \cdot \Sigma_{c_t}\}$ and ξ is the scale factor, contains $K = 5$ clusters. The cluster mean vectors were chosen as, respectively, $\mu_1 = \begin{bmatrix}0\\0\end{bmatrix}$, $\mu_2 = \begin{bmatrix}-3\\-5\end{bmatrix}$, $\mu_3 = \begin{bmatrix}4\\6\end{bmatrix}$, $\mu_4 = \begin{bmatrix}-5\\5\end{bmatrix}$ and $\mu_5 = \begin{bmatrix}4\\-6\end{bmatrix}$. Note that the covariance matrix Σ_j follows an inverse-Wishart distribution, i.e., $\Sigma_j \sim InvWishart(\Psi, \nu)$ with the scale matrix Ψ and degrees of freedom ν. Then the covariance matrices for two different levels of overlap were sampled based on different sets of priors $\{\Psi, \nu\}$.

For each setting of $\xi = \{1, 5, 10, 20, 50, 100\}$, we first simulated a time series of 10,000 data points from the DPGSM and computed the estimation errors in terms of the unscented Hellinger distances $\rho_H(p, p_0)$ [50] between posterior distribution p

given data points within window length L and the true Gaussian mixture p_0. For a given ξ ranging from 1 to 100, we capture multiple conditions of cluster overlaps as shown in Figure II-4. As ξ ranges from 1 to 10, the Gaussian mixtures are well separated but for $\xi \geq 50$, the clusters are highly overlapped. The variations in the estimation errors based on 10 simulations at each setting are summarized in the box plots shown in Figure II-5 . The solid lines represent the two theoretical bounds of the convergence rates- the topline (red) for the polylogarithmic rate and the bottomline (green) for the parametric rate. The dark (black) dashed line connects the average values of the errors at different L using a polynomial interpolation.

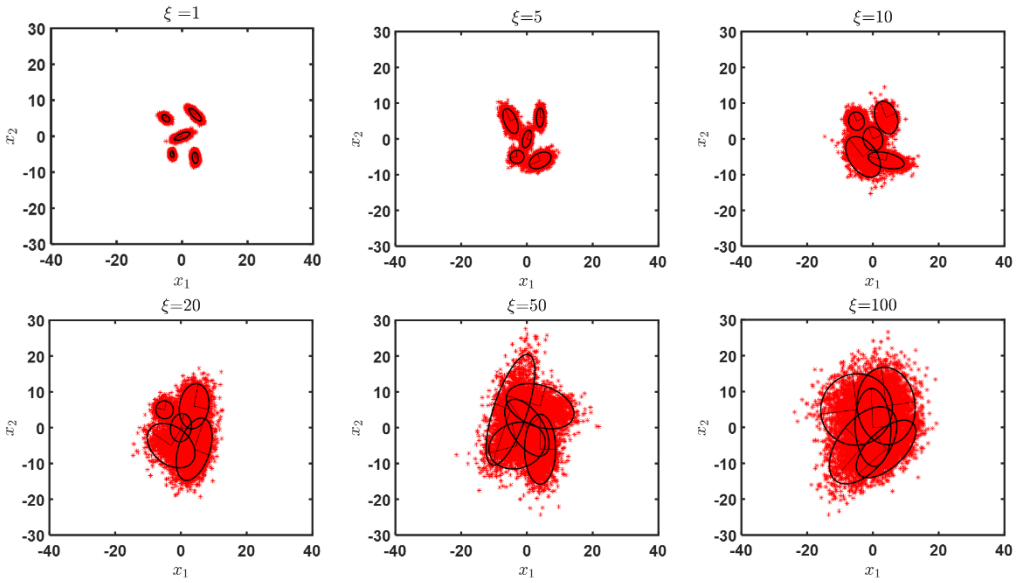

Figure II-4. Scatter plot of a mixture Gaussian model under different levels of noise (ξ ranges from 1 to 100). (reprinted with permission)

One can note that for $\xi < 20$, the convergence follows a parametric rate. For $\xi \in [20, 50]$, the convergence rate is well bounded using the polylogarithmic rate, indicating the robustness of the suggested polylogarithmic rate even when the mixtures are hard to identify. However, when ξ is greater than 50, the uncertainty seems to increase to an extent that for reasonable values of window length L, the convergence rate seems slower than the polylogarithmic rate. In brief, when the mixtures are highly overlapping and Gaussian noise and the time series is overwhelmed by the level of Gaussian noise, the convergence rate is slower than the parametric rate, and the polylogarithmic term might provide a suitable lower bound.

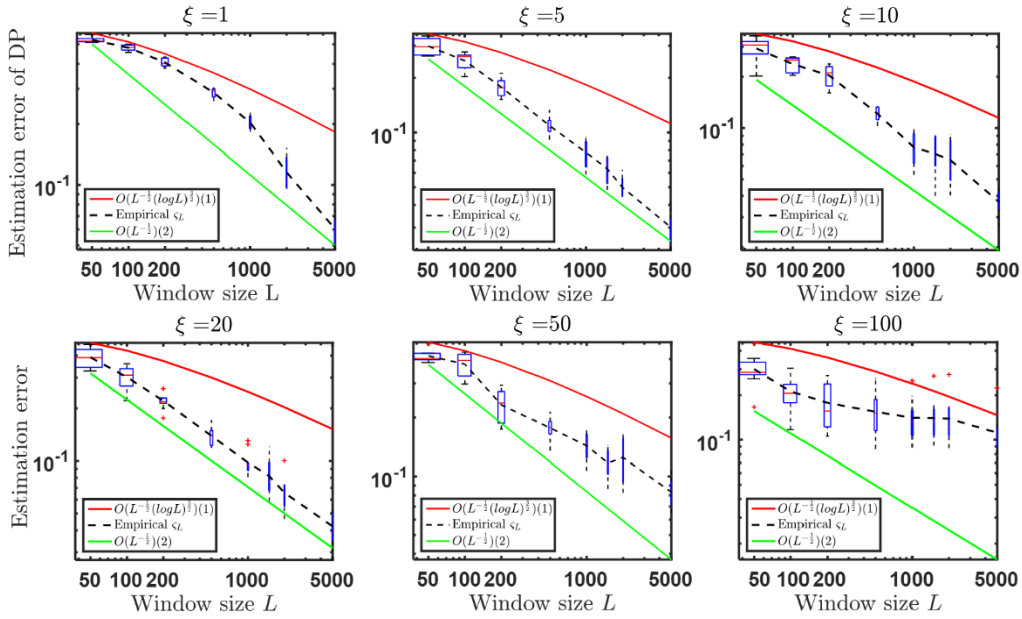

Figure II-5. Comparisons of convergence rates under different levels of Gaussian noise. (reprinted with permission)

The second study investigates the convergence rate of the DPGSM realized with different levels of sample dependency. First, we chose the same distribution parameters as the previous case study: 5 clusters with identical means and priors of covariance matrices. To introduce the dependency in stochastic terms, the time series is realized by the autoregressive (AR) model $y_t = \left(1 + \phi_1 B + \phi_2 B^2 + \ldots + \phi_q B^q\right) x_t + \epsilon_t$ where $x_t | c_t \sim \mathcal{N}(\cdot | \theta_{c_t})$, $\epsilon_t \sim MVN(0, I)$, q is the order and $\{\phi_q\}$ are the coefficients of the AR model. We considered four orders, namely $q = \{1, 2, 5, 10\}$, to investigate the convergence rate under different dependencies.

The variations in empirical convergence rates with L for different AR models are shown in Figure II-6. Since the AR model creates highly concentrated mixtures (each cluster is well separated) with a small component number (as $K = 5$) for all four AR models, the empirical convergence rates, shown as dashed black lines, tend to be close to/bounded by parametric rate $L^{-\frac{1}{2}}$ for $L > 200$. The results also indicate that the asymptotic convergence rates can be higher than the parametric rate. However, as the AR order increases, it takes longer for the convergence rate to reach this level. It may be noted that most real-world systems considered in our case studies contain significant noise, to an extent that the cluster concentrates and hence the convergence rates tend to be much lower. For example, when mixing rates are high with complex correlation structures a more conservative bound of $L^{-\frac{1}{3}}$ may be employed. These

observations open the possibilities for additional theoretical studies on convergence rates of correlated mixture data.

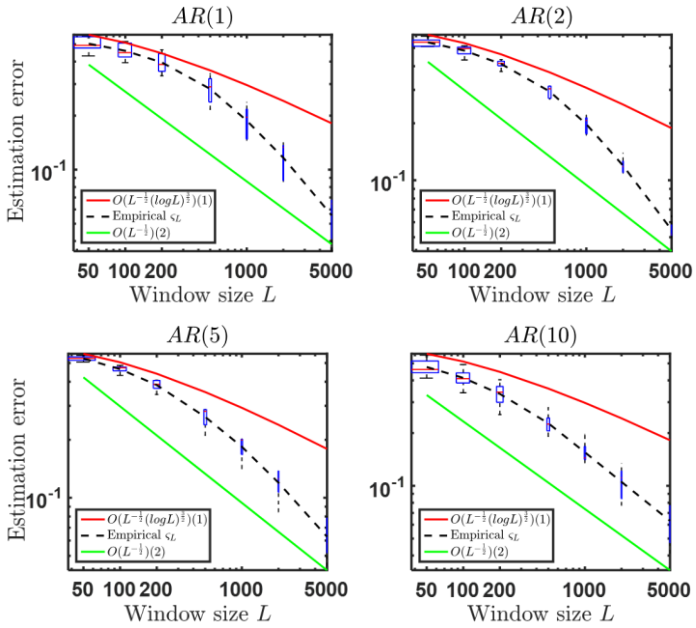

Figure II-6: Comparisons of convergence rates under different AR models. (reprinted with permission)

Asymptotic Property for the Transition Matrix Estimation Errors

For determining window length L based on the foregoing study, we need to express ς_L and L in terms of the specified significance level, α. However, doing so is not straightforward, as p_0 is unknown for the time series samples from most real-world processes. We therefore pursued an alternative approach to select the window length. Here, we define Φ, the vectorized representation of Π such that $\Phi = [\boldsymbol{\pi}_{1.}, \boldsymbol{\pi}_{2.}, \ldots, \boldsymbol{\pi}_{K.}]$ and

$\Delta\Phi = \Phi^{(L)} - \Phi^{(0)}$, where $\Phi^{(L)}$ is the vectorized transition matrix estimated using time series within window length L and $\Phi^{(0)}$ is the vectorized true transition matrix (unknown in most real-world contexts). We also define $Q = \Delta\Phi\Sigma_{\Pi}^{-1}(\Delta\Phi)^{\top}$. For sufficiently large L, we have the following result [42]:

Proposition 4. *As $L \to \infty$, LQ follows a chi-squared distribution, i.e., $LQ \sim \chi^2_{K^2}$.*

Thus, given significance level α and bound q^* for Q, we can specify a lower bound for the window length. The result can be stated as follows:

Proposition 5. *Given $Q = q^*$, we have the lower bound of minimum window length as*

$$\frac{\chi^2_{K^2,\frac{\alpha}{2}}}{q} \leq L_{min} \tag{10}$$

As suggested in Proposition 5, the error between the estimated transition matrix Π and the true transition matrix $\Pi^{(0)}$ expressed as $q = \Delta\Phi\Sigma_{\Pi}^{-1}(\Delta\Phi)^{\top}$ is bounded by $q \geq \frac{\chi^2_{K^2,\frac{\alpha}{2}}}{L}$.

Here Φ is the vectorized row of the transition matrix $\Pi = [\pi_{1.}, \pi_{2.}, \ldots, \pi_{K.}]$ and $\Delta\Phi$ is the error between the estimated transition matrix $\Phi^{(L)}$ using a time series within window length L and the true transition matrix $\Phi^{(0)}$.

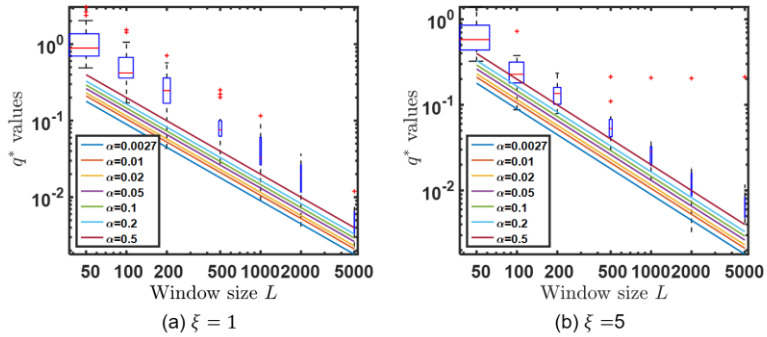

Figure II-7. Boxplots of q's compared with their statistical lower bounds with multiple confidence levels, α's. (reprinted with permission)

However, specifying the bound on $\Delta\Phi\Sigma^{-1}(\Delta\Phi)^{\mathrm{T}}$ is difficult since the value q^* may differ case by case for different values of Σ^{-1}. Instead, the following result provides the bounds on L when the l_2-norm error of the transition matrix is specified:

Proposition 6. *Given $\Delta\Phi(\Delta\Phi)^{\mathrm{T}} \leq \epsilon^*$, the bound for (a) minimum window length is given by*

$$\frac{\chi^2_{K^2,\frac{\alpha}{2}}}{\epsilon^* \cdot \lambda_{max}\left(\Sigma^{-1}\right)} \leq L_{min} \tag{11}$$

where $\lambda_{\max}(\Sigma^{-1})$ represents the largest eigenvalue of Σ^{-1}.

Consistent with Proposition 6, window length L was chosen to be in the range of 500~2000 data points for all investigations reported in the following section. This choice was found to be adequate to ensure convergence (for $\epsilon^* \approx K^2 \times 10^{-4}$) of Π in the DPGSM approach.

To verify the suitability of the propositions, we compute the estimation errors, q's, obtained with 10 simulations with the theoretical lower bounds $\frac{\chi^2_{K^2,\frac{\alpha}{2}}}{L}$ for various α values (see Figure II-7). Evident from the figure, most of the estimation errors $q's$ lie above the lower bounds given $\alpha \approx 0.0027$. Therefore, Proposition 5 provides the valid lower bounds for choosing a proper window length, L.

Power Test

We now present the statistical power of the procedure provided in Sec. 2.2 to detect a change introduced to a DPGSM process. Here, the Markov matrix of DPGSM process $\Pi = \{\pi_j^0\}$ was changed at a certain time t^* to $\Pi^1 = \{\pi_j^1\} = \{\pi_j^0 + \delta_{\pi j}\}$ for $j = 1,2,\ldots,K$. We employed $\delta_q = \sum_{j=1}^{K} \left(\delta_{\pi_j}\right) \Sigma_{\pi_j}^{-1} \left(\delta_{\pi_j}\right)^{\mathsf{T}}$ to signify the extent of this change. For each setting of δ_q, we studied the change detection performance for 100 DPGSM process realizations, each with a randomly chosen setting of ξ as detailed in Sec. 2.3.1. For each realization, we computed both the theoretical and the empirical powers for detecting this change, i.e., to reject K null hypotheses, $H_o \ \pi_j = \pi_j^0;\ j = 1,2,\ldots K$; in favor of $\pi_j = \pi_j^1$. Then, the theoretical power of such an FWER-based hypothesis can be expressed as $1 - \beta(DPGSM) =$ Pr (reject at leat one of the false K null hypothesis) $= 1 - \prod_j^K \beta_j$ where β_j is the row-wise type II error.

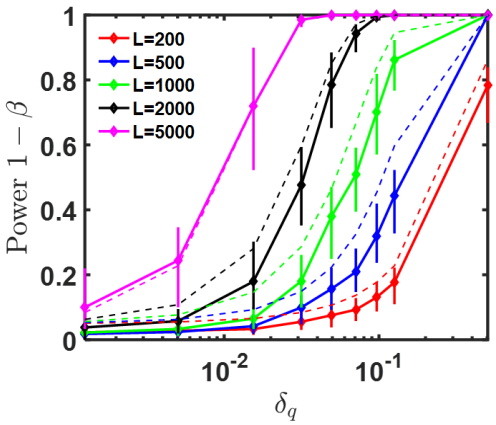

Figure II-8. Empirical test power compared with theoretical power (dashed lines). (reprinted with permission)

It may be noted that the term $L \cdot \left(\widetilde{\pi_j}^1 - \pi_j^0\right)\Sigma_{\pi_j}^{-1}\left(\widetilde{\pi_j}^1 - \pi_j^0\right)^\top$ follows a noncentral chi-squared distribution $\chi_K^2(\lambda_j)$ (Hogg and Craig 1994) with the noncentral parameter $\lambda_j = L \cdot \sum_{k=1}^K \delta_{\pi_{jk}}^2$. Consequently, the overall test power can be formulated as $1 - \prod_j^K \beta_j = 1 - \prod_j^K \Pr\left(L \cdot \left(\widetilde{\pi_j}^1 - \pi_j^0\right)\Sigma_{\pi_j}^{-1}\left(\widetilde{\pi_j}^1 - \pi_j^0\right)^\top \leq \chi_{K,1-\alpha_j}^2\right)$. We conducted a numerical study to observe the variation of $1-\beta$ relative to δ_q with $\alpha = 0.05$ at different choices of window length L to estimate Π^1. Figure II-8records the 25%, 50% and 75% quartiles of empirical powers $1-\hat{\beta}$'s (solid lines) along with those of theoretical powers $1-\beta$'s (dashed lines) for different L's.

The power curves suggest that even under significant overlap among the Gaussian clusters, the empirical estimate $1-\hat{\beta}$ is consistent with the theoretical power $1-\beta$ at all L's. More interestingly, L was a crucial determinant of test power. As L increases the sensitivity approaches 1 at progressively smaller values of δ_q. For example, for $L = 200$, the sensitivity exceeded 0.80 at $\delta_q \approx 0.50$ and for $L = 2000$, it reached the 0.8 at $\delta_q \approx 0.05$. For small values of δ_q and L, the mean sensitivity remains

close to zero, and we did not observe significant sample-to-sample variation in the sensitivity. Similarly, for large L and δ_q, the sensitivity remained close to 1 with little sample-to-sample variation. For intermediate values, however, we observed significant differences in the sensitivity from sample to sample. In general, a large variation in test power estimates $1-\hat{\beta}$'s occurs when the theoretical test power increases sharply as depicted in Figure II-8. This interesting finding may open future investigation into the robustness of DPGSM models.

Implementation Details and Results

The performance of the present approach was evaluated for detecting changes in intermittency patterns introduced in carefully designed numerical experiments, as well as those occurring in complex physical processes, namely music patterns (specifically transitions between *ragas* that use the same scales and notes), and manufacturing machine vibrations. The average run length, ARL_1 was used to compare the performance of the DPSGM with three other change detection methods; namely, a conventional exponential weighted moving average (EWMA), a contemporary parametric wavelet-based SD-WCUSUM (CUSUM control chart on Haar wavelet coefficients) [35], and a piecewise segmentation method [20], which methods have been considered for change detection scenarios involving transients. We did not use computationally intensive hidden Markov models. At the outset, the investigations suggest that our approach allows detection of salient changes in intermittency dynamics not discernible with any other method.

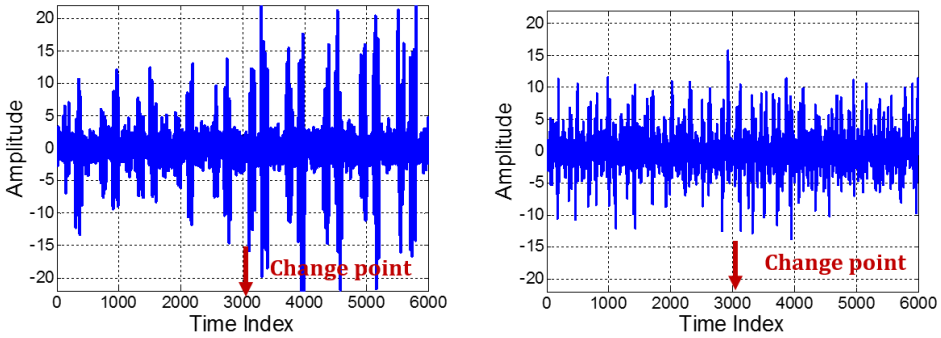

(a) Type A fault: Variance change (b) Type B fault: Sojourn time change

Figure II-9. Traces of piecewise stationary time series data showing two types of changes. (reprinted with permission)

Table II-1: ARL_1 comparisons. (reprinted with permission)

	EWMA	SD-WCUSUM	RNDP	DPGSM
Fault A	25.6	2.5	6.1	3.5
Fault B	Inf	Inf	Inf	3.8

Change Detection for Piecewise Stationary Time Series

We employed a piecewise stationary autoregressive and moving average ARMA(2,1) process $x_i = f_m(x_{-i}; \phi^{(m)}, \psi^{(m)}), i = 1,2,\dots,N$, defined over M time intervals (i_{m-1},i_m), such that i_m, $m = 0,\dots,M$, forms an order statistic sampled from a discrete uniform distribution $UNIF(0,N)$ [51]. The Gaussian noise (shock) process for each interval has a constant variance $a_t \sim N(0, \Delta_m \sigma^2)$, such that $\Delta_{3m+1}= 3$, $\Delta_{3m+2}=4$, $\Delta_{3m+3}=1$. We compared the performances of the DPGSM and the methods mentioned earlier for detecting the following two types of faults introduced at time index i=3000 (see Figure II-9): a Type A fault consists of a change in the variance patterns to $\Delta_{3m+1}=6$,

Δ_{3m+2}=7, Δ_{3m+3}=1, and so on and a Type *B* fault consists of changing the lengths of intervals (i_m, i_{m+1}) to half of their original lengths. The ARL_1 values with various methods for detecting the two faults are summarized in Table II-1. The results suggest that all three methods can detect a Type *A* fault and that ARL_1 are much lower with the DPGSM, RNDP, and SD-WCUSUM methods than with EWMA. For a Type *B* fault, however, only the DPGSM was able to detect the change consistently, with a low ARL_1 of ~ 3.8 time steps.

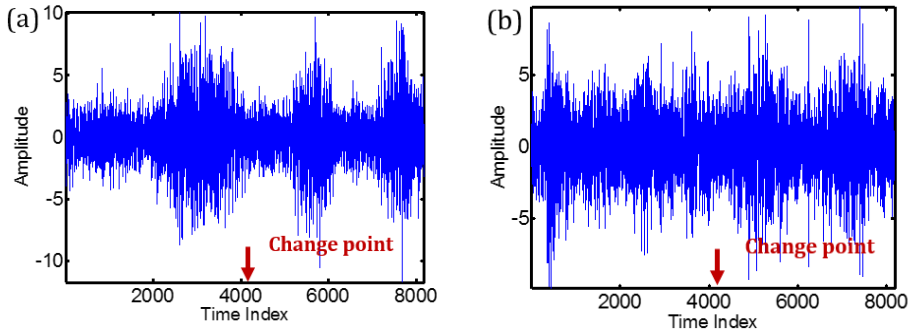

Figure II-10. Time portraits of representative (a) MMA and (b) MAR time series. (reprinted with permission)

Next, we employed the modulated moving average (MMA) and modulated autoregressive (MAR) time series models investigated in [20]. We used $y_t = \varepsilon_t + a_t\varepsilon_{t-1} + 0.5\varepsilon_{t-2}$, as the MMA time series model (See Figure II-10 (a)), where the time-varying coefficient a_t is given by $a_t = 1.122\left(1 - 1.781 \cdot sin\left(\frac{\pi t}{2048}\right)\right)$. A fault was introduced at

time index t=4096 data point by doubling the modulation frequency so that $a_t' = 1.122\left(1 - 1.781 \cdot sin\left(\frac{\pi t}{2048}\right)\right)$.

Similarly, we used $y_t = a_t y_{t-1} - 0.81 y_{t-2} + \varepsilon_t$, with $a_t = \left(1 - 0.5 \cdot cos\left(\frac{4\pi t}{2048}\right)\right)$ as the MAR time series model [20]. A fault was introduced at $t = 4096$ in the form of doubling of the modulating frequency, i.e., $a_t = \left(1 - 0.5 \cdot cos\left(\frac{2\pi t}{2048}\right)\right)$ (See Figure II-10 (b)). We tested the performances of the DPSGM and the other change detection methods, including EWMA and SD-WCUSUM [35], as well as a piecewise stationary segmentation method (henceforth referred to as SKL-Info) reported in [20] using 50 time series realizations of the MMA and MAR processes. SKL-Info uses a symmetrized Kullback-Leibler divergence statistic that quantifies changes in the frequency spectral distribution for change detection.

Figure II-11 compares the distribution of ARL_1 values with various methods for 50 realizations of the MMA and MAR time series. It was noticed that EWMA and SD-WCUSUM methods failed to detect the change in the MMA and MAR processes, as reflected in the large ARL_1 values. Moreover, for the MMA model, the SD-WCUSUM failed to detect changes in 20 of the 50 trials. Change detection with the SKL-Info method is comparable to that of the DPSGM for the MMA series. However, SKL-Info has much higher latency (ARL_1 values are higher by 2000 points) relative to DPSGM for detecting changes in the MAR time series.

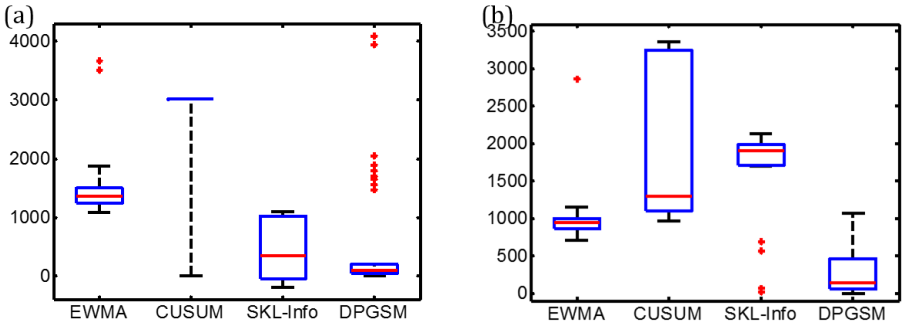

Figure II-11. Comparison of change point estimation with different methods for (a) MMA and (b) MAR models. (reprinted with permission)

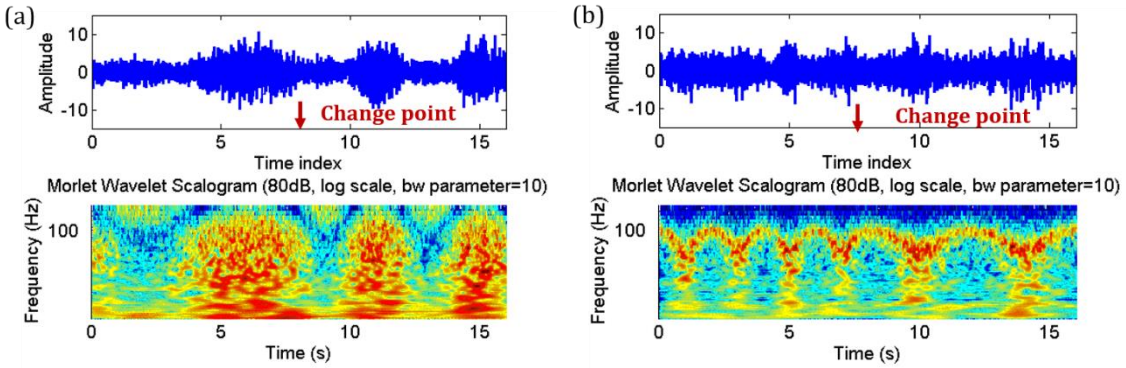

Figure II-12. Scalograms (a) MMA and (b) MAR time series. (reprinted with permission)

The SD-WCUSUM as well as SKL-Info methods essentially rely on the assumption that the underlying covariance structure and/or the frequency content over a large time window is stationary prior to the change, i.e., no intermittency. However, the spectrograms of MMA and MAR time series (see Figure II-12) suggest that the wavelet spectral content exhibits a distinct time-varying pattern even under non-anomalous conditions.

Consequently, SDWCUSUM and SKL-Info methods failed to detect the changes in these cases. In contrast, the DPGSM consistently obtains the lowest median ARL_1 values of 11.2 for MMA and 1.8 for MAR as shown in Figure II-12.

Music Signal Pattern Change Detection

Music and audio signals are inherently nonstationary and exhibit transient behaviors [52]. Their transient evolution, interestingly, creates a stationary mood, and a discerning human brain can detect a change in music patterns (e.g., the ragas genre in classical Indian music) within seconds (usually 3-100 sec) of its inception. Prior efforts to investigate the perception of music pattern changes, whether in key signature, scale, or relative articulation, are very limited, although significant efforts have been made towards automated classification of music patterns and ragas [53]. To investigate the effectiveness of the DPGSM for online, fast detection of changes in music patterns, we devised two test cases.

First, we considered the Introduction to "Smoke on the Water", and investigated the detection of the alternation of chord progression from $G5 - B^b5 - C5$ to $G5 - C5 - B^b5$ under the same key (Figure II-13 (a)) as well as a change in the key signature of chord progression from chord $E5$ to $D5$ (Figure II-13 (b)). The results, summarized in Table II-2, suggest that the present approach can detect changes in chord progression and key signature orders of magnitude earlier than with other methods.

We next studied a case inspired by the central structure of a classical Indian raga scheme, which prescribes a collection of "gestures" to develop the melody. A gesture is a sequence of notes, often inflected with various micro-pitch alterations and articulated with an expressive sense of timing. We investigated two cases of raga changes (see Figure II-14) (a) from a base raga *jaijaiwante* (Raga 1) to another, *khamaj* (Raga 2) that has the same notes as the base raga but follows a different sequence, and (b) from a base raga *yamankalyani* (Raga 3) to *yaman* (Raga 4), which has a note missing compared to the base raga. The results (see Table II-3) suggest that the conventional EWMA, as with most cases tested, does not provide timely detection of change (large ARL_1 with frequent false alarms). While SDWCUSUM as well as the present DPGSM can detect raga changes associated with missing note(s), only the DPGSM is able to detect changes when a raga transitions to another raga with the same set of notes but different rules for the rendition of the note sequences.

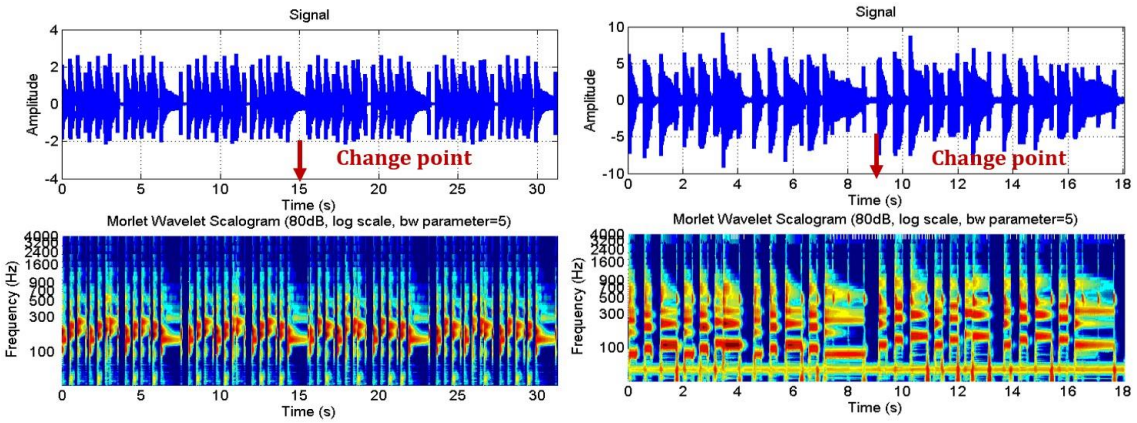

(a) Progressions alternation **(b) Key signature change chord**

Figure II-13. Representative time and time-frequency portraits of signals with changes in intermittency dynamics. (reprinted with permission)

Table II-2. ARL_1 comparisons. (reprinted with permission)

	EWMA	SD-WCUSUM	DPGSM
Chord progression alternation	-476 #	700	243
Key signature change	1320	1448	270

 # Due to the false alarm since the change point was set by Type I error

The results may be rationalized by examining the possible routes of changes for intermittency dynamics. A change in transit behavior may connote either (a) a different path taken through the same collection of attractors, (and hence mostly invariant time-frequency patterns), or (b) the meandering of system trajectories to attractors not visited earlier (the signals emanating therefrom may exhibit a distinct, and new note pattern). In the first case, both Ragas 1 and 2 contain the same scores but with different sequences. Since the reconstructed state space signal for each music note possesses the same set of attractors and hence frequency patterns, albeit with different transition

patterns, the frequency content (whose change is necessary for SD-WCUSUM-based detection) does not change. But the change in the sequence can cause the distribution of the transition vectors $\pi_j|*$ estimated from their local sample mean π_j and covariance matrix S_j to change dramatically. As a result, the Mahalanobis distance statistic value was able to indicate a change in the Raga which other methods could not detect. In the second case, two nonstationary signals consist of a different set of attractors (the consequence of a missing note) as Raga 4. The resulting difference in the frequency pattern was quickly discerned with SD-WCUSUM as well as the DPGSM.

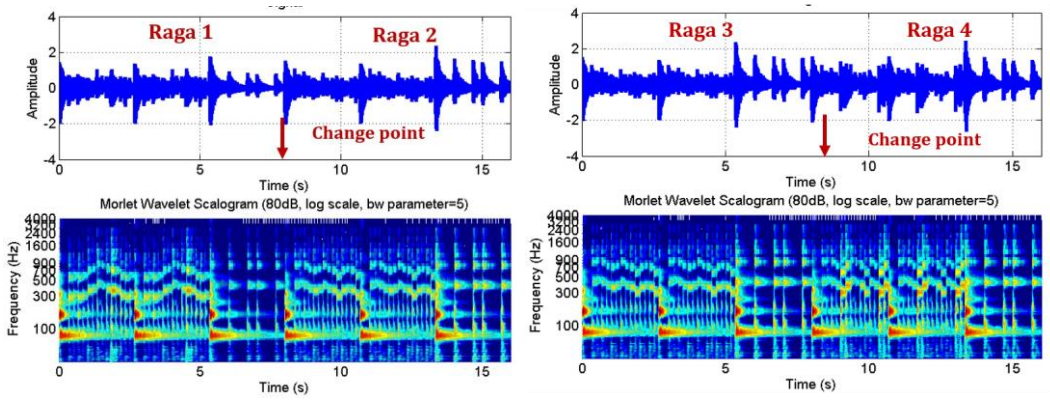

(a) Changes in ascending and descending scales (b) Scale change with missing notes

Figure II-14. Representative time and time-frequency portraits of raga snippets with micropitch and note sequence changes. (reprinted with permission)

Table II-3. Delay for detection (*ms*) for Raga music. (reprinted with permission)

	EWMA	SD-WCUSUM	DPGSM
Ascending and descending scales	24#	Inf	17
Descending scale with missing note	1682	191	151

#

Due to the false alarm since the change point was set by Type I error

Detecting Incipient Surface Quality Variation in Ultra-precision Manufacturing Processes

Next, we applied the DPSGM to detecting incipient anomalies in chemical mechanical polishing (CMP). The semiconductor industry widely employs this ultraprecision manufacturing process for realizing highly polished wafers for integrated circuit fabrication. Accurate and timely detection of incipient process anomalies including pad wear and the resulting surface scratches [see Figure II-15 (b)] is critical for quality and yield assurance [54]. We investigated the application of the present approach to detection of pad wear and scratch formation in the CMP process. Here, a bench-top CMP machine was equipped with a wireless (XBee IEEE 802.15.4 RF module) multi-sensor unit that included a MEMS 3-axis accelerometer from Analog Devices (ADXL 335) for polishing a copper disk (dia~40.6 *mm*, thickness~12.5 *mm*, and initial surface roughness *Ra*~15 *nm*). Although the accelerometer was sensitive to process variations, detection of surface deterioration in the early stages was challenging because of the noise induced by extraneous interferences.

Table II-4. Comparisons of delays (*ms*) in detecting CMP pad glaze. (reprinted with permission)

	EWMA	SD-WCUSUM	DPGSM
Pad wear	2941	2262	65
Depletion of slurry	45(*sec*)	Inf	20
Slurry coagulation	617	57	30

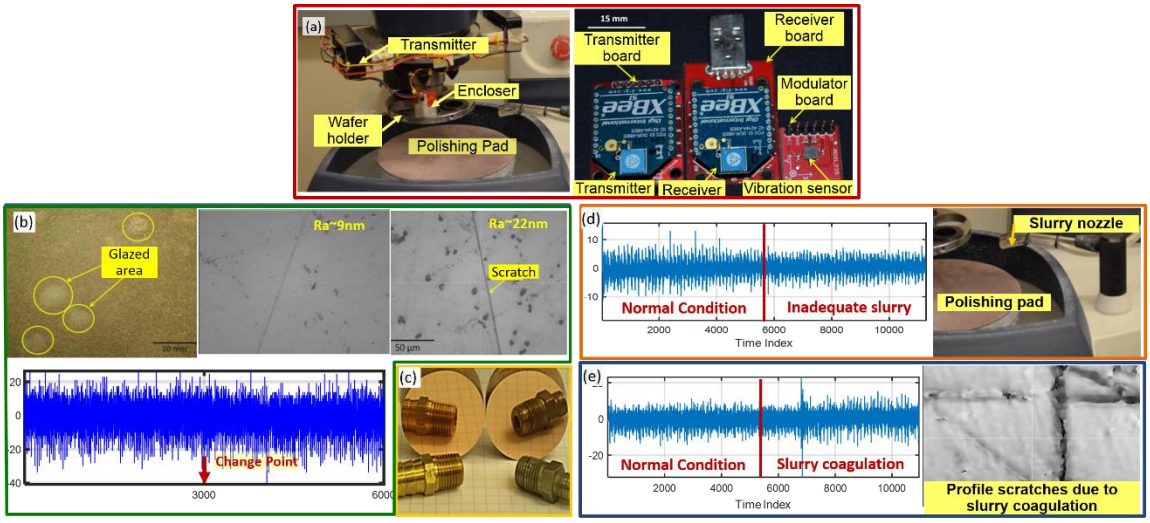

Figure II-15. (a) Bench top CMP machine with vibration sensor setup; (b) Glazed pad and wafer scratch after 12 min of polishing and the time portrait of a vibration signal capturing transition to glazed pad condition; (c) Copper wafer polished by the CMP setup with the mirror-like surface finish; Vibration signal gathered during polishing with observations of (d) depletion of slurry and (e) slurry coagulation. (reprinted with permission)

After 3 min of polishing (platen speed 250 RPM, head speed 60 RPM and download force 4 *lbs*), the average *Ra* improved to around 7 *nm*. After 12 min of polishing, significant

deterioration (glazing) of the polishing pad as well as scratches on the wafer were observed (Figure II-15Fig. 15(b)), and the finish degraded to *Ra* ~22 *nm*. In addition, depletion of slurry at the pad-wafer interface as well as coagulation of abrasive particles increased the propensity for scratches on the wafer surface. As shown in Figure II-15 (d) and (e), we created faults of slurry depletion (by closing the slurry gate), and abrasive particle coagulation (by introducing large-sized silica particles), respectively, at 90 sec of CMP polishing. The deteriorated surface with scratches (shown in the Figure II-15 (e)) were the consequences of these faults. Results comparing on-line detection of pad degradation along with slurry inadequacy and coagulation from vibration signals using the DPGSM, EWMA and SD-WCUSUM methods are summarized in Table II-4. It was noticed that the DPGSM outperformed the EWMA and SD-WCUSUM in all three cases by achieving the minimal delay of detection values. Especially for detection of the pad wear and scratch formation, the values for detection delay were more than 2.2 seconds with EWMA and SD-WCUSUM, while the DPGSM could detect the surface deterioration within 65 *ms*. These applications taken together indicate the potential of the present approach for early stage change detection in precision manufacturing processes that tend to exhibit transient dynamics.

Conclusions

This chapter has introduced a new approach based on a Dirichlet process Gaussian state machine (DPGSM) to detect changes in intermittency dynamics, one of the most common types of transient processes. The main conclusions from the present work are as follows:

- The DPGSM represents an intermittent process as a random walk about a Dirichlet process distribution of Gaussian clusters, with random sojourn times around each cluster. The elements of the Markov transition matrix that captures the random walk are shown to exhibit beta distribution.

- A DPGSM-based change detection method was developed based on discerning changes to the transition matrix elements. A Mahalanobis distance based statistic was investigated to capture changes in the transition matrix in the presence of large data.

- Numerical studies on DPGSM convergence suggest that errors in predicting the transition matrix of the DPGSM converge at a parametric rate wherever the clusters do not overlap (high concentration prior) and the time series samples are (fairly) independent of each other. However, when the cluster overlap is high or significant autocorrelations exist, the polylogarithmic rate provides a suitable lower bound for the convergence rate. We also developed a statistical constant

to obtain a suitable window length, L_{min} to obtain constant DPGSM models. Investigations also suggest that sensitivity exceeding 90% is possible by choosing proper window lengths L.

- The performance of the DPGSM approach was compared to multiple existing competing methods, namely EWMA, SD-WCUSUM and RNDP, using numerical benchmark test cases as well as real-world applications involving the detection of changes in music patterns and ultra-precision manufacturing. The ARL_1 metric was used to compare the sensitivity of the methods to detecting changes.

- Piecewise stationary ARMA models with variance changes and laminar sojourn time changes were designed to emulate changes in intermittency dynamics. The results indicate that ARL_1 values with DPGSM approach are 43% lower compared to other methods tested. More pertinently, only the DPGSM could detect the changes in sojourn times.

- Application to detecting changes in modulated moving average and modulated autoregressive models suggests that the DPSGM reduces ARL_1 values by 44% for MMA and 98% for MAR compared to competing methods.

- Several music clippings were designed to compare the detection of subtle music pattern changes (different note articulation and altered attractors). It was noticed

that SD-WCUSUM performed well in detecting frequency change cases but failed to detect changes in note alternation (i.e., the change is related to the path taken for visiting each attractor). The DPGSM approach outperformed others by detecting changes at least 40 ms in advance (21% improvement).

- In ultraprecision manufacturing processes (CMP), the DPGSM-based detection of incipient surface characteristic variations from subtle changes in vibration sensor signal patterns was investigated. DPGSM was able to capture the salient intermittency characteristics of the process from the vibration signal patterns and, consequently, was able to detect surface damage (scratches) almost an order of magnitude earlier than existing change detection methods (e.g., EWMA and SD-WCUSUM).

In closing, the DPGSM provides a robust approach to discerning incipient changes in intermittency dynamics and it can emerge as a viable tool for change detection in real-world intermittent nonstationary systems. Furthermore, to improve the present detection method, the robustness of the DPGSM model and parameter selection, especially for the sampling scheme, should be investigated. For example, concentration parameter ϑ and the use of alternative priors (e.g. Pitman-Yor processes) may play important roles in generating a proper Gaussian mixture as well as decreasing small false alarm rates.

References

[5] Wang, Z., Bukkapatnam, S. T. S., Kumara, S. R. T., Kong, Z., and Katz, Z., 2014, "Change detection in precision manufacturing processes under transient conditions", CIRP Annals - Manufacturing Technology, **63**(1), pp: 449-452. http://dx.doi.org/10.1016/j.cirp.2014.03.123.

[15] Raghavan, V., and Veeravalli, V. V., 2010, "Quickest Change Detection of a Markov Process Across a Sensor Array", IEEE Transactions on Information Theory, **56**(4), pp: 1961-1981. https://dx.doi.org/10.1109/TIT.2010.2040869.

[16] Érdi, P., and Lente, G., 2014, Stochastic chemical kinetics: Theory and (Mostly) Systems Biological Applications, vol. 1, Springer, New York.

[17] Cheng, C., Sa-ngasoongsong, A., Beyca, O., Le, T., Yang, H., Kong, Z., and Bukkapatnam, S. T. S., 2015, "Time Series Forecasting for Nonlinear and Nonstationary Processes: A Review and Comparative Study", IIE Transactions, **47**(10), pp: 1053-1071. https://dx.doi.org/10.1080/0740817X.2014.999180.

[18] Noé, F., and Fischer, S., 2008, "Transition networks for modeling the kinetics of conformational change in macromolecules", Current Opinion in Structural Biology, **18**(2), pp: 154-162. http://dx.doi.org/10.1016/j.sbi.2008.01.008.

[19] Montes De Oca, V., Jeske, D. R., Zhang, Q., Rendon, C., and Marvasti, M., 2010, "A cusum change-point detection algorithm for non-stationary sequences with application to

data network surveillance", Journal of Systems and Software, **83**(7), pp: 1288-1297. http://dx.doi.org/10.1016/j.jss.2010.02.006.

[20] Last, M., and Shumway, R., 2008, "Detecting abrupt changes in a piecewise locally stationary time series", Journal of Multivariate Analysis, **99**(2), pp: 191-214. http://dx.doi.org/10.1016/j.jmva.2007.06.010.

[21] Choi, H., Ombao, H., and Ray, B., 2008, "Sequential change-point detection methods for nonstationary time series", Technometrics, **50**(1), pp: 40-52.

[22] Killick, R., Eckley, I., and Jonathan, P., 2013, "A wavelet-based approach for detecting changes in second order structure within nonstationary time series", Electronic Journal of Statistics, **7**, pp: 1167-1183.

[23] Zbilut, J. P., Thomasson, N., and Webber, C. L., 2002, "Recurrence quantification analysis as a tool for nonlinear exploration of nonstationary cardiac signals", Medical Engineering & Physics, **24**(1), pp: 53-60. http://dx.doi.org/10.1016/S1350-4533(01)00112-6.

[24] Alippi, C., and Roveri, M., 2008, "Just-in-time adaptive classifiers—Part I: Detecting nonstationary changes", IEEE Transactions on Neural Networks, **19**(7), pp: 1145-1153.

[25] Lai, Y.-C., 1996, "Distinct small-distance scaling behavior of on-off intermittency in chaotic dynamical systems", Physical Review E, **54**(1), pp: 321.

[26] Zhang, M., Xu, S., and Fulcher, J., 2002, "Neuron-adaptive higher order neural-network models for automated financial data modeling", IEEE Transactions on Neural Networks, **13**(1), pp: 188-204.

[27] Ghazali, R., Hussain, A. J., Nawi, N. M., and Mohamad, B., 2009, "Non-stationary and stationary prediction of financial time series using dynamic ridge polynomial neural network", Neurocomputing, **72**(10-12), pp: 2359-2367.

[28] Cvitanovic, P., Artuso, R., Mainieri, R., Tanner, G., Vattay, G., and Whelan, N., 2005, Chaos: Classical and Quantum, Niels Bohr Institute, Copenhagen.

[29] Genç, M. S., Karasu, I., Acikel, H. H., Akpolat, M. T., and Genc, M., 2012, "Low Reynolds number flows and transition", Low Reynolds Number Aerodynamics and Transition, Genc, MS Ed.; InTech: Rijeka, Croatia, pp: 1-28.

[30] Wang, X.-J., 1989, "Statistical physics of temporal intermittency", Physical Review A, **40**(11), pp: 6647.

[31] Isola, S., 1999, "Renewal sequences and intermittency", Journal of Statistical Physics, **97**(1-2), pp: 263-280.

[32] Sturman, R., and Ashwin, P., 2004, "Internal dynamics of intermittency", Dynamics and Bifurcation of Patterns in Dissipative Systems, **12**, pp: 357.

[33] Kawabata, T., and Nishikawa, K., 2000, "Protein structure comparison using the markov transition model of evolution", Proteins: Structure, Function, and Bioinformatics, **41**(1), pp: 108-122.

[34] Bertuccelli, L. F., and How, J. P., 2008, "Estimation of non-stationary Markov chain transition models", Proc. of 47th IEEE Conference on Decision and Control,Cancun, Mexico, IEEE, pp: 55-60.

[35] Guo, H., Paynabar, K., and Jin, J., 2012, "Multiscale monitoring of autocorrelated processes using wavelets analysis", IIE Transactions, **44**(4), pp: 312-326.

[36] Dai, A. M., and Storkey, A. J., 2015, "The Supervised Hierarchical Dirichlet Process", IEEE Transactions on Pattern Analysis and Machine Intelligence, **37**(2), pp: 243-255. 10.1109/TPAMI.2014.2315802.

[37] Marwan, N., Romano, M. C., Thiel, M., and Kurths, J., 2007, "Recurrence plots for the analysis of complex systems", Physics reports, **438**(5), pp: 237-329.

[38] Bukkapatnam, S. T., and Cheng, C., 2010, "Forecasting the evolution of nonlinear and nonstationary systems using recurrence-based local Gaussian process models", Physical Review E, **82**(5), pp: 056206.

[39] Katok, A., and Hasselblatt, B., 1997, Introduction to the modern theory of dynamical systems, vol. 54, Cambridge university press.

[40] Liu, C.-S., 2007, "A study of type I intermittency of a circular differential equation under a discontinuous right-hand side", Journal of Mathematical Analysis and Applications, **331**(1), pp: 547-566.

[41] Neal, R. M., 2000, "Markov chain sampling methods for Dirichlet process mixture models", Journal of Computational and Graphical Statistics, **9**(2), pp: 249-265.

[42] Crommelin, D. T., and Vanden-Eijnden, E., 2006, "Fitting timeseries by continuous-time Markov chains: A quadratic programming approach", Journal of Computational Physics, **217**(2), pp: 782-805. http://dx.doi.org/10.1016/j.jcp.2006.01.045.

[43] Hinrichs, N. S., and Pande, V. S., 2007, "Calculation of the distribution of eigenvalues and eigenvectors in Markovian state models for molecular dynamics", The Journal of chemical physics, **126**(24), pp: 244101.

[44] Ghosal, S., Ghosh, J. K., and van der Vaart, A. W., 2000, "Convergence rates of posterior distributions", Annals of Statistics, **28**(2), pp: 500-531. https://doi.org/10.1214/aos/1016218228.

[45] Ma, J., Xu, L., and Jordan, M. I., 2000, "Asymptotic convergence rate of the EM algorithm for Gaussian mixtures", Neural Computation, **12**(12), pp: 2881-2907.

[46] Genovese, C. R., and Wasserman, L., 2000, "Rates of convergence for the Gaussian mixture sieve", The Annals of Statistics, **28**(4), pp: 1105-1127.

[47] Ghosal, S., and Van Der Vaart, A. W., 2001, "Entropies and rates of convergence for maximum likelihood and Bayes estimation for mixtures of normal densities", Annals of Statistics, pp: 1233-1263.

[48] Shen, W., Tokdar, S. T., and Ghosal, S., 2013, "Adaptive Bayesian multivariate density estimation with Dirichlet mixtures", Biometrika, **100**(3), pp: 623-640.

[49] Ghosal, S., and Van Der Vaart, A., 2007, "Posterior convergence rates of Dirichlet mixtures at smooth densities", The Annals of Statistics, **35**(2), pp: 697-723.

[50] Kristan, M., Leonardis, A., and Skočaj, D., 2011, "Multivariate online kernel density estimation with Gaussian kernels", Pattern Recognition, **44**(10–11), pp: 2630-2642. http://dx.doi.org/10.1016/j.patcog.2011.03.019.

[51] Davis, R. A., Lee, T. C. M., and Rodriguez-Yam, G. A., 2006, "Structural break estimation for nonstationary time series models", Journal of the American Statistical Association, **101**(473), pp: 223-239.

[52] Nakano, M., Le Roux, J., Kameoka, H., Ono, N., and Sagayama, S., 2011, "Infinite-state spectrum model for music signal analysis", Proc. of 2011 IEEE International Conference on Acoustics, Speech and Signal Processing (ICASSP),Prague, Czech Republic, 22-27 May 2011, pp: 1972-1975.

[53] Chordia, P., and Rae, A., 2008, "Real-time Raag recognition for interactive music", Proc. of 8 th International Conference on New Interfaces for Musical Expression NIME08,Genova, Italy, pp: 331-336.

[54] Rao, P. K., Bhushan, M. B., Bukkapatnam, S. T. S., Zhenyu, K., Byalal, S., Beyca, O. F., Fields, A., and Komanduri, R., 2014, "Process-Machine Interaction (PMI) Modeling and Monitoring of Chemical Mechanical Planarization (CMP) Process Using Wireless Vibration Sensors", IEEE Transactions on Semiconductor Manufacturing, **27**(1), pp: 1-15. https://doi.org/10.1109/TSM.2013.2293095.

CHAPTER III

BUILT-UP-EDGE EFFECTS ON SURFACE DETERIORATION IN MICROMILLING PROCESSES[2]

Preface

Built-up edge (BUE) has been noted as a major cause for surface finish deterioration in micromachining processes—even a trace formation of hardened and brittle structure on the tool edge alters the chip load, creates ad hoc and irregular material flow patterns, and results in deposits and smeared regions on the machined surface. To date, few investigations have addressed the formation and effects of BUE in micromachining. This report is one of the first experimental investigations of the BUE effects on surface quality and its prediction in micromachining. Experiments were conducted on a Haas OM2 CNC milling system with air bearing spindle. The experiments consisted of micromilling 12 mm long thin channels on 316L stainless steel plates (30×40×0.5 mm) using uncoated tungsten carbide micromills (from Performance Micro Tools with flat end and Φ0.406 mm diameter) at 16 different settings of carefully selected combination of cutting speed and chip load with minimum quantity lubrication (MQL). The surface morphology including BUE distribution, as well as BUE formation on tool surfaces were studied *ex situ* via optical and

[2] Reprinted with permission from "Built-up-edge effects on surface deterioration in micromilling processes" by Z. Wang, V. Kovvuri, A. Araujo, M. Bacci, W.N.P. Hung, and S.T.S. Bukkapatnam, Journal of Manufacturing Processes, 2016, 24: 321-327, https://doi.org/10.1016/j.jmapro.2016.03.016, Copyright [2016] by Elsevier. For copyright details, please visit https://www.elsevier.com/about/policies/copyright

scanning electron microscopy. We introduce two metrics to quantify the severity of BUE, namely, BUE density and its distribution entropy. These metrics capture, respectively, the extent and dispersion of BUE on the surface. We also conducted empirical studies to assess the extent to which these quantifiers can determine the variation in surface finish (S_a). Results suggest that the BUE is the major determinant of surface finish besides the chip load effect in micromachining. Statistical Granger-causality tests suggest also that estimation of the BUE density can help with improving the accuracy (R^2) of surface finish S_a prediction from a negative value (poor fit) with conventional model to 0.4, i.e., 40% of S_a variation in the micromachining experiments can be attributed to the BUE effect.

Introduction

Micromachining processes have found growing applicability in the industry for realizing complicated geometries, such as for fabricating masks for X-ray lithography, creating microfluidic channels, and biomedical devices [55]. This process employs slender endmills of diameters < 0.5mm at axial depths in 2-50 μm range [56-62]. In this process, the tool edge radius is comparable to the chip thickness, axial depth of cut and material grain size (see Figure III-1). The round tool edge promotes a distinct negative rake angle regime that gives rise to a unique chip formation and cutting mechanism where the workpiece material is subject to a predominantly ploughing effect with some shear, which is often highly localized.

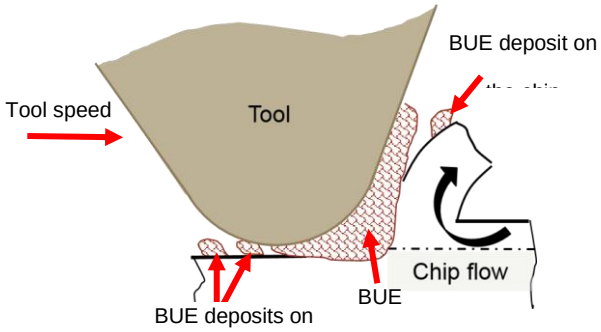

Figure III-1. Schematic diagram of built-up edge formation in micro machining processes. (reprinted with permission)

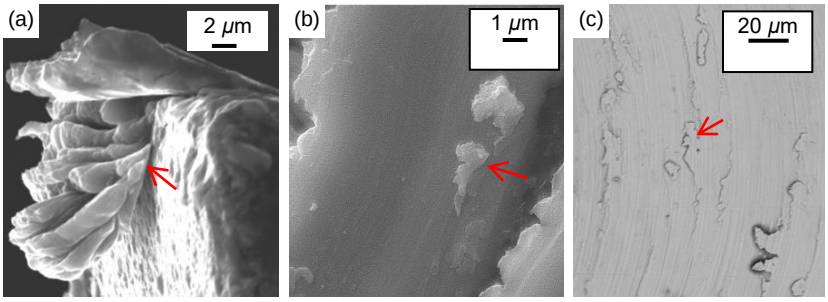

Figure III-2. BUE deposits on (a) tool rake face, (b) chip flank face, and (c) micromilled surface. (reprinted with permission)

Even at low chip loads employed in micromachining, the cutting geometry (e.g., negative rake angle) and machining mechanisms promote temperature fields and material quiescent zones that are known to lead to BUE formation [63]. Since the dimension of BUE is of the same order of magnitude of depth of cut and chip thickness (see Figure III-1), even

with little amount of BUE, the rake angle and the effective tool geometry and thence the cutting forces are altered substantially [64]. As in conventional machining, the hardened and brittle BUE would smear the machined surface under the tool flank face by the effects of friction and thermomechanics [63, 65]. Also, the fractured segments of the brittle BUE are either swept away as the chip flows up the tool (Figure III-2 (b)) and/or would adhere to the workpiece surface (BUE deposits shown in Figure III-2 (c)) thereby affecting the surface quality.

The physics of BUE formation and the effect of BUE on deterioration of surface characteristics in conventional machining has received notable attention, particularly in terms of providing guidance on proper process parameter selection to eliminate BUE [66, 67]. Pertinently, it was suggested that milling process with high feed rate would cause the surface deterioration due to the effect of BUE [68-71]. Recent research attempts have also addressed process control and quality improvement based on BUE detection and prediction. Shahabi and Ratnam [72] proposed an *in situ* inspection technique to detect and measure BUE. A subtraction method and polar-radius transformation algorithms on images from high resolution microscopes were applied to detect the formation of BUE. Fang *et al*. [73] developed resource allocation network and multilayer perceptron network models to predict BUE formation in round and sharp cutting tool edges.

Although BUE is a major limiter of surface finish in micromachining, very few efforts to date have investigated the effects of BUE in micromachining. For example, some

ex situ techniques have been report to characterize BUE using Scanning Electron Microscope (SEM) and optical microscope [66]. Ucun *et al*. [74] investigated the BUE effect on surface finish with different process parameters in micromilling of Inconel 718 alloy and observed that machining with a coated cutting tool would minimize BUE formation and low surface roughness realized at low feeds. To date, these sparse observations are yet to be represented quantitatively. Mathematical models exist in conventional and ultraprecision machining to relate surface roughness quantifiers such as R_a and R_q with process parameters [75, 76]. Such models tend to become highly inaccurate for micromachining. Our recent experimental studies suggest that BUEs are the main reason leading to the bias between the theoretical model estimates and experimental measurements of surface roughness in micromachining [77, 78]. Therefore, the models need to be modified to accommodate BUE effect. However, the lack of a suitable quantifier of BUE and its severity limits our ability to characterize its effect on surface deterioration and thereby obtain an accurate estimate of variation of surface roughness quantifiers (e.g., R_a and S_a) in micromachining.

This chapter presents an experimental study of BUE formation in micromachining of thin channels on 316L plates under various settings of cutting speed and chip load with minimum quantity lubrication (MQL). Based on subsequent *ex situ* optical and SEM characterizations of the micromachined surfaces we present two metrics that quantify the extent and the spatial dispersion of BUE on the machined surface. Further investigations

and subsequent confirmatory experiments suggest that BUE is the major determinant of surface finish in micromachining beyond the chip load effect considered in conventional mesoscale machining. The proposed BUE quantifiers increased the accuracy of surface finish S_a estimation in micromachining with R^2 increasing from -11.35 (i.e., the discrepancy is much larger than the variations in the S_a measurements) with conventional models to over 0.4 with BUE quantifiers. The remainder of this chapter is organized as follows: Sec 2 presents our experimental approach and the experimental confirmation of BUE. Quantification of BUE in micromilling as well as the results on S_a prediction with BUE consideration are provided in Sec. 3, and conclusions are presented in Sec. 4.

Experimental Setup

The micro-milling experiments consisted of machining microchannels on 316L stainless steel plates (30×40×0.5 mm) using a Haas OM2 CNC milling system fitted with an air bearing spindle (Figure III-3(a)). Workpiece alignment with the horizontal machine plane was measured by sweeping the plate surface using a Mitutoyo indicator with 1.27 µm (0.000,05 in) resolution, and parallelism precision within 2 µm along every 25 mm. We used double flute uncoated tungsten carbide micromills (from Performance Micro Tools). The end mills had a flat end with a tool diameter of Φ0.406 mm, tool edge radius of ~5 µm and a flute length 1.220 mm. A 12 mm long slot (Figure III- 3 (b)) was machined using these tools under 16 different process conditions (Table III-1) obtained from varying the cutting speed (10, 27, 44, 60m/min) and the chip load (0.05, 0.20, 0.50, 1.00 µm/tooth).

The depth of cut (Doc) was selected as 30 µm which resulted in a significantly large Doc/edge radius ratio (600% compared to critical value as 50%) to improve cutting under all process conditions. All experiments were conducted with minimum quantity lubrication (MQL). In addition, two sets of meso-scale milling processes experiments were conducted under 2 to 100 µm/tooth chip loads: The first set of experiments were conducted on a pure titanium workpiece using a signal flute AlTiN coated WC tool with Φ0.8 mm diameter and 5.2^{o} concavity angle, at 10 m/min speed, 30 μm depth, dry condition at chip loads in 2~8 µm/tooth range. The second set was conducted on a 6061-T6 aluminum workpiece using a double flute Φ3.175 mm uncoated high speed steel tool of 3.5° concavity angle, at 60 m/min speed, 100 µm depth, dry condition, for chip loads in 12.7 to 101.6 μm/tooth range.

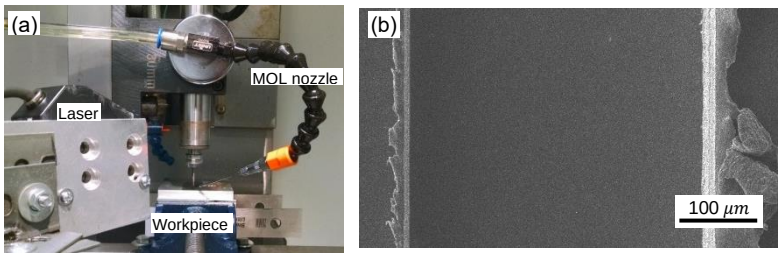

Figure III-3: (a) Experimental setup from micromilling, including the MQL nozzle, laser displacement sensor (Keyence LK-G82) for alignment and 316L stainless steel plate (30×40×0.5 mm) on the workpiece holder, (b) SEM image of a channel segment on workpiece machined using an uncoated tungsten carbide tool with Φ0.406mm and concavity angle of 7°. (reprinted with permission)

The machined workpiece was then treated with acetone in an ultrasonic cleaner for 5 minutes. Subsequently, the surface characteristics, including the surface profile and surface roughness (S_a) of the stainless steel plate were analyzed via multiple non-contact metrology instruments, namely, optical interference microscope (Zegage from Zygo), optical microscope (Olympus STM6) and scanning electron microscope (TESCAN Vega LM3) integrated with an energy dispersive X-ray spectroscopy (EDS) system. The workpiece was Au-Pd sputter-coated prior to SEM imaging. The images were subsequently processed using Image Pro software for BUE quantification and analysis. A summary of the average S_a values obtained each experimental condition is provided in Table III-1.

Table III-1. Achieved surface roughness S_a (µm) values averaged over ten measurements taken at random locations of the channel machined under each of the selected process parameters with consistent 30 µm depth of cut. (reprinted with permission)

Cutting Speed (m/min) / Chip Load (µm/tooth)	10	27	44	60
0.05	0.154	0.138	0.094	0.094
0.2	0.155	0.137	0.087	0.091
0.5	0.148	0.139	0.091	0.084
1	0.130	0.136	0.093	0.075

Figure III-4(a) shows the SEM images of a workpiece surface with BUE after machining at a chip load of 0.05 μm/tooth and cutting speed of 10 m/min. Note that the size of BUE deposit appears twice as large as the chip load. An SEM image of the BUE formation observed on the tool edge is shown in Figure III-4(b). The geometry of the BUE image suggests a high amount of localized shear and deformation of chip. The associated thermomechanical regime is known to conducive to sustain BUE formation [79]. We employed energy dispersive spectrum (EDS) on the samples with BUE deposits. Results suggest that the chemical composition of the samples studied is consistent with the one of 316L (Table III-2), indicating that the adherent matter on the tool edge and the workpiece surface is indeed a BUE.

Table III-2. Chemical composition of 316L stainless steel and a BUE after micromilling. (reprinted with permission)

Element	316L stainless steel	BUE
Cr	16-18%	17.7%
Ni	10-14%	9%
O	0	4%
Mn	<2%	1.6
Si	<0.75%	0.4
Fe	Balance	69%

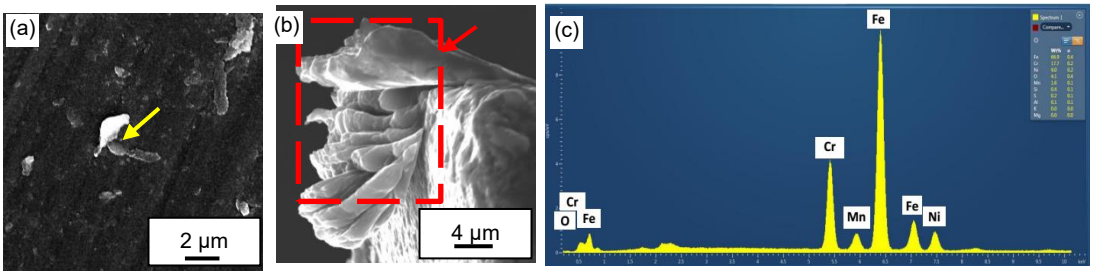

Figure III-4. (a) SEM image of typical built-up-edges on micromilled surface. Micromilling 316L stainless steel with ø0.406 mm tool, 10 m/min speed, 0.05 µm/tooth chip load, 30 µm depth, MQL; (b) SEM image of built-up-edges on the cutting edge of a micromilling tool; (c) Energy dispersive spectrum of the BUE. (reprinted with permission)

Subsequently, we performed a quantitative characterization of how BUE influences surface roughness in a micromachining process. As noted earlier, previous works (e.g.,[80]) suggest that under wet meso-scale machining, the surface roughness R_a (or S_a) are essentially functions of the chip load f_t and the concavity angle γ, i.e.,

$$R_a = \frac{\tan(\gamma)}{4} \cdot f_t \tag{1}$$

We tested the predictions from this conventional surface roughness estimation model using a prior meso-scale milling experiment [78] in addition to the aforementioned micromilling experiments. For meso-scale milling processes, a high-speed steel tool with diameter Φ3.175 mm and concavity angle 3.5° was employed with depth of cut of 100 µm under dry condition. As summarized in Figure III-5, surface roughness estimation model was valid for meso-scale milling (R^2~94%) while it failed to capture the surface profile trends for micromilling with chip loads below 1 µm/tooth. While BUE can be contributing

to this discrepancy, absent a consistent metric it is not possible to quantitatively capture its effect on S_a.

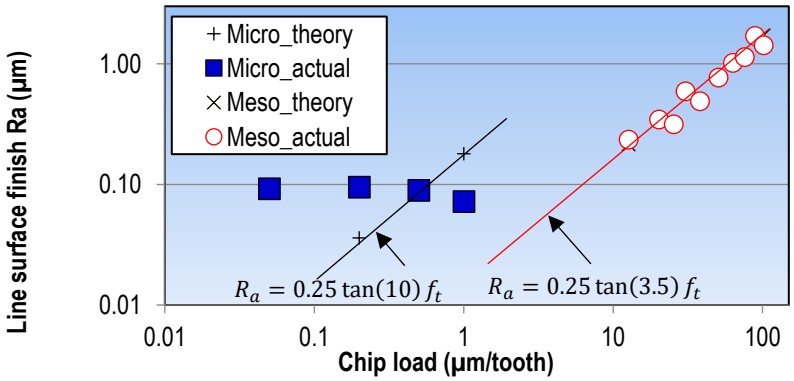

Figure III-5. Theoretical and experimental results for surface finish in meso- and micro-milling with cutting speed 60 m/min. (reprinted with permission)

BUE Quantification and Surface Roughness Prediction

As noted in the foregoing, an appropriate quantification of BUE effect is needed (similar to how V_b the width of the wear land has emerged as a quantifier for flank wear effects) for accurate prediction of surface roughness in micromilling processes and thus design process conditions to improve quality assurance. Here, we present an approach for BUE quantification based on a statistical analysis of surface images. Although images from various microscopes can be employed for BUE quantification, we use optical microscope (Olympus STM6) to ensure wider relevance. In total, 20 images were taken at the scale of 100×100 μm^2 for each experimental condition—ten of which were captured on the

upmilling regions and the other ten on the downmilling regions. Associated surface profiles and roughness values (including S_a and S_q) were gathered using a Zegage profilometer from Zygo. We introduce quantifiers that capture, respectively, the volume and the dispersion of BUEs on a machined surface for surface finish prediction in micromilling. The procedures of estimating the different BUE quantifiers are as follows:

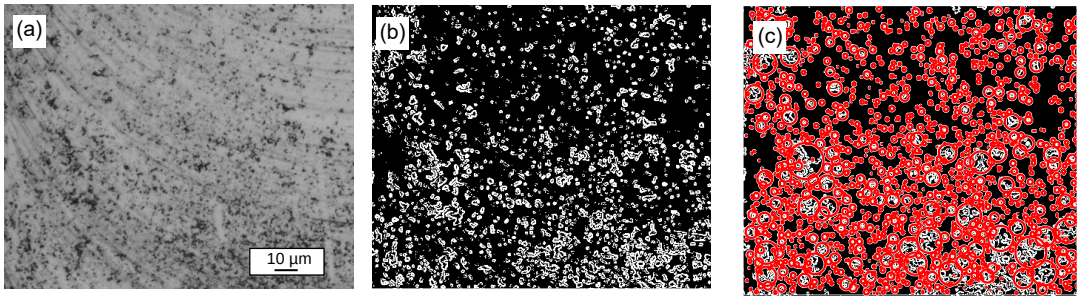

Figure III-6. (a) Processing the optical microscope images of micromilled surfaces, (b) extraction of binary imaging to BUE images and (c) subsequent delineation of BUE boundaries (process conditions: 316L stainless steel workpiece with uncoated WC tool, Φ0.406 mm, at 10 m/min speed, 0.05 µm/tooth chip load, 30 µm depth, MQL). (reprinted with permission)

BUE density estimation: Techniques borrowed from digital image analysis literature [81] were applied to extract the density of BUE residues on the finish. The procedure consisted of (see Figure III-6): (1) Converting microscopic image to a gray-scale matrix/image, (2) Automatic estimates of #(BUE), the count of independent BUE residues (marked in red in Figure III-6(c)) based on using the image grayscale variation in adjacent pixels to

determine the boundaries and segments, (3) computing the BUE density using the following equation:

$$\rho(BUE) = \frac{\#(BUE)}{\mathrm{A}} \times 10^2 \quad (2)$$

where area A refers to 100×100 μm^2 sample image area. It may be noted that $\rho(BUE)$ can serve as a surrogate for the volume of BUE generation. However it does not quantify the variation in the BUE fragment sizes or the dynamic (intermittent) nature of the BUE inception, growth, fragmentation, and deposition process [82].

BUE entropy: The image entropy quantifies the variation of BUE residues on the micromachined surface. Here, the entropy H of a BUE image is given by:

$$H(BUE) = -\sum_k p_k \, log_2(p_k) \quad (3)$$

where p_k is the fraction of histogram counts returned from image which represents the probability of the difference of gray-scale value between any two adjacent pairs of pixels equals k ($k = 0,1, \dots ,255$). It may be noted that $H(BUE)$ captures the irregularity in the size and dispersion of BUE on a micromachined surface but the volumetric information is absent.

We note that this procedure is an improvement over popular image analysis tools such as ImageJ in the sense that ImageJ counts were found to be sensitive to the feed marks, and assume near-circularity of the BUE deposits. The thresholds chosen from our methods provide flexibility to isolate BUE dispersion as noted in Figure III-6.

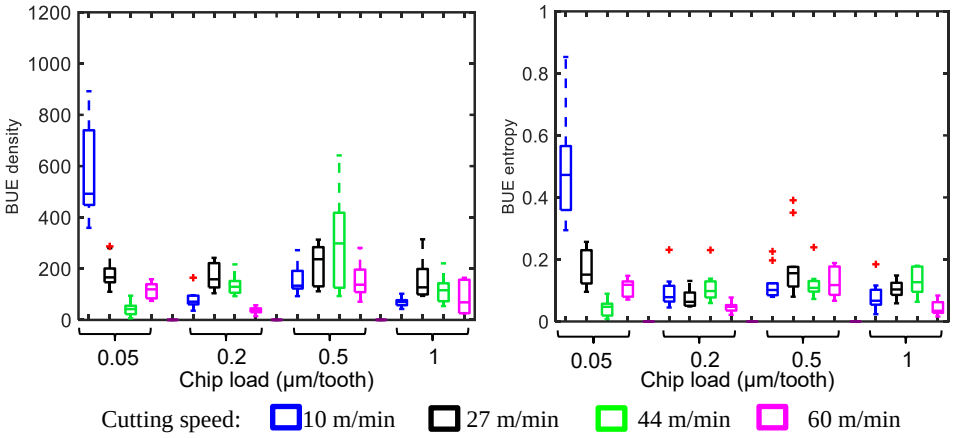

a) Boxplot of BUE density under 16 conditions b) Boxplot of BUE entropy under 16 conditions

Figure III-7. Variation of the BUE quantifiers with the cutting speed and chip load. (reprinted with permission)

Figure III-7 summarizes the variation of the quantifiers $\rho(BUE)$ and $H(BUE)$ with cutting speed under various chip load conditions. The figure indicates that the BUE volume and entropy values are the highest at the low cutting speed and chip load setting. This condition is most conducive for BUE formation because under this condition the edge effects are predominant and likelihood for material seizure and subsequent formation and severance of BUE is high. Under the low chip load of 0.05 μm/tooth the BUE density and entropy does not monotonically decrease as the cutting speed increases. Similar observations of BUE effect in micromachining when the depth of cut is in the range of 100 μm was presented by Weule *et al*. [83]. They note that as the cutting speed increases from 5 to 140 m/min, BUE effect is worse at cutting speed of 60 m/min due compared to that at 40 m/min or 80 m/min. Also, given the distribution of the shapes and sizes of BUE deposits

observed from our experiments, we believe that more than one route for BUE formation exist in micromachining due to extreme shear localization and associated thermomechanical regimes concentrated around the tool edge [84]. These may include adhesion and asperity deformation with thermal softening [85]. Investigations into the thermomechanics, chip formation and interaction between machined surface and tool flank face would be necessary to fully understand these interesting observations of BUE formation in micromilling.

More pertinently, Pearson correlation values in Table III-3suggest that $\rho(BUE)$ and $H(BUE)$ are positively correlated mutually and with the measured S_a values. All p-values from a student *t*-test [86] (Table III-4) were below the significance level of 0.05, indicating that these correlations are statistically significant.

Table III-3. Pearson correlation between BUE features and surface roughness (Process parameters: chip load 1 µm/tooth, cutting speeds 10, 27, 44, 60 m/min). (reprinted with permission)

	S_a	BUE Density	BUE Entropy
S_a	1.00	0.56	0.47
BUE Density	0.56	1.00	0.60
BUE Entropy	0.47	0.60	1.00

Table III-4. The p-values from a student-t test (the orange elements are with the p-values less than 0.05). (reprinted with permission)

	S_a	BUE Density	BUE Entropy
S_a	-	1.5E-04	2.2E-03
BUE Density	1.5E-04	-	4.8E-05
BUE Entropy	2.2E-03	4.8E-05	-

Table III-5. F-statistic values for causality of BUE density and entropy to the surface finish quality (the elements are painted orange if their values are greater than the rejection criterion at 0.05 significant level). (reprinted with permission)

F-Statistic	BUE Density	BUE Entropy
For S_a	7.10	3.64
For S_q	16.46	5.94

However, the correlations could not indicate the potential existence of causal relations [17, 87]. The causes with underlying relations may be indirect, and high correlations may be due to the tautologies (overlap with identity relations) where even no causal process exists. As a result, correlation between BUE features and the surface roughness is insufficient to establish a causal relationship. Alternatively, a Granger-causality test [88] was then applied to BUE features' impact on surface quality. The null hypothesis is tested for possible rejection under assumption that BUE features are not useful in estimating the surface roughness S_a. The observed F-statistic values (rejection criterion at 0.05 significance level was 4.11) are listed in Table III-5. The results indicate that only BUE density is a causal predictor of S_a, but both the density and entropy are causal predictors of S_q. The reason why the features are more significant for predicting S_q rather than S_a could be explained as

follows: the BUE deposits on a micromilled surface cause large peaks and valleys on the profiles compared to those caused by the tool feed. These large variations affect RMS value (i.e. S_q) much more so than the mean absolute deviation S_a.

Based on the foregoing, we used BUE density as a predictor of surface roughness S_a along with the chip load f_t and the concavity angle γ. The modified S_a prediction model was of the form:

$$S_a = 0.25\, tan(\gamma) \cdot f_t + a \cdot \rho(BUE) \tag{4}$$

where the coefficient a captures the effect of BUE on S_a. The model prediction results are summarized in Table III-6. The low p-value (0.00322) indicates the significance of the chosen feature (BUE density) in the prediction of surface roughness. A standard error of some 25% of the coefficient indicates marginal collinearity between the chip load and the BUE density values. The implication of this model is that as chip load increases, there is an upper bound on the uncut chip thickness above which BUE effect on surface morphology becomes insignificant. To substantiate this point, predictions with the conventional model (green/light line) and the improved model (black line) were plotted along with actual surface roughness measurements (depicted as blue/dark squares). The results indicate that the conventional model can capture the variation of S_a under meso-scale milling (Table III-7) but it fails to predict the surface roughness in micromilling for chip loads ≤1 μm/tooth (Table III-7b)). In fact, the prediction accuracy R^2 for chip loads ≤1 μm/tooth falls to -11.35, indicating that systematic deviations far exceed even the natural

variation in the measured S_a values with process conditions. In contrast, the modified model can capture the surface profile characteristics under micromilling with an R^2 of 0.4.

Table III-6. Linear regression result for modified estimation model. (reprinted with permission)

Fitting variables	Estimate	Std. Error	p-value
Coefficient a	1.962e-05	5.902e-06	0.00322

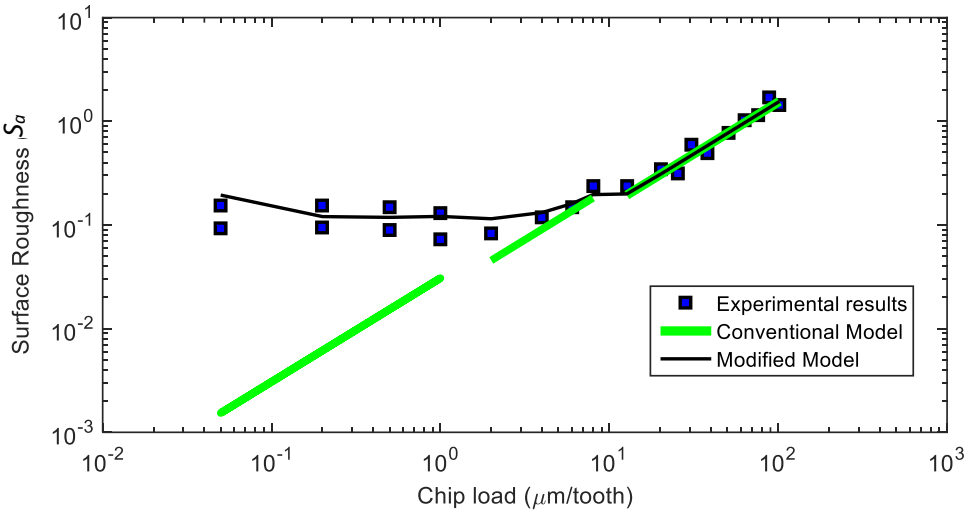

Figure III-8. Prediction results of conventional and modified models with the experimental S_a measurements. (reprinted with permission)

Table III-7. Comparisons of Sa estimation results between conventional and modified models. (reprinted with permission)

	Conventional model	Improved model
R^2	0.94	0.96

a) Comparison of total R^2 for conventional vs. improved models

	Conventional model	Improved model
R^2	-11.35	0.40

b) Comparison of R^2 for conventional vs. improved models under micromilling conditions (chip load ≤1 μm/tooth)

Additionally, a lower bound of chip thickness would also likely exist below which no chip formation happens and elastic deformation regimes dominate. Perhaps due to the surface asperities being of the same order as the chip load and axial depth, chips bearing marks of shear localization were observed even at the lowest chip load and depth condition experimented (Figure III-9). Further experiments with chip load < 1µm/tooth need to be conducted on surfaces prepared to a much finer finish to understand the chip and BUE formation mechanisms and establish the existence of critical chip thickness.

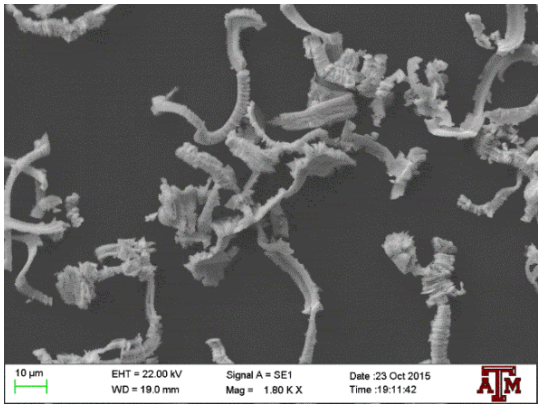

Figure III-9. SEM image of collected chip under micromilling processes (process parameters: depth 2-5 µm, RPM: 7839 rev/min, chip load 0.2 µm/rev). (reprinted with permission)

Conclusions

We reported the BUE effects on surface deterioration and present quantification of BUE using a set of experimental results of micromilling. The main conclusions from the present work are as follows:

- Investigations and subsequent confirmatory experiments through microscopic and SEM characterization suggest that the presence of BUE is detrimental to surface finish in micromachining. Using the *ex-situ* optical and SEM characterization of the micromachined surfaces, an image process based technique was applied to generate two quantifiers of BUE that capture the BUE effect on surface morphology deterioration;
- The significance of presented BUE quantifiers on surface deterioration was verified using the student-t tests on the correlation between test BUE features and achieved surface finish. Evidences are shown as small p-value compared to the significance level α=0.05. Moreover, results from Granger-causality hypothesis test signifies the impact of presented BUE density on surface morphology estimation under micromilling processes with significant large F-statistic values (5.64 which is larger than the critical value for rejection 4.41 with α=0.05);
- The BUE density was introduced in the surface roughness estimation model as a major predictor reflecting the BUE's impact on surface deterioration. The modified

estimation model achieves accurate estimation on surface roughness with R^2 over 0.96. Consequently, prediction results imply that our modified model could capture the surface profile variations in micromillings with significantly improvement as R2~0.4 compared to conventional model poorly fitted with negative R2 value.

Future investigations will attempt to quantify and predict surface finish in micromilling due to (i) tool coating, (ii) tool wear, (iii) process parameters, (iv) workpiece material properties, and (v) thermomechanics. Additionally, the ongoing effort is focused on understanding the chip morphology as well as causal mechanisms for high BUE under low chip loads.

Acknowledgments

The authors acknowledge the generous support of the NSF grant (CMMI-1432914). We also thank Mr. Tim Walker of Unist for the technical support, and Mr. Patrick Anderson of Performance Micro Tools for the microtools.

References

[17] Cheng, C., Sa-ngasoongsong, A., Beyca, O., Le, T., Yang, H., Kong, Z., and Bukkapatnam, S. T. S., 2015, "Time Series Forecasting for Nonlinear and Nonstationary Processes: A Review and Comparative Study", IIE Transactions, **47**(10), pp: 1053-1071. https://dx.doi.org/10.1080/0740817X.2014.999180.

[55] Bissacco, G., Hansen, H. N., and De Chiffre, L., 2005, "Micromilling of hardened tool steel for mould making applications", Journal of Materials Processing Technology, **167**(2–3), pp: 201-207. http://dx.doi.org/10.1016/j.jmatprotec.2005.05.029.

[56] Adams, D. P., Vasile, M. J., Benavides, G., and Campbell, A. N., 2001, "Micromilling of metal alloys with focused ion beam–fabricated tools", Precision Engineering, **25**(2), pp: 107-113. http://dx.doi.org/10.1016/S0141-6359(00)00064-7.

[57] Liu, X., DeVor, R. E., and Kapoor, S. G., 2007, "Model-based analysis of the surface generation in microendmilling—part II: experimental validation and analysis", Journal of manufacturing science and engineering, **129**(3), pp: 461-469.

[58] Sreeram, S., Kumar, A. S., Rahman, M., and Zaman, M., 2006, "Optimization of cutting parameters in micro end milling operations in dry cutting condition using genetic algorithms", Int J Adv Manuf Technol, **30**(11-12), pp: 1030-1039.

[59] Jin, X., and Altintas, Y., 2012, "Prediction of micro-milling forces with finite element method", Journal of Materials Processing Technology, **212**(3), pp: 542-552.

[60] Lauro, C., Brandão, L., Panzera, T., and Davim, J., 2015, "Surface Integrity In the Micromachining: A Review", Rev. Adv. Mater. Sci, **40**, pp: 227-234.

[61] Huo, D., 2013, Micro-cutting: fundamentals and applications, John Wiley & Sons.

[62] Ng, C. K., Melkote, S. N., Rahman, M., and Kumar, A. S., 2006, "Experimental study of micro-and nano-scale cutting of aluminum 7075-T6", International Journal of Machine Tools and Manufacture, **46**(9), pp: 929-936.

[63] Ozcatalbas, Y., 2003, "Chip and built-up edge formation in the machining of in situ Al4C3–Al composite", Materials & Design, **24**(3), pp: 215-221. http://dx.doi.org/10.1016/S0261-3069(02)00146-2.

[64] Dogra, M., Sharma, V. S., and Dureja, J., 2011, "Effect of tool geometry variation on finish turning–A Review", Journal of Engineering Science and Technology Review, **4**(1), pp: 1-13.

[65] Masounave, J., Youssef, Y. A., Beauchamp, Y., and Thomas, M., 1997, "An experimental design for surface roughness and built-up edge formation in lathe dry turning", International Journal of Quality Science, **2**(3), pp: 167-180.

[66] Jackson, M., 2005, "Primary chip formation during the micromachining of engineering materials", Proceedings of the Institution of Mechanical Engineers, Part B: Journal of Engineering Manufacture, **219**(3), pp: 245-254.

[67] Selvam, M. S., and Radhakrishnan, V., 1973, "Influence of side-flow and built-up edge on the roughness and hardness of the surface machined with a single point tool", Wear, **26**(3), pp: 393-403. http://dx.doi.org/10.1016/0043-1648(73)90189-0.

[68] Childs, T., 2011, "Towards simulating built-up-edge formation in the machining of steel", CIRP Journal of Manufacturing Science and Technology, **4**(1), pp: 57-70.

[69] Heginbotham, W., and Gogia, S., 1961, "Metal cutting and the built-up nose", Proceedings of the Institution of Mechanical Engineers, **175**(1), pp: 892-917.

[70] Boothroyd, G., 1988, Fundamentals of metal machining and machine tools, vol. 28, CRC Press.

[71] Zorev, N. N., 1966, Metal cutting mechanics, Pergamon, headington Hill Hall, Oxford, England.

[72] Shahabi, H., and Ratnam, M., 2010, "In-cycle detection of built-up edge (BUE) from 2-D images of cutting tools using machine vision", The International Journal of Advanced Manufacturing Technology, **46**(9-12), pp: 1179-1189.

[73] Fang, N., Pai, P. S., and Edwards, N., 2010, "Prediction of built-up edge formation in machining with round edge and sharp tools using a neural network approach", International Journal of Computer Integrated Manufacturing, **23**(11), pp: 1002-1014. https://dx.doi.org/10.1080/0951192X.2010.511651.

[74] Ucun, İ., Aslantaş, K., Gökçe, B., and Bedir, F., 2014, "Effect of tool coating materials on surface roughness in micromachining of Inconel 718 super alloy", Proceedings of the Institution of Mechanical Engineers, Part B: Journal of Engineering Manufacture, **228**(12), pp: 1550-1562.

[75] Shaw, M., 1942, "The chemico-physical role of the cutting fluid", Metal Progress, **42**, pp: 85-91.

[76] Chan, K. C., Cheung, C. F., Ramesh, M. V., Lee, W. B., and To, S., 2001, "A theoretical and experimental investigation of surface generation in diamond turning of an

Al6061/SiCp metal matrix composite", International Journal of Mechanical Sciences, **43**(9), pp: 2047-2068. http://dx.doi.org/10.1016/S0020-7403(01)00028-5.

[77] Kovvuri, V. R., 2015, "Experimental Study of Built-up-edge Formation in Micro Milling," Master of Science, Texas A&M University, College Station (TX).

[78] Berestovskyi, D., Hung, W., and Lomeli, P., 2014, "Surface Finish of Ball-End Milled Microchannels", Journal of Micro and Nano-Manufacturing, **2**(4), pp: 041005.

[79] Shaw, M. C., and Cookson, J., 2005, Metal cutting principles, 2nd ed., vol. 2, Oxford university press Oxford, UK.

[80] Wang, M.-Y., and Chang, H.-Y., 2004, "Experimental study of surface roughness in slot end milling AL2014-T6", International Journal of Machine Tools and Manufacture, **44**(1), pp: 51-57.

[81] Rao, P. K., Beyca, O. F., Kong, Z., Bukkapatnam, S. T. S., Case, K. E., and Komanduri, R., 2015, "A graph-theoretic approach for quantification of surface morphology variation and its application to chemical mechanical planarization process", IIE Transactions, **47**(10), pp: 1088-1111. https://dx.doi.org/10.1080/0740817X.2014.1001927.

[82] Komanduri, R., 1993, "Machining and grinding: A historical review of the classical papers", Appl. Mech. Rev, **46**(3), pp: 80-132.

[83] Weule, H., Hüntrup, V., and Tritschler, H., 2001, "Micro-Cutting of Steel to Meet New Requirements in Miniaturization", CIRP Annals - Manufacturing Technology, **50**(1), pp: 61-64. http://dx.doi.org/10.1016/S0007-8506(07)62071-X.

[84] Venkatachalam, S., and Liang, S. Y., 2007, "Effects of ploughing forces and friction coefficient in microscale machining", Journal of manufacturing science and engineering, **129**(2), pp: 274-280.

[85] Ramaswami, R., 1971, "The effect of the built-up-edge(BUE) on the wear of cutting tools", Wear, **18**(1), pp: 1-10. http://dx.doi.org/10.1016/0043-1648(71)90059-7.

[86] Munro, B. H., 2005, Statistical methods for health care research, vol. 1, Lippincott Williams & Wilkins.

[87] Aldrich, J., 1995, "Correlations genuine and spurious in Pearson and Yule", Statistical science, pp: 364-376.

[88] Granger, C. W., 1969, "Investigating causal relations by econometric models and cross-spectral methods", Econometrica: Journal of the Econometric Society, pp: 424-438.

CHAPTER IV

A VISION-BASED MONITORING APPROACH FOR REAL-TIME CONTROL OF LASER ORIGAMI CYBERMANUFACTURING PROCESSES[3]

Preface

Laser origami processes that use sheet precursors offer considerable advantages over traditional powder based additive manufacturing for fast realization of functional complex shapes for custom manufacturing. An in-process monitoring tool that captures shape transformation in real time is necessary to assure cost and quality parity with mass production. Recent advances in optimal image correlations with Aruco markers and sparse regression formulations can lead to fast and accurate real-time process monitoring and quality assurance. We present a spatial regression approach to combine information from multiple low-resolution cameras for real-time monitoring of a laser-origami processes. Experimental investigations on an origami testbed at Texas A&M University suggest that the present approach can provide fast (delays of around 100 ms) and accurate (error rates $NRSME < 5\%$) estimates of geometric features such as the angle of a fold in the laser based origami shape forming process.

---

[3] Reprinted with permission from "A vision-based monitoring approach for real-time control of laser origami cybermanufacturing processes" by Z. Wang, A.S. Iquebal, and S.T.S. Bukkapatnam, Procedia of Manufacturing, 2018, 26: 1307-1317, https://doi.org/10.1016/j.promfg.2018.07.135, Copyright [2018] by Elsevier. For copyright details, please visit https://www.elsevier.com/about/policies/copyright

Introduction

Recent breakthroughs in sensing, additive manufacturing (AM), and data informatics technologies offer an exciting opportunity to fabricate custom and personalized products as part a new paradigm of cybermanufacturing systems [1, 2] at a mass-production cost structure for the industry [89]. The current AM processes that mostly employ powder or wire/filament precursors have some shortcomings in this context. They are slow, requiring hours to print, compared to other manufacturing processes, and are limited to small prototypes (part dimensions < 1m). They often need additional post-processing (e.g., sintering and finishing) to provide functional parts, and expensive material handling and safety systems (e.g., explosion-protected vacuum cleaners, integrated sieves) [90, 91].

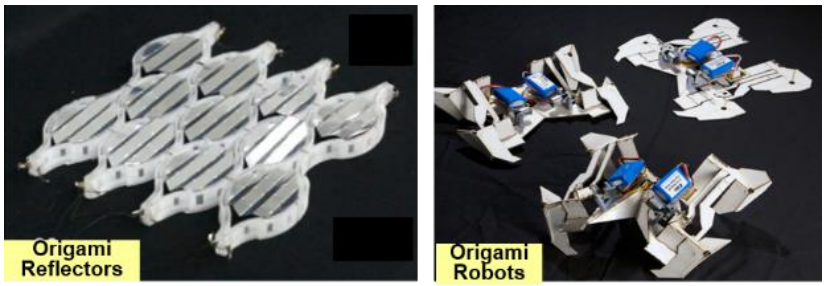

Figure IV-1. Schematic diagram of origami product [92-94].

As an alternative, we have been investigating a novel custom manufacturing approach, referred to as the laser origami process [95], which adapts the cybermanufacturing system paradigm with sheet-based precursors. The current setup, equipped with a laser source and robotic arm(s), can operate a sequence of bend-fold (origami) to realize complicated, innovative and highly load-bearing structures that meet

the functionalities of customization (Figure IV-1). Such a process provides advantages over traditional AM as it is comparatively time-efficient, and sheet precursors are safer and easier to handle than the powder precursors used in conventional additive manufacturing processes [96].

However, laser origami processes are sensitive to the perturbations of the process parameters (e.g., laser power and the moving speed of the laser nozzle); consequently, the open-loop process creates uncertainties in the finished geometric dimensioning. Therefore, real-time control is essential for deploying custom manufacturing systems. Also, for low volume customized production, the relationship connecting the structural transformations achieved during the process with specific settings and adjustments of the process parameters and tool motion is not known a priori. Consequently, process control cannot be hardcoded as part of a process plan and should be part of a real-time service application that uses inputs from online sensors.

Recent advances in image processing offer a promising approach for in-process monitoring of the new laser-origami cybermanufacturing process. Two types of imaging approaches, viz., feature-based and marker-based, have been attempted earlier to track the morphing of objects, such as the sheet material during the origami process [97]. In general, feature-based approaches generate sparse descriptors that contain extracted image features from local regions and use them as reference sets to track the object [98]. For example, the digital image correlation (DIC) method is a vision-based approach which has been widely used for measuring surface deformation of materials and structures subjected to various loadings [99]. This technique determines the surface deformation by comparing the gray

intensity changes of the object surface before and after deformation. However, as with most feature-based approaches, extracting and pairing the localized features of the image in DIC is time-consuming, and the wrong pairing of features in images introduce significant errors in object tracking. In contrast, marker-based tracking can provide accurate, fast, and consistent monitoring in real time, as each marker can be uniquely identified via distinct patterns [100]. For example, fiducial markers have been applied as part of mono- as well as stereo-mode simultaneous localization and mapping (SLAM) [101, 102] for tracking moving objects. The markers are often attached to the tracked object and the background walls, allowing a reconstruction of the object in the environment based on the estimates of camera pose parameters. These approaches often use a state estimation method, such as Kalman filter or its extensions to reduce projection errors of each individual marker [103, 104]. The current marker-based approaches, however, assume that the state space of the object motion is well known. This assumption does not hold in real world situations, especially considering the uncertainty associated with the depth of fields of the cameras. This renders the estimates from the current marker-based approaches inadequate for accurate tracking [103]. Thus far, few monitoring schemes exist to allow closed-loop control of a sheet forming processes including the present laser origami process [96]. The issue of how to visually capture the morphology and precisely track the evolution of origami planes in real-time, essential for ensuring accurate geometric features and dimensioning of highly customized products, has not received much attention in the literature.

In this chapter, we present a vision-based monitoring approach for the laser origami and other sheet metal free-forming processes that can be implemented towards real-time control and quality assurance for such a process. This approach extends Aruco marker-based tracking schemes [105] reported to reconstruct origami objects in camera coordinates. The prior methods have attempted to try to track markers by applying a monocular tracking system [106, 107]. The camera is often mounted on the ceiling of the building or on an aerial robot to increase the field of view of a single camera. Further research [108] applies a stereo camera setup in which the location for each camera is fixed. However, this stereo setup requires extensive calibration whenever the relative position between two cameras changes [109]. Thus, the prior methods may not be suited for laser origami monitoring since camera displacements may differ case by case because of the complex geometry of each highly customized origami product. In contrast, the present method employs a multiple-camera setup with an associated absolute orientation algorithm. This framework allows a rapid image stitching based on marker projections in camera coordinates, a feature which introduces more flexibility for stereo-monitoring. Experimental results suggest that the approach presented here achieves speeds of 10 frames per second and accurate estimations of geometric features during the geometric evolution in the laser origami process. The remainder of this chapter is organized as follows: the technical details of the vision-based monitoring approach are presented in Sec. 2; the implementation of the approach to in-process monitoring of laser cybermanufacturing processes and performance evaluations are reported in Sec. 3; and Sec. 4 provides some concluding remarks.

Approach

Real-time control for the laser origami cybermanufacturing processes requires a monitoring approach with adequately short detection delay (video frame rate at least 5~10fps) to track the morphing of the sheet during the kirigami process, and simultaneously estimate geometric features at high precision (the deviation of the estimates for geometric features needs to be less than 5% of the realized bending angle to meet the minimal requirement for geometric tolerancing as recommended by ISO 2768-1 [110]). Towards realizing this capability, our investigations address the following three intertwined challenges: 1) a mathematical representation of the origami object that allows modeling for sequential laser origami processes; 2) the monocular image tracking using fiducial markers to reconstruct origami objects in camera coordinates; and 3) a multiple-camera setup that can provide a sufficiently broad field of view for consistently tracking complex surface morphing.

Representation of origami object

First, we present a mathematical representation of an origami object in sequential evolutions of sheet morphing. An origami object $\mathbb{O}(\mathcal{M}, \mathcal{A}, \Theta)$ is defined [111], in terms of the facets $\mathcal{M}$, the facet connectivity $\mathcal{A}$, and dihedral angles Θ, detailed as follows.

Origami Facets, $\mathcal{M}$:

The crease pattern based on the origami design divides the sheet precursor into multiple facets. A collection of K facets is represented as $\mathcal{M} = \{M_1, M_2, \dots, M_K\}$. For

example, the initial origami, shown in Figure IV-2, consists of 4 facets M_1, M_2, M_3 and M_4 based on three red-dashed creases $l(1), l(2)$ and $l(3)$.

Facet connectivity, $\mathcal{A}$:

An adjacency mapping $\mathcal{A}: \mathcal{M} \mapsto 2^{\mathcal{M}}$ is applied to describe the facet connectivity. Given a facet M_k, such mapping is defined by $\mathcal{A}(M_k) = \{ M_j \in \mathcal{M} | M_j \sim M_k, \forall j \neq k \}$ where $\sim$ denotes the adjacency between two facets M_j and M_k if they share one edge (crease).

Dihedral angles, Θ:

$\Theta = \left\{ \{\theta_{\mathcal{F}_1} = \vartheta^0_{\mathcal{F}_1}, \dots, \theta_{\mathcal{F}_n} = \vartheta^0_{\mathcal{F}_n}\}, \{\theta_{\mathcal{F}_{-n}} = \vartheta^\tau_{\mathcal{F}_{-n}}\} \right\}$ is the set of all dihedral angles that describe the geometric features between any two connected facets. Here, the subscript $\mathcal{F}_n$ represents two facets affected by the nth folding. It may be noticed that Θ contains two subsets of which the first subset collects all realized dihedral angles up to the nth folding with achieved dihedral angle values $\vartheta^\tau_{\mathcal{F}_n}$'s, and the second subset contains all other dihedral angles $\{\theta_{\mathcal{F}_{-n}}\}$ that wait to be laser-bended from their initial dihedral angle values $\{\vartheta^0_{\mathcal{F}_{-n}}\}$. As shown in Figure IV-2, after two foldings along the creases $l(1)$ (between M_1 and M_3) and $l(2)$ (between M_1 and M_4), $\Theta = \{\{\theta_{13} = \vartheta^\tau_{13}, \theta_{14} = \vartheta^\tau_{14}\}, \{\theta_{12} = \vartheta^0_{12}\}\}$, where initial states of all dihedral angles $\vartheta^0_{12} = \vartheta^0_{13} = \vartheta^0_{14} = 0°$ and the achieved angle values $\vartheta^\tau_{13} = \vartheta^\tau_{14} = 90°$.

In general, the evolution of the origami object $\mathbb{O}_n(\mathcal{M}, \mathcal{A}, \Theta)$ during the nth laser bending step can be mathematically represented as follows: select a crease line $l(n)$ to generate the nth fold, and then determine the associated $\mathcal{F}_n$ that includes two facets

affected by this folding. Next, apply a defocused laser along the crease line $l(n)$ and fold the origami until a desired angle value $\vartheta^{\tau}_{\mathcal{F}_n}$ is realized. As the illustrative example shown in Figure IV-2, each fold over a crease line constitutes on laser bending step. The generation of an origami product is complete when all desired dihedral angles are realized, i.e., $\Theta = \{\{\theta_{\mathcal{F}_n} = \vartheta^{\tau}_{\mathcal{F}_n}; for\ all\ n\}, \{\emptyset\}\}$.

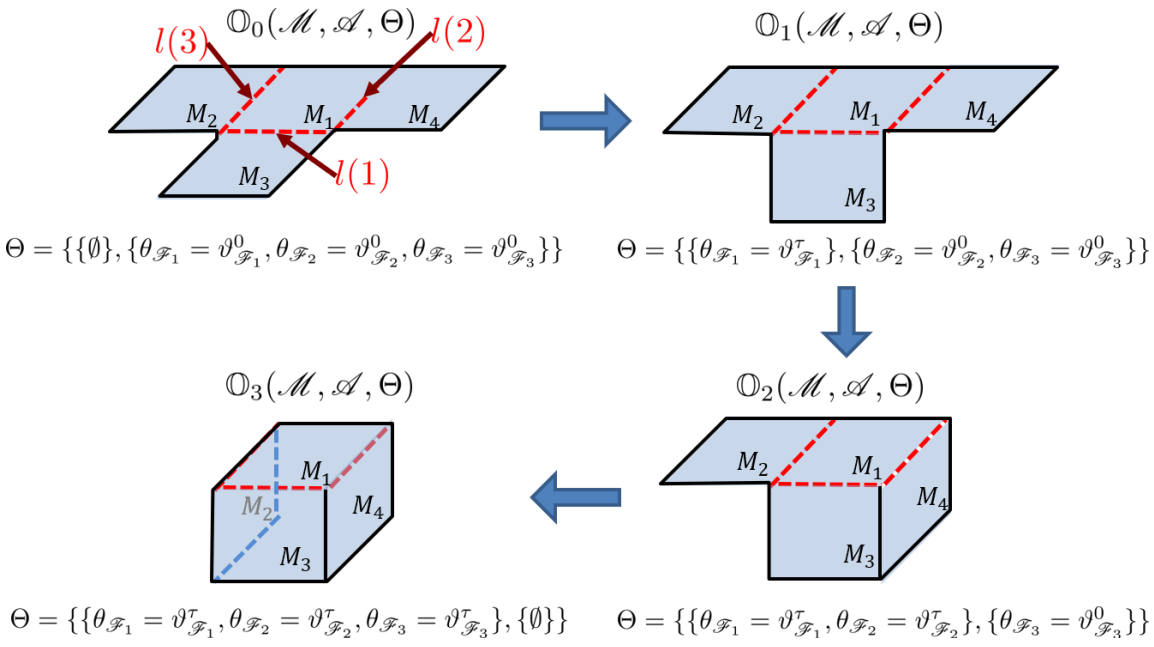

Figure IV-2. An illustrative example on representation of an origami object. (reprinted with permission)

Camera/image based 3D reconstruction using planar markers

One key aspect of our vision-based approach is to consistently track the geometric evolution of the sheet in real time during the origami operations. Two types of vision-based approaches, *viz.*, feature-based and marker-based, have been widely used for object tracking [97]. In general, feature-based approaches extract elementary descriptors that

contain visual features, such as color, texture and motion from highly localized areas, and use them as reference sets for real-time object recognition and tracking [98]. However, the feature extraction and descriptors pairing for such a monitoring scheme are time-consuming, and descriptor mismatches between consecutive video frames may cause inconsistent object tracking. On the other hand, the marker-based tracking approach provides a fast, accurate and consistent monitoring scheme as each fiducial marker can be uniquely identified via its distinct binary patterns. An earlier work [100] investigated the performances of different fiducial marker libraries. It suggests that the Aruco marker has advantages over other competitive marker libraries as it obtains both the minimal error rate on marker border estimation and the minimal inter-marker confusion error with comparatively short computation time (e.g., detection delay of all markers in the dictionary is less than 10 ms). Therefore, as shown in Figure IV-3, we apply the planar markers from Aruco library [112] on a non-curved crease pattern origami plate (i.e., each facet lies in a plane). Formally, the planar markers are denoted by planar segments $\{m_j\}$ $(j = 1,2, \dots, J)$, and $m_j \in M_k$ represents that the marker m_j is embedded onto the origami facet M_k.

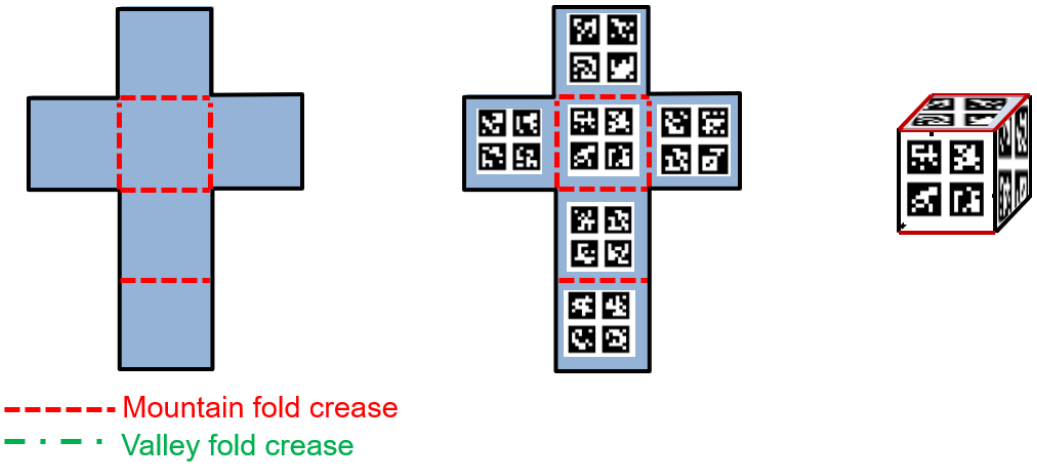

Figure IV-3. Representation of origami using planar markers. (reprinted with permission)

The use of such planar markers facilitates fast and accurate the registration of each facet in the camera coordinates. Figure 4 illustrates how the fiducial markers are projected into the camera coordinate system. Let four vertices of a marker m_j in the marker-reference coordinate system be $\{\mathcal{P}_i\} = \{(U_i, V_i, W_i)^T\}$. For example, the coordinates of the four edges of a the marker shown in the figure are $\{\mathcal{P}_1, \mathcal{P}_2, \mathcal{P}_3, \mathcal{P}_4\} = \{\left(-\frac{\rho}{2}, \frac{\rho}{2}, 0\right)^T, \left(\frac{\rho}{2}, \frac{\rho}{2}, 0\right)^T, \left(-\frac{\rho}{2}, -\frac{\rho}{2}, 0\right)^T, \left(\frac{\rho}{2}, -\frac{\rho}{2}, 0\right)^T\}$, and ρ is the predefined marker length. x^C, y^C and z^C in Figure 4 are three axes of the camera coordinate system. The mapping of $\{\mathcal{P}_i\}$ (red-dotted in Figure 4) from the marker-reference coordinates into the camera coordinates $\{P_i\} = \{(x_i, y_i, z_i)^T\}$ is given by

$$[x\ y\ z]^T = [R|T][U\ V\ W\ 1]^T \tag{1}$$

where we have the rotation matrix $R = [[r_{11}\ r_{21}\ r_{31}]^\top, [r_{12}\ r_{22}\ r_{32}]^\top, [r_{13}\ r_{23}\ r_{33}]^\top]$ and the translation vector $T = [t_1\ t_2\ t_3]^T$. Both R and T can be estimated by solving a perspective-n-point (PnP) problem (in this case, $n = 4$ for all corners) in the marker-

reference coordinates $\{\mathcal{P}_i\}$, and their corresponding 2D projections on the image plane $\{p_i\} = \{(u_i, v_i)^T\}$ [113]. This solution follows a perspective projection model as follows:

$$z \cdot [u\ v\ 1]^\top = K \cdot [R|T][U\ V\ W\ 1]^\top \quad \textbf{(2)}$$

where $K = [[f\ \ 0\ \ 0]^\top, [0\ \ f\ \ 0]^\top, [u_c\ \ v_c\ \ 1]^\top]$ is the intrinsic camera parameter matrix, f is the focal length of the camera, and $(u_c, v_c)^T$ is the focus center on the image plane (in unit of pixels). Then the following procedure provides a solution to the camera pose estimation:

We first define $\Gamma \stackrel{\text{def}}{=} K \cdot [R|T] = [[\gamma_{11}\ \ \gamma_{21}\ \ \gamma_{31}]^\top, [\gamma_{12}\ \ \gamma_{22}\ \ \gamma_{32}]^\top, [\gamma_{13}\ \ \gamma_{23}\ \gamma_{33}]^\top, [\gamma_{14}\ \gamma_{24}\ \gamma_{34}]^\top]$. Then, the estimated values of (u_i, v_i) can be expressed as:

$$(\gamma_{31}U_i\ + \gamma_{32}V_i + \gamma_{33}W_i + 1)\hat{u}_i = \gamma_{11}U_i\ + \gamma_{12}V_i + \gamma_{13}W_i + \gamma_{14} \quad (3)$$

$$(\gamma_{31}U_i\ + \gamma_{32}V_i + \gamma_{33}W_i + 1)\hat{v}_i = \gamma_{21}U_i\ + \gamma_{22}V_i + \gamma_{23}W_i + \gamma_{24} \quad (4)$$

Here, Eqs. 3 and 4 form the implicit system of equations to obtain the estimates $\hat{u}_i$ and $\hat{v}_i$. The actual functional relations explicitly connecting $\hat{u}_i$ and $\hat{v}_i$ to Γ and $\mathcal{P}_i$ may be represented as follows.

$$\hat{u}_i = g_1(\Gamma, \mathcal{P}_i) = u_i\ + \epsilon_i, \quad \epsilon_i \sim N(0, \sigma^2) \quad (5)$$

$$\hat{v}_i = g_2(\Gamma, \mathcal{P}_i) = v_i + \varepsilon_i, \quad \varepsilon_i \sim\ N(0, \sigma^2) \quad (6)$$

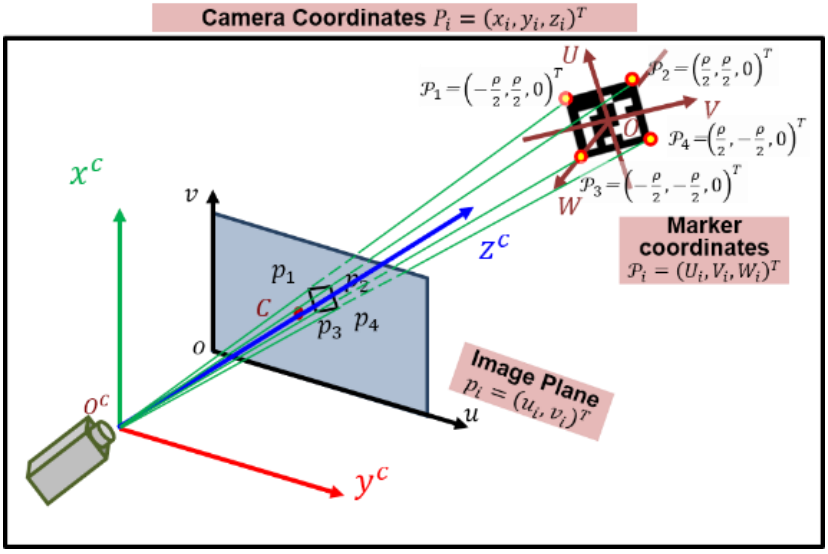

Figure IV-4. Schematic diagram of marker reconstruction in camera coordinate system. (reprinted with permission)

Here, Eqs. 5 and 6 also represent the relationship between the estimates and the ground truth of the projected points (note that ϵ_i and ε_i are independent white noises with the variance σ^2). The likelihood of Γ given (u_i, v_i)'s could be therefore expressed as follows:

$$L = \Pi_i p(\hat{u}_i|u_i)p(\hat{v}_i|v_i)$$

$$= \Pi_i \, exp\left(-\frac{(u_i-\hat{u}_i)^2}{\sigma^2}\right) exp\left(-\frac{(v_i-\hat{v}_i)^2}{\sigma^2}\right) + C_1 \quad (7)$$

We apply the Levenberg-Marquardt algorithm to find the optimal solution of Γ by minimizing the negative log likelihood:

$$-logL = \sum_i \left[\frac{(u_i-\hat{u}_i)^2}{\sigma^2} + \frac{(v_i-\hat{v}_i)^2}{\sigma^2}\right] + C_2 \quad (8)$$

where C_1 and C_2 are two constants. Then a QR decomposition on the optimal solution $\hat{\Gamma}$ can recover an upper triangle matrix, i.e., the intrinsic camera matrix K, and an orthogonal matrix $[\hat{R}|\hat{T}]$ that contains the camera pose [114]. Based on estimated $\hat{R}$ and $\hat{T}$, the projections of markers in the single camera coordinates can be obtained from Eq. 1.

Absolute orientation problem in a multiple-camera setup

A single camera setup has serious drawbacks to track the laser origami process as it performs the sequence of folding operations, especially to generate complicated geometries. Oftentimes, the facets and or markers thereon may be far divergent from the camera's line of focus (depicted in Figure 4 as a thick blue line emanating from the camera with an arrow). Additionally, certain marker planes can become significantly tilted parallel to the camera's line of focus, especially while realizing a sharp dihedral angle, that causes the pose estimation errors to increase, and affects the reprojection accuracy of the origami plates [115]. Even worse, this monocular vision-based approach may lose its tracking targets during complex shape realization. To overcome this shortcoming, we apply a multiple-camera setup in which each camera is set at a different orientation towards the origami object. By combining the information from each camera, such a setup provides a broad field of view that assures a consistent monitoring of the origami morphing.

However, the multiple-camera setup introduces an absolute orientation problem: since the cameras are oriented at different directions relative to each other and the tracking object, the projections from different camera coordinates need to be transformed into a uniform coordinate system.

To find the spatial translation of the coordinates between two cameras (denoted by c_1 and c_2), let one of the cameras be the reference camera coordinate system (in this case camera c_2 is selected). Then, the solution to this spatial translation between two camera coordinate systems of c_1 and c_2 can be obtained by minimizing the transformation errors in terms of the sum of squares, which is formulated as:

$$\min_{\substack{s\in\mathbb{R}^+, R\in\mathbb{R}^{3\times3} \\ and\ R^\top=R^{-1}}} \sum_{i=1}^{I} ||P_{m_j,i,c_2} - s\cdot R\left(P_{m_j,i,c_1}\right) - T||^2 \quad (9)$$

where $||\cdot||$ is the l_2-norm and s is the scale ($s > 0$). Horn [116] provides a closed-form solution for this absolute orientation problem, which is computationally efficient compared to most nonlinear optimization algorithms. First, the mean value of the projection points was subtracted from the original projections to generate the set of points $P'_{m_j,i,c_2} = P_{m_j,i,c_2} - \frac{1}{I}\sum_{i=1}^{I} P_{m_j,i,c_2}$ of which the centroid is at the origin. Then the objective function could be rewritten as: $\sum_{i=1}^{I}||P'_{m_j,i,c_2}||^2 - 2s\cdot\sum_{i=1}^{I} P'_{m_j,i,c_2}\cdot R\,(P'_{m_j,i,c_1}) + s^2\cdot \sum_{i=1}^{I}||P'_{m_j,i,c_1}||^2$. The closed-form solution to minimize this objective function can be expressed in Eqs. 10 and 11. Here the vector $q = \left[q_0, q_x, q_y, q_z\right]^T$ is the coefficient of the unit quaternion solution to the problem, obtained from the eigenvector with respect to the largest eigen of matrix N in Eq. 12, where $S_{xx} = \sum_{i=1}^{I} x'_{m_j,i,c_1}\, x'_{m_j,i,c_2}$, $S_{xy} = \sum_{i=1}^{I} x'_{m_j,i,c_1}\, y'_{m_j,i,c_2}$, $S_{xz} = \sum_{i=1}^{I} x'_{m_j,i,c_1}\, z'_{m_j,i,c_2}$ and $x'_\cdot$, $y'_\cdot$ and $z'_\cdot$ are the values of three coordinates of the projection point $P'_\cdot$.

$$R = \begin{bmatrix} q_0^2 + q_x^2 - q_y^2 - q_z^2 & 2(q_x q_y - q_0 q_z) & 2(q_x q_z + q_0 q_y) \\ 2(q_y q_x + q_0 q_z) & q_0^2 - q_x^2 + q_y^2 - q_z^2 & 2(q_y q_z - q_0 q_x) \\ 2(q_z q_x - q_0 q_y) & 2(q_z q_y + q_0 q_x) & q_0^2 - q_x^2 - q_y^2 + q_z^2 \end{bmatrix} \quad (10)$$

$$s = \frac{\sum_{i=1}^{I} P_{m_j,i,c_2} \cdot R(P_{m_j,i,c_1})}{\sum_{i=1}^{I} ||P_{m_j,i,c_1}||^2} \quad (11)$$

$$N = \begin{bmatrix} (S_{xx} + S_{yy} + S_{zz}) & S_{yz} - S_{zy} & S_{zx} - S_{xz} & S_{xy} - S_{yx} \\ S_{yz} - S_{zy} & (S_{xx} - S_{yy} - S_{zz}) & S_{xy} + S_{yx} & S_{zx} + S_{xz} \\ S_{zx} - S_{xz} & S_{xy} + S_{yx} & (-S_{xx} + S_{yy} - S_{zz}) & S_{yz} + S_{zy} \\ S_{xy} - S_{yx} & S_{zx} + S_{xz} & S_{yz} + S_{zy} & (-S_{xx} - S_{yy} + S_{zz}) \end{bmatrix} \quad (12)$$

It may be noted that the Hamilton's quaternion representation offers significant advantages compared to other formulations of spatial translation such as the orthogonal matrix and Euler angles [117] in the following ways: 1) it reduces the dimensions (compared to the rotation matrix and translation vector), which saves computation time, 2) a unit quaternion representation ensures that recovered solution of rotation matrix is orthogonal, and 3) it can represent multiple transformations simply by taking a product of quaternions because of its homomorphism property [118]. The time complexity and accuracy of this absolute orientation method are further discussed in Sec. 3.1.

Sequential monitoring of the evolution of origami

After 3D reconstruction in a uniform coordinate system, a linear regression, Eq. 13, is applied to estimate the plane function of facet M_k:

$$Z = \beta X + \epsilon \quad (13)$$

where $\boldsymbol{X} = [\left(1, x_{m_j,i,c_1}, y_{m_j,i,c_1}\right)^T, \left(1, x^{c_1}_{m_j,i,c_2}, y^{c_1}_{m_j,i,c_2}\right)^T]$ is the input including x and y values in coordinates for all projection points ($i = 1,2,3, \dots, \mathbb{N}$), over every $\forall m_j \in M_k$, $\boldsymbol{Z} = \left[z_{m_j,i,c_1}, z^{c_1}_{m_j,i,c_2}\right]$ is all corresponding z values from those projection points for $\forall m_j \in M_k$, $\boldsymbol{\beta} = [\beta_0^{(M_k)}, \beta_1^{(M_k)}, \beta_2^{(M_k)}]$ is the vector of regression coefficients fitting the plane function of facet M_k, and $\boldsymbol{\epsilon} \sim \mathcal{N}(\mathbf{0}, \boldsymbol{I}\sigma^2)$ is the Gaussian noise. Suppose the surface planes of two connected facets, M_k and M_r, are fitted by: Facet k: $-\beta_1^{(M_k)} \cdot x - \beta_2^{(M_k)} \cdot y + z = \beta_0^{(M_k)}$ and Facet r: $-\beta_1^{(M_r)} \cdot x - \beta_2^{(M_r)} \cdot y + z = \beta_0^{(M_r)}$.Then the estimate of geometric feature in terms of the dihedral angle between M_k and M_r can be formulated as a function of regression coefficients:

$$cos\hat{\theta}_{kr} = \frac{\left|\beta_1^{(M_k)} \cdot \beta_1^{(M_r)} + \beta_2^{(M_k)} \cdot \beta_2^{(M_r)} + 1\right|}{\sqrt{\left[\beta_1^{(M_k)}\right]^2 + \left[\beta_2^{(M_k)}\right]^2 + 1} \cdot \sqrt{\left[\beta_1^{(M_r)}\right]^2 + \left[\beta_2^{(M_r)}\right]^2 + 1}} \tag{14}$$

For the present application, $\hat{\theta}_{kr}$ is estimated at every 120 *ms* time step, and is provided as an input for real-time tuning of the laser power and the scanning rate. In addition, we include the pseudocode for the whole monitoring approach in Appendices.

Experimental case studies

The performance of the present approach was evaluated for the monitoring of the sheet precursor evolution based on the experiments conducted on a laser origami testbed at Texas A&M University. The laser origami setup, shown in Figure 5, was equipped with one 4-axis robotic arm that could precisely place the workpiece, i.e., sheet precursors attached with fiducial markers, in the laser machine coordinates (with displacement

precision ~ 0.2mm), in addition to a multiple digital camera setup for monitoring the surface morphing, and a CO_2 laser source with 10.6 μm wavelength and power up to 100 watts.

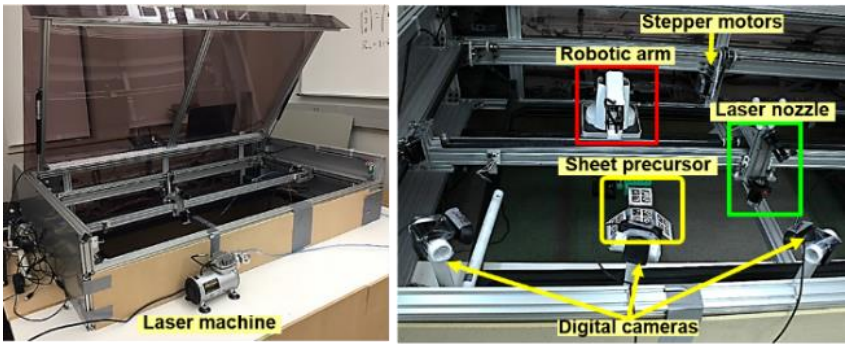

Figure IV-5. Laser origami setup. (reprinted with permission)

Investigations into accuracy and time complexity

First, we investigated the time efficiency and the accuracy of the method. Here, we reconstruct the planar markers in the camera coordinates using a sampled mesh grid with a specific number of projection points $\mathbb{N}$. The value of $\mathbb{N}$ is crucial for the overall time complexity {including complexities of absolute orientation problem $\mathcal{O}(\mathbb{N})$ and the linear regression model $\mathcal{O}(\mathbb{N})$ [119]} and the goodness of fit for plane functions. Therefore, we conducted a set of experiments to investigate the impact of $\mathbb{N}$ on 1) the detection delay for the image tracking and 2) the estimation accuracy of the geometric features.

In total, six settings of resolutions of mesh grid points (i.e., $\mathbb{N}$) were selected. For each setting of $\mathbb{N} = \{2^2, 3^2, 5^2, 11^2, 21^2, 51^2\}$, the performance of the present method was evaluated in terms of the root mean square error ($RMSE$), goodness of fit (R^2 value) and

time delay of detection. The presented approach was computed 20 times based on the same number of the video frames taken when monitoring a completely realized dihedral angle between two origami plates (M_1 and M_2). The performance estimates are summarized as box plots in Figure 6. Each boxplot captures the variation of a performance metric, namely, the time delay for detection (Figure 6a), RMSE values (Figure 6b), are R^2 values for two origami planes M_1 and M_2 (Figures 6c&d) relative to mesh grid resolution $\mathbb{N}$. It may be noted that as $\mathbb{N}$ increases, R^2 increases to plateau to its maximum (0.95) for $\mathbb{N} > 121$, and $RMSE$ that calculates the error between estimated dihedral angle and its ground truth decreases to reach a minimum of 1.0641 for $\mathbb{N} > 121$. This may be due to that as the mesh grid points increase beyond a certain resolution, more redundant sample points are introduced as they are highly spatial-correlated and consequently they would not further improve the estimation accuracy. These results imply that given the camera resolution as well as the rate of change in the slopes and curvatures over the surface, there is a maximum resolution beyond which the prediction accuracies do not improve and latency worsens.

Moreover, the results from the time consumption in Figure 6a) suggest that the time delay increases significantly as $\mathbb{N}$ surpasses 400. With the consideration of the time delay, we select $\mathbb{N} = 25$ to sample the mesh grid of each marker to obtain a minimal estimation error ($NRSME \approx 2.14\%$) as well as a fast computation speed (delay of detection is around 100 ms).

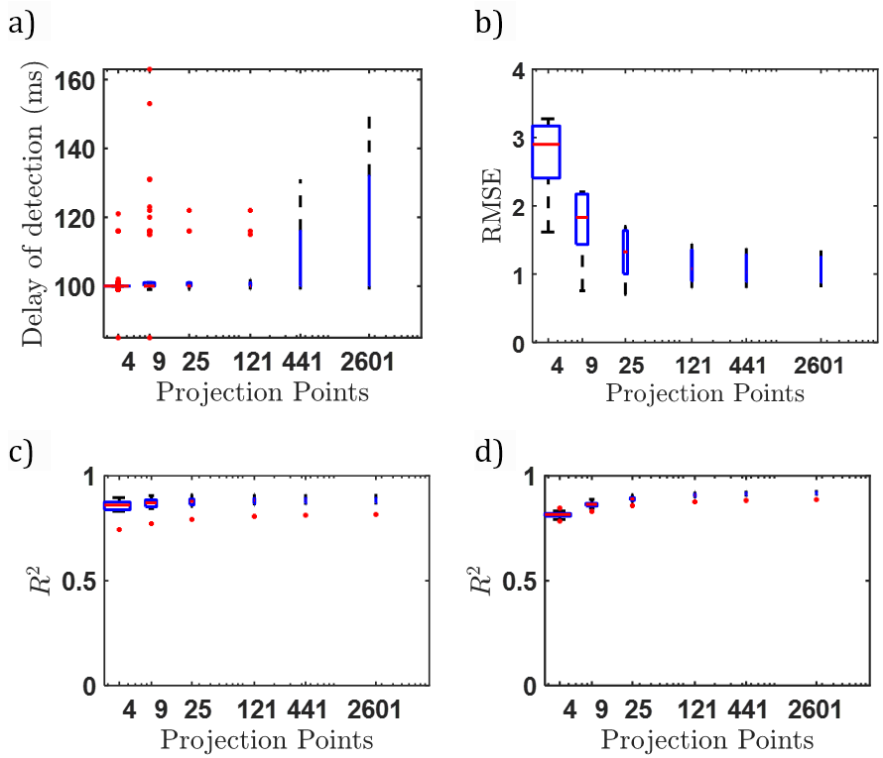

Figure IV-6. Experimental results of a) boxplot of time delays vs *N*, b) boxplot of RMSE vs $\mathbb{N}$, and goodness of fit in terms of R^2 values for two planes as depicted in c) and d). (reprinted with permission)

Sequential bending for realizing origami box

Next, we conducted laser origami bending on a workpiece (as illustrated in Figure 7) to achieve an origami box. The process involves three bends: on selected creases $l(1), l(2)$, and $l(3)$. For the nth folding (as $n = 1,2,3$), based on the crease $l(n)$ and the connectivity mapping $\mathcal{A}$, we generate the subset $\mathcal{F}_n \in \mathcal{M}$, which includes the facets affected by the nth folding. Our approach is then applied for the monitoring of the origami plate morphing on $\mathcal{F}_n$ and computing the geometric feature $\theta_{\mathcal{F}_n}$ in real time. Figure 8 shows step-by-step video footage of the origami evolution followed by the folding

sequence of $l(1), l(2)$, and $l(3)$. The box origami was achieved until all the geometric angles were realized.

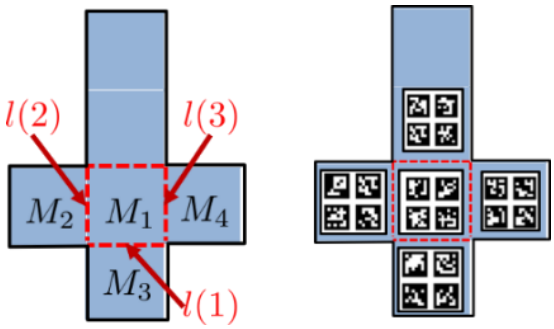

Figure IV-7. Workpiece of origami box with folding sequence as $l(1), l(2)$ and $l(3)$. (reprinted with permission)

Figure 9 summarizes the evolutions of the dihedral angles θ_{13}, θ_{12} and θ_{14} with respect to the crease sequence $l(1)$, $l(2)$ and $l(3)$. It may be noticed that significant variations on dihedral angles were observed before desired θ_{12} and θ_{14} were realized. This phenomenon may be due to the temperature gradient mechanism (TGM): as the defocused laser ray is applied on restricted area (along the crease pattern), an inhomogeneous temperature distribution is generated, introducing non-uniform thermal stress along thickness direction, and consequently, the origami plate bends towards the laser beam. The accuracy of the monitoring approach was then evaluated by a normalized root mean square error ($NRMSE$), which can be formulated as:

$$NRMSE = \sqrt{\frac{1}{\sum_n^N Fr^{(n)} - Fr_0^{(n)}} \sum_n^N \sum_{fr=Fr_0^{(n)}}^{Fr^{(n)}} \left(\hat{\theta}_{\mathcal{F}_n}^{(fr)} - \theta_{\mathcal{F}_n}\right)} / \bar{\theta} \qquad (15)$$

where $\hat{\theta}_{\mathcal{F}_n}^{(fr)}$ is the estimate of the realized dihedral angle for the nth bending at video frame fr. $\theta_{\mathcal{F}_n}$ is the ground truth of the realized bending angle measured by a digital

protractor (with measurement error less than 0.3 °). Since the video recordings of three bending angles, $\theta_{\mathcal{F}_n}$'s, were of different durations, we applied a weighted mean value $\bar{\theta}$ for the ground truth measurement, i.e., $\bar{\theta} = \sum_n^N w_n \theta_{\mathcal{F}_n}$ where w_n is the weight such that $\sum_n w_n = 1$ and $w_n \propto Fr^{(n)} - Fr_0^{(n)}$. Here $Fr_0^{(n)}$ and $Fr^{(n)}$ represent the starting and ending frames of the recording of the realized $\theta_{\mathcal{F}_n}$, and the weight, w_n, is thereby proportional to the footage duration of the nth bending. Based on the recordings of the origami box realization, an $NRMSE$ of 4.36% was obtained for the geometric feature estimation, suggesting that the presented approach can provide an accurate closed-loop feedback for laser origami processes.

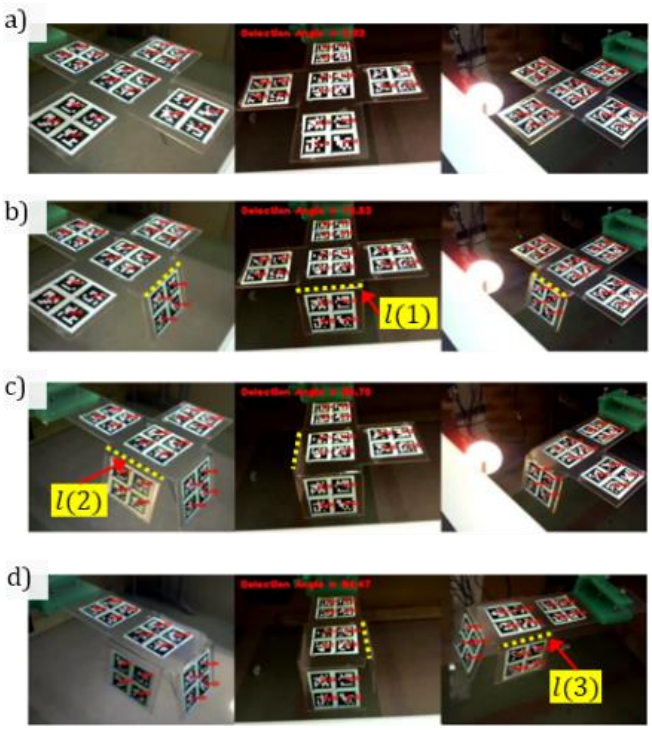

Figure IV-8. Experimental results for a box bending: a) is the initial workpiece with attached planar markers, b), c) and d) capture the states of origami plate after the laser bendings along the crease patterns $l(1), l(2)$ and $l(3)$ (yellow-dashed), respectively. (reprinted with permission)

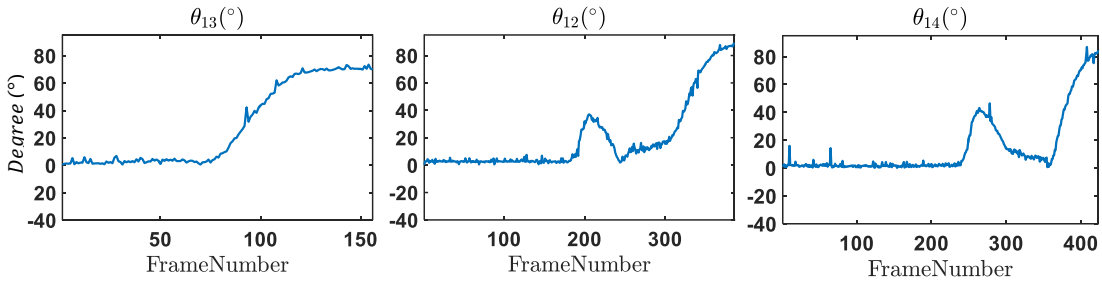

Figure IV-9. Estimates of the dihedral angles θ_{13}, θ_{12} and θ_{14} during the laser bendings along the crease patterns $l(1), l(2)$ and $l(3)$, respectively. (reprinted with permission)

Conclusions

In this chapter, we have presented a vision-based monitoring approach that addresses the core issue in realizing a viable cybermanufacturing system that employs sheet precursors for custom fabrication of freeform shell geometries. The present approach allows real-time tracking of the bending process to control sheet forming processes, particularly laser origami processes. A mathematical representation of an origami object is presented for modeling the sequential evolution of the origami plate. The monitoring approach applies planar markers and a multiple-camera setup to consistently track origami plates and estimate the states of the origami process. Case studies suggest that the present approach can yield an accurate estimation ($NRSME \leq 5\%$) with video frame rate≈10fps. Therefore, it can be a viable tool for providing closed-loop feedback for in-process quality control of the laser-origami cybermanufacturing process.

There are several practical and theoretical issues that need to be addressed in the future. For example, upgrading the hardware setup by introducing 6-axis robotic arms may

be necessary for achieving complicated foldings (e.g., dihedral angle $\theta = 180°$), and a randomization sampling scheme for the mesh grid should be presented to reduce spatial correlations and improve computation efficiency.

Acknowledgements

I would thank Dr. Zhujiang (Jason) Wang and Mr. Woo Hyun Ko for their lead role with installing the imaging setup as part of the laser origami machine and its control interface, and for all the help with conducting the experimental study reported in this chapter. They also gratefully acknowledge the support from the National Science Foundation (#ECCS-1547075).

References

[1] Kim, K.-D., and Kumar, P. R., 2012, "Cyber–physical systems: A perspective at the centennial", Proceedings of the IEEE, **100**, pp: 1287-1308.

[2] Lee, J., Bagheri, B., and Jin, C., 2016, "Introduction to cyber manufacturing", Manufacturing Letters, **8**, pp: 11-15.

[89] Bukkapatnam, S., and Srinivasa, A., 2015, http://tees.tamu.edu/media/197462/cyber-manufacturing-primer.pdf.

[90] Everton, S. K., Hirsch, M., Stravroulakis, P., Leach, R. K., and Clare, A. T., 2016, "Review of in-situ process monitoring and in-situ metrology for metal additive manufacturing", Materials & Design, **95**, pp: 431-445.

[91] Krishnan, M., Atzeni, E., Canali, R., Manfredi, D., Calignano, F., Ambrosio, E., and Iuliano, L., 2013, "Influence of post‐processing operations on mechanical properties of AlSi10Mg Parts by DMLS", Proc. of The 6th International Conference on High Value Manufacturing: Advanced Research in Virtual and Rapid Prototyping, Leiria, Portugal, CRC Press, p. 243.

[92] Miyashita, S., Guitron, S., Li, S., and Rus, D., 2017, "Robotic metamorphosis by origami exoskeletons", Science Robotics, **2**(10), pp: eaao4369. https://dx.doi.org/10.1126/scirobotics.aao4369.

[93] Wang, W., Li, C., Rodrigue, H., Yuan, F., Han, M. W., Cho, M., and Ahn, S. H., 2017, "Kirigami/Origami‐Based Soft Deployable Reflector for Optical Beam Steering", Advanced Functional Materials, **27**(7), pp: 1604214.

[94] Onal, C. D., Tolley, M. T., Wood, R. J., and Rus, D., 2015, "Origami-inspired printed robots", IEEE/ASME Transactions on Mechatronics, **20**(5), pp: 2214-2221.

[95] Piqué, A., Mathews, S. A., Charipar, N. A., and Birnbaum, A. J., 2012, "Laser origami: a new technique for assembling 3D microstructures", Proc. of Proceedings of SPIE, pp: 82440B-82440B.

[96] Mueller, S., Kruck, B., and Baudisch, P., 2013, "LaserOrigami: laser-cutting 3D objects", Proc. of Proceedings of the SIGCHI Conference on Human Factors in Computing Systems, ACM, pp: 2585-2592.

[97] Yang, H., Shao, L., Zheng, F., Wang, L., and Song, Z., 2011, "Recent advances and trends in visual tracking: A review", Neurocomputing, **74**(18), pp: 3823-3831.

[98] Yu, G., and Morel, J.-M., 2011, "ASIFT: An algorithm for fully affine invariant comparison", Image Processing On Line, **1**, pp: 11-38.

[99] Pan, B., Qian, K., Xie, H., and Asundi, A., 2009, "Two-dimensional digital image correlation for in-plane displacement and strain measurement: a review", Measurement science and technology, **20**(6), pp: 062001.

[100] Garrido-Jurado, S., Muñoz-Salinas, R., Madrid-Cuevas, F. J., and Marín-Jiménez, M. J., 2014, "Automatic generation and detection of highly reliable fiducial markers under occlusion", Pattern Recognition, **47**(6), pp: 2280-2292. https://doi.org/10.1016/j.patcog.2014.01.005.

[101] Lim, H., and Lee, Y. S., 2009, "Real-time single camera SLAM using fiducial markers", Proc. of ICCAS-SICE, 2009, IEEE, pp: 177-182.

[102] Muñoz-Salinas, R., Marín-Jimenez, M. J., Yeguas-Bolivar, E., and Medina-Carnicer, R., 2016, "Mapping and Localization from Planar Markers", arXiv preprint arXiv:1606.00151.

[103] Migliore, D., Rigamonti, R., Marzorati, D., Matteucci, M., and Sorrenti, D. G., 2009, "Use a single camera for simultaneous localization and mapping with mobile object tracking in dynamic environments", Proc. of ICRA Workshop on Safe navigation in open and dynamic environments: Application to autonomous vehicles, pp: 12-17.

[104] Ceriani, S., Marzorati, D., Matteucci, M., and Sorrenti, D. G., 2014, "Single and multi camera simultaneous localization and mapping using the extended Kalman Filter", Journal of Mathematical Modelling and Algorithms in Operations Research, **13**(1), pp: 23-57.

[105] Garrido-Jurado, S., Muñoz-Salinas, R., Madrid-Cuevas, F. J., and Medina-Carnicer, R., 2016, "Generation of fiducial marker dictionaries using Mixed Integer Linear Programming", Pattern Recognition, **51**(Supplement C), pp: 481-491. https://doi.org/10.1016/j.patcog.2015.09.023.

[106] Guérin, F., Guinand, F., Brethé, J.-F., Pelvillain, H., and Zentout, A., 2015, "Vision based target tracking using an unmanned aerial vehicle", Proc. of Advanced Robotics and its Social Impacts (ARSO), 2015 IEEE International Workshop on, IEEE, pp: 1-6.

[107] Borstell, H., Pathan, S., Cao, L., Richter, K., and Nykolaychuk, M., 2013, "Vehicle positioning system based on passive planar image markers", Proc. of Indoor Positioning and Indoor Navigation (IPIN), 2013 International Conference on, IEEE, pp: 1-9.

[108] Achtelik, M., Tianguang, Z., Kuhnlenz, K., and Buss, M., 2009, "Visual tracking and control of a quadcopter using a stereo camera system and inertial sensors", Proc. of 2009 International Conference on Mechatronics and Automation, 9-12 Aug. 2009, pp: 2863-2869.

[109] Hartley, R., and Zisserman, A., 2004, "Epipolar geometry and the fundamental matrix", Multiple View Geometry in Computer Vision, Cambridge University Press, pp: 239-261.

[110] ISO, 1989, "Tolerances for linear and angular dimensions without individual tolerance indications (ISO 2768-1)," https://www.iso.org/standard/7748.html.

[111] Ida, T., Takahashi, H., Marin, M., and Ghourabi, F., 2007, "Modeling origami for computational construction and beyond", Proc. of International Conference on Computational Science and Its Applications, Springer, pp: 653-665.

[112] Bradski, G., 2000, "The OpenCV Library", Dr. Dobb's Journal of Software Tools. citeulike-article-id:2236121.

[113] Zhang, Z., 2000, "A flexible new technique for camera calibration", IEEE Transactions on pattern analysis and machine intelligence, **22**(11), pp: 1330-1334.

[114] Golub, G. H., and Van Loan, C. F., 2012, Matrix computations, vol. 3, JHU Press.

[115] Schweighofer, G., and Pinz, A., 2006, "Robust pose estimation from a planar target", IEEE transactions on pattern analysis and machine intelligence, **28**(12), pp: 2024-2030.

[116] Horn, B. K., 1987, "Closed-form solution of absolute orientation using unit quaternions", Journal of the Optical Society of America A, **4**(4), pp: 629-642.

[117] Familton, J. C., 2015, "Quaternions: a history of complex noncommutative rotation groups in theoretical physics", arXiv preprint arXiv:1504.04885.

[118] Thomas, F., 2014, "Approaching dual quaternions from matrix algebra", IEEE Transactions on Robotics, **30**(5), pp: 1037-1048.

[119] Eggert, D. W., Lorusso, A., and Fisher, R. B., 1997, "Estimating 3-D rigid body transformations: a comparison of four major algorithms", Machine vision and applications, **9**(5-6), pp: 272-290.

CHAPTER V

ACOUSTIC EMISSION (AE) CHARACTERIZATION OF NATURAL FIBER REINFORCED PLASTIC (NFRP) COMPOSITE MACHINING USING A RANDOM FOREST MACHINE LEARNING MODEL[4]

Preface

Natural fiber reinforced plastic (NFRP) composites are eliciting an increased interest across industrial sectors, as they combine a high degree of biodegradability and recyclability with unique structural properties. These materials are machined to create components that meet the dimensional and surface finish tolerance specifications for various industrial applications. The heterogeneous structure of these materials—resulting from different fiber orientations and their complex multi-scale structure —introduces a distinct set of material removal mechanisms that inherently vary over time. This structure has an adverse effect on the surface integrity of machined NFRPs. A real-time monitoring approach is therefore desirable for timely intervention for quality assurance. Acoustic emission (AE) sensors that capture the elastic waves generated from the plastic deformation and fracture mechanisms have potential to characterize these abrupt variations in the material removal mechanisms. However, the relationship connecting AE waveform

[4] Reprinted with permission from "Acoustic Emission(AE) characterization of natural fiber reinforced plastic (NFRP) composite machining using a random forest machine learning model," by Z. Wang, F. Chegdani, N. Yalamarti, B. Takabi, B. Tai, M. E. Mansori, and S. T. Bukkapatnam, Journal of Manufacturing Science and Engineering, pp. 1-40. Copyright [2020] by the American Society of Mechanical Engineers.

patterns with these NFRP material removal mechanisms is not currently understood. This chapter reports an experimental investigation into how the time-frequency patterns of AE signals connote the various cutting mechanisms under different cutting speeds and fiber orientations. Extensive orthogonal cutting experiments on unidirectional flax-fiber NFRP samples with various fiber orientations were conducted. The experimental setup was instrumented with a multi-sensor data acquisition system for synchronous collection of AE and vibration signals during NFRP cutting. A random forest machine learning approach was employed to quantitatively relate the AE energy over specific frequency bands to machining conditions, and hence the process microdynamics; specifically, the phenomena of fiber fracture and debonding that are peculiar to NFRP machining. Results from this experimental study suggest that the AE energy over these frequency bands can correctly predict the cutting conditions to ~95% accuracies, as well as the underlying material removal regimes.

Introduction

Natural fiber reinforced plastic (NFRP) composites have recently received considerable interest in the industry [120-123]. Their high degree of biodegradability and recyclability offers tremendous economic and ecological advantages for sustainable manufacturing. Machining of NFRPs is an essential operation for finishing industrial products from such composite materials. In fact, the viability of fiber reinforced plastics for various industrial applications is largely determined by the machined surface quality [124]. The texture and the finish of the machined surfaces of fiber reinforced composites

have a fundamental bearing on the mechanical properties (strength and hardness) and the geometric tolerance [125, 126].

While significant investigations of the mechanics of material removal in fiber reinforced composites have been reported, relatively fewer attempts have been made to characterize the machining of NFRP composites [127]. The machining process for fiber-reinforced composites involves complicated material removal mechanisms [128] that include a combination of shear deformation of the matrix material, fractures across the natural fibers, fiber pull-out, fiber-matrix detachment through tensile fracture, shearing and sliding along the fiber orientation directions, and delamination of fiber bundles [128-130]. Earlier investigations suggest that the cutting mechanisms may highly depend on fiber orientation angle and matrix properties [131]. Machining of NFRP is further complicated by the multi-scale nature of the fibers themselves [121], as well as the prevalence of significant thermal effects [120].

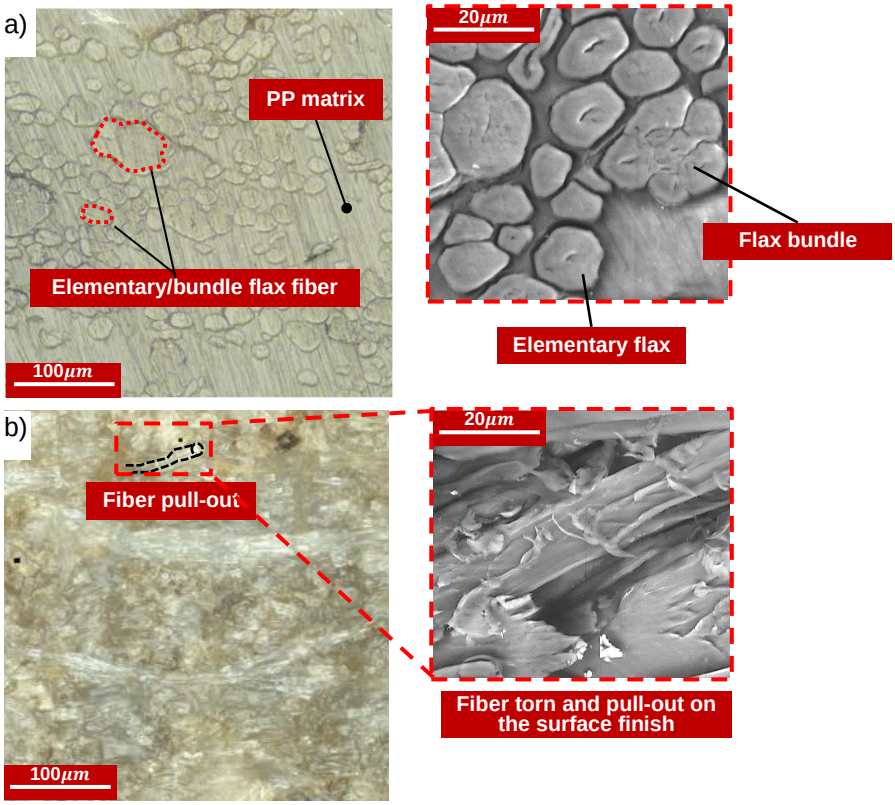

Figure V-1. a) Surface obtained from polishing a flax fiber reinforced plastic material showing a clear contour of flax fibers and basin PP matrix (with a magnified SEM image for showing the elementary/bundle fiber); b) Surface finished using orthogonal cutting processes in which the torn/broken-off fibers are randomly oriented on the surface finish (with the SEM image showing detailed torn fibers on the finished surface). (reprinted with permission)

For example, Figure V-1 shows the machined surface of an NFRP composite with a rough texture resulting from the presence of fiber protrusions spread over the surface even when the machining process was well-controlled. These protrusions result whenever the natural fibers are cut and/or pulled out across and along their lay direction. As most natural fibers are highly flexible and heterogeneous over multiple geometric scales (e.g., the material composition and mechanical properties vary greatly from macro- to micro- to nano-scales [121]), the defects on machined surfaces affect the integrity of the finished

surface, and consequently reduce mechanical properties and geometric and dimensional tolerances, hence impeding the emerging industrial applications of NFRP composites.

Currently, investigations into the machining of NFRP composites rely heavily on offline approaches that employ mechanical property testing and alternative imaging and microscopy instruments to characterize the strength, thermo-mechanics, surface morphology, and chip formation [132]. While these methods have shed significant light on the various modes of material removal and surface modification [133, 134], they cannot fully capture the effects of the enormous statistical heterogeneity and variations in the distributions of the fibers over multiple scales of the matrix on the material removal mechanisms. Additionally, these offline characterization tools are often unwieldy for real-time monitoring of the NFRP machining processes, and a sensor-based in-process monitoring approach is desirable to observe and delineate the diverse material removal mechanisms prevalent during NFRP cutting, to characterize the cutting process in real time, and to provide real-time predictions of the machined surface quality for timely intervention for quality assurance [131, 135, 136].

Conventional sensor technologies may have a limited signal-to-noise ratio (SNR) and are often insensitive to the subtle variations in cutting processes at high precision levels, where the cutting dimensions are of the order of a few μm and cutting force values are smaller than those in conventional machining processes [137]. Acoustic emission (AE), which emanates from the deformation, fracture, and/or friction mechanisms at the various tool, workpiece, and chip interfaces of machining, can be sensitive to monitoring and enable us to discern among the various material removal mechanisms in NFRP machining.

AE can also provide information related to chip entanglement, crack formation and propagation, and chip breakage in this process [138, 139]. As detailed in the next section, very little, if any, work has been done to study AE monitoring of the NFRP machining process.

Background

Earlier applications of AE for characterizing traditional glass and carbon fiber reinforced polymer composites employed approaches developed in the non-destructive testing literature for measuring and localizing the damage [140-142]. For machining applications, however, environmental noise/inference needs to be maintained at a level that ensures an adequate signal-to-noise (SNR) ratio. Many of the underlying dynamics of machining processes are complicated, and the signals are often contaminated with a high level of environmental noise. Consequently, how to analyze the nature of the nonstationary AE signals during NFRP machining remains a major challenge.

Initial investigations of AE in machining have focused mostly on relating various statistical quantifiers of the signal patterns to predicting machining conditions [143, 144]. One of the earlier research thrusts was based on applying advanced machine learning approaches to estimate the machining process state using extracted frequency features of AE signals. Kamarthi *et al.* [145] and Pittner *et al*. [146, 147] presented a neural network that extracted features using the wavelet decomposition on a multi-sensor setup for detecting tool wear. The microdynamics of the AE signal have also been investigated by Bukkapatnam *et al*. [148], and a recurrent neural network (RNN) framework that uses the fractal properties of the attractor of the underlying dynamic system along with other

machining parameters as the training inputs was developed to predict flank wear in machining. Furthermore, Rao *et al*. [149] applied a recurrent predictor neural network (RPNN) to capture the complex nonlinear and nonstationary evolution of the process underlying the measured vibration and AE signals and detect the incipient surface deterioration in ultra-precision machining processes. Cheng *et al*.[8] applied the Gaussian process with extracted statistical features as well as features based on nonlinear recurrent analysis for on-line prediction of the surface morphology. Some statistical analysis approaches [144, 150] have been presented to analyze the AE for monitoring of the cutting tool condition and to relate the AE signal features to the metal cutting process parameters. Lee *et al*. [137] discussed the unique requirements for monitoring precision manufacturing processes and the suitability of AE as a monitoring technique at the precision scale. A statistical modeling approach from our earlier effort [6] was aimed at handling transient behaviors during ultra-precision machining processes. However, most of these approaches may rely heavily on data-driven modeling and consequently lack explanations for the physical principles connecting the acoustic emission signal to the process microdynamics. Chang and Bukkapatnam [151, 152] addressed the connection between AE sensor signal waveforms and the microdynamics for machining ductile metals. The model that represents the propagation of AE waveform signals from the plastic deformation in the shear zone suggests that AE energy is highly related to the shear strain and the shear strain rate.

Investigations into the characteristics of AE waveforms from NFRP composite machining, especially those attempting to understand the relationships connecting the measured AE signals and the NRFP machining microdynamics, have received very little

attention. This lack of attention is mostly due to the difficulties of characterizing the complicated material removal mechanisms that govern NFRP composite machining. Some research efforts have also investigated the spectral characteristics AE during the machining processes of polymer-matrix composite materials [153, 154]. These investigations suggest that the AE frequency components are highly related to flank wear and workpiece surface modifications.

The present work investigates the AE characteristics related to the machining processes of NFRP composites using a data-driven analytic approach which not only allows real-time sensing and detection of the variations in the microstructure of NFRPs during machining processes, but also provides analytic insights towards explaining the deformation mechanism during machining of such NFRP materials. An experimental study is presented to relate AE signals from NFRP machining to the process conditions and the underlying material removal mechanisms. The experiments were conducted on an orthogonal cutting testbed equipped with a multi-sensor data acquisition system. To connect the AE signal patterns to the machining mechanisms of NFRP cutting, we employ a random forest machine learning model. This model aims to capture the underlying nonlinear relationship between predictors from AE signals and the estimate of the process condition without sustaining significant overfitting issues. The model was also employed subsequently to enable us to the spectral components of AE signals that are highly sensitive to various material removal mechanisms during the cutting of NFRPs. The remainder of this chapter is organized as follows: the experimental setup as well as the framework of the present approach is presented in Sec.3; Sec. 4 presents the results of the random forest

modeling study and provides insights into the physical origins of the signal components; Section 5 concludes this chapter.

Experimental and Analysis Approach

Experimental Setup and Procedures

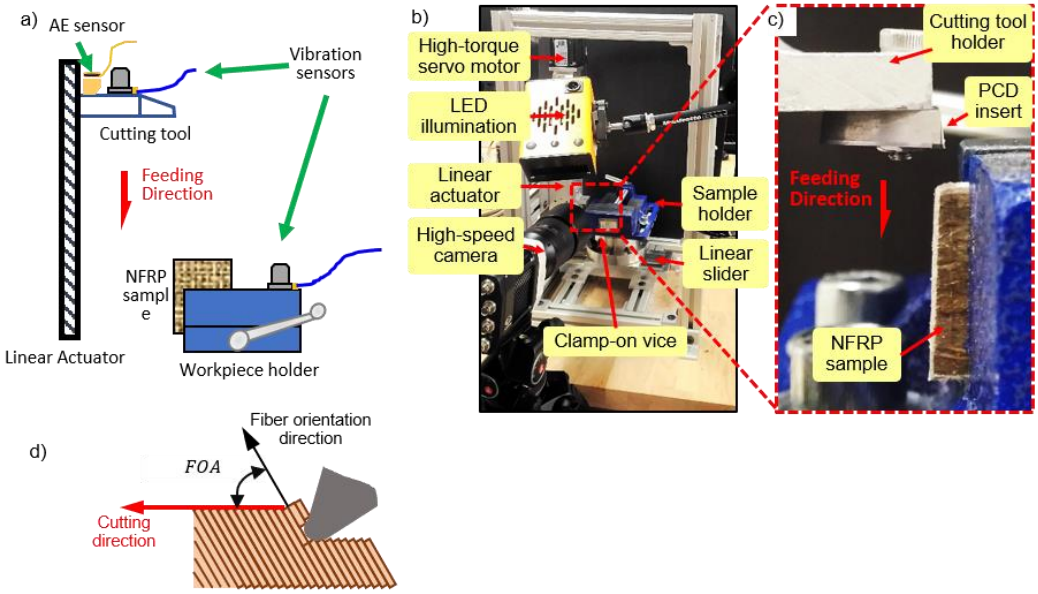

Figure V-2. Experimental setup for the orthogonal cutting process: a) schematic diagram showing the mounting locations of AE and vibration sensors, b) the orthogonal cutting machine setup with the installed high-speed camera and illumination system, c) a PCD inserted cutting tool is held against the unidirectional flax fiber/PP matrix sample before the cutting begins, and d) a schematic diagram showing the disposition of the cutting direction relative to the fiber orientation angle. (reprinted with permission)

The experiments were conducted on an orthogonal cutting testbed as shown in the schematic diagram in Figure V-2. The setup consists of two linear sliders and a workpiece

holder/clamping vice. The cutting tool setup was attached to one linear actuator (L70, Moog Animatics, Milpitas, CA) through a customized tool holder. A high-torque servomotor drives the linear actuator to ensure a consistent cutting speed. Mainly two types of sensors were mounted on the machine setup: two accelerometers (Kistler Type 8728A500) were mounted on the tool holder and the workpiece holder separately for gathering vibration signals while an acoustic emission sensor (Physical Acoustics S9225) was mounted on the cutting tool holder for collecting acoustic emission signals during the orthogonal cutting processes. This sensor monitoring system was equipped with a data acquisition system (National Instrument compactDAQ with DAQ module NI-9223) that allows real-time data collection at a 1MHz sampling rate for each sensor signal. Unidirectional flax-fiber-reinforced polypropylene composites (UDF/PP) mounted on the clamp-on vice were used as workpiece samples to investigate the effect of the fiber orientation angle on the cutting process. The UDF/PP samples shown in Figure V-2 c) are manufactured by the material supplier *Composites Evolution – UK*. Each UDF/PP workpiece is a rectangular slab with dimensions of 20×15×4 mm^3. The fiber volume fraction is 40% and the fiber unidirectionality is maintained by polyester weft fiber with low volume fraction (around 5%). The orthogonal cutting experiments were conducted with the depth of cut around 100 μm in different cutting conditions with varying cutting speeds (v=2, 4, 6, 8, 10, 12 m/min) and different fiber orientation angles ($FOA = 0°$, $45°$ and $90°$) relative to the cutting direction (shown in Figure V-2 d). Polycrystalline diamond (PCD) cutting tool inserts (Sandvik Coromant- Model TCMW16T304FLP-CD10) with a tungsten carbide substrate (as shown in Figure V-2 c)) were employed for the experiments.

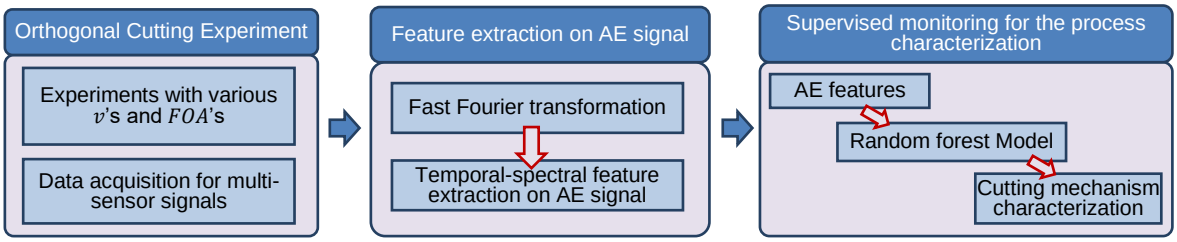

Figure V-3. A schematic diagram of the presented research approach. (reprinted with permission)

As noted earlier, the purpose of this study is to assess the ability of AE signals to discern the various process conditions including changes in the cutting speed and orientation in real-time. The ability to discern changes in the process parameters is essential (but not sufficient) for a sensor to be qualified for real-time monitoring applications. This ability is also important in NFRP machining because of the high levels of variation expected in the fiber orientation related to the cutting direction as well as in the speeds during the machining of complex geometries and profiles. Consistent with this notion, the present approach aims to estimate process conditions based on analyzing the spectral characteristics of AE signals gathered from orthogonal cutting experiments using a random forest model, as summarized in Figure V-3. We employed a total of 18 different experimental settings, each formed by a combination of six cutting speeds, $v = 2, 4, 6, 8, 10, 12$ m/min, and three FOAs, $0°$, $45°$ and $90°$. Experiments were replicated three times at each combination. At the beginning of each experiment, the surface of each NFRPs sample was polished using sand paper with a grit size of ~15μm to ensure a consistent initial condition (i.e., smooth surface with minimal deformed protrusions). As the surface was machined, the data acquisition system recorded signals from three

channels, *viz.*, two from the vibration sensors and one from an AE sensor, at a sampling rate of 1 MHz. A moving windowed time-frequency analysis was performed to extract frequency features over the specified 125 µsec long time windows. To investigate the relationship between the frequency responses of the AE signal and the fundamental cutting mechanisms during the cutting of the NFRPs, we treated the generated time-frequency features as inputs to a random forest model for characterizing the cutting processes with different fiber microstructures. Given the spectral features extracted from the online data during the machining, the trained random forest model was expected to predict the machining conditions, specifically the cutting speed and the FOA in real-time. The details of this approach are presented in the following subsections.

Time-frequency analysis and feature extraction

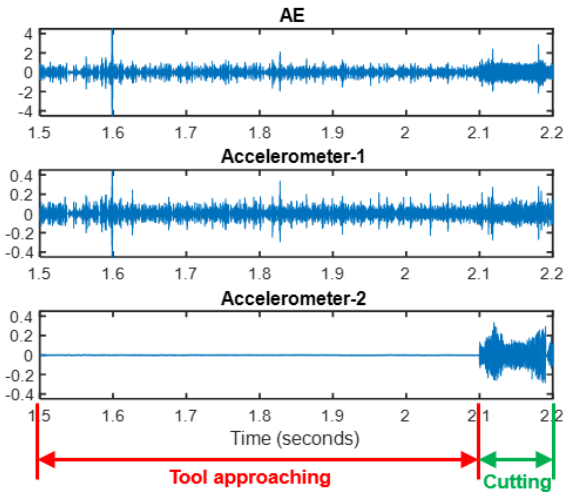

Figure V-4. Time portraits showing the synchronously gathered AE signal along with vibration signals from the tool holder (Accelerometer 1) and the workpiece holder (Accelerometer 2), respectively, during an orthogonal cutting process experiment ($v = 8$ m/min, FOA as 45°). (reprinted with permission)

Figure V-4 shows the representative sensor signals collected synchronously from the AE sensor and the two accelerometers mounted on the tool holder and the workpiece holder, respectively, during one cutting phase. The tool-approach and the cutting phases are appropriately marked. As the cutting begins, we observe a sudden increase in the amplitude of Accelerometer 2 (attached to the workpiece holder). This increase allows us to isolate the dynamics of the cutting and the non-cutting stages, such as tool-approaching and various cutting phases, by the distinct changes in the variance of the vibration signal at the onset of cutting.

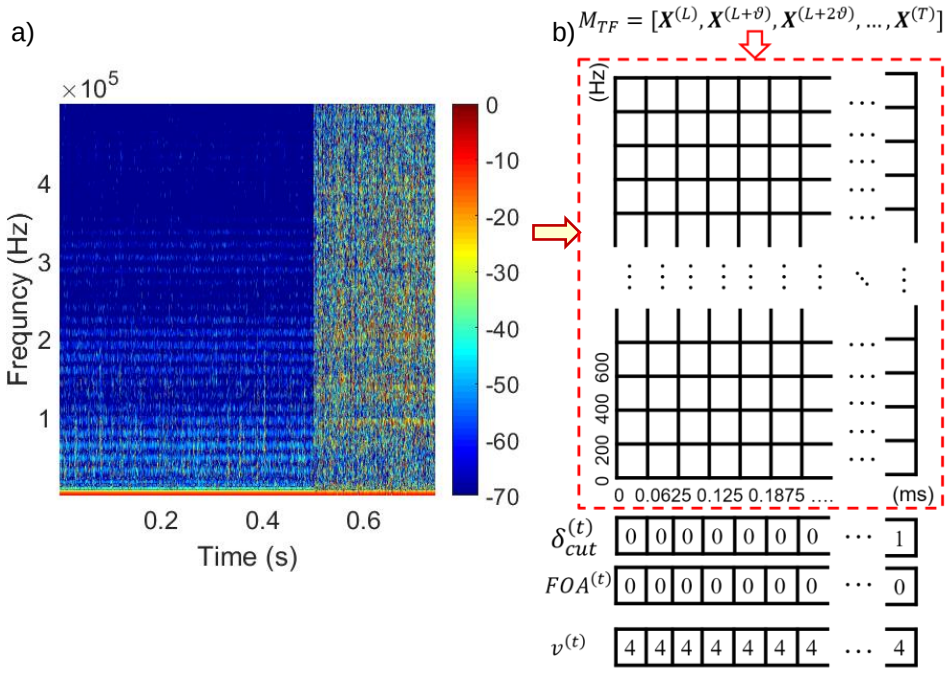

Figure V-5. A schematic diagram showing the temporal-spectral feature extraction with time stamp resolution of 0.125 *ms*, a 0.6725 *ms* overlap, and the frequency resolution as 200Hz. The process responses $\boldsymbol{Y^{(t)}} = \left[\boldsymbol{\delta_{cut}^{(t)}}, \boldsymbol{FOA^{(t)}}, \boldsymbol{v^{(t)}}\right]^{\mathsf{T}}$ where $\boldsymbol{FOA} = \boldsymbol{0^{\circ}}$ and $\boldsymbol{v = 4\, m/min}$. Note that the matrix $\boldsymbol{M_{TF}}$ records the magnitudes of the Fourier components (as Volts) and their logarithmic amplitudes (in decibels) are depicted in the spectrogram to visually signify the frequency components' variations. (reprinted with permission)

The AE signal captures the transients, i.e., time-varying frequency patterns associated with the material deformation and/or fractures that occur at irregular intervals during machining [155]. Hence, a time-frequency analysis is needed to generate the spectral features of the transient AE signal. Such temporal-spectral features are visually represented using a spectrogram as shown in Figure V-5 a), where the x axis represents the time index and the y axis is the frequency range. The energy of various frequency bands is represented using a color map. Such a spectrogram records the frequency components of the signal and their variations over time. The procedures for generating the temporal-spectral features can be summarized as follows:

1. A sliding window with window width $L = 125$ is applied to collect a set of AE signals at time index t, i.e., $\{x_{t-L+1}, x_{t-L+2}, \dots, x_t\}$.
2. Then the fast Fourier transformation (FFT) is applied to compute the frequency component:

$$\boldsymbol{X_k^{(t)}} = \sum_{\boldsymbol{n=t-L+1}}^{\boldsymbol{t}} \boldsymbol{x_n e^{-\frac{i2\pi kn}{L}}} \qquad k = 0,1, \dots, L-1 \tag{1}$$

where $\{x_n\}$ (for $n = t - L + 1, t - L + 2, \dots, t$) is the time series of the AE signal within sliding window L, and the fast Fourier transformation generates the frequency components $\boldsymbol{X^{(t)}} = \left[X_1^{(t)}, X_2^{(t)}, \dots, X_L^{(t)}\right]^\top$. After sequentially generating the frequency component vectors, $\boldsymbol{X^{(t)}}$'s (for $t = L, L+1, L+2, \dots, T$), the matrix of the spectrogram can be represented as $M_{TF} = [\boldsymbol{X^{(L)}}, \boldsymbol{X^{(L+\vartheta)}}, \boldsymbol{X^{(L+2\vartheta)}}, \dots, \boldsymbol{X^{(T)}}]$, where ϑ denotes the step of the sliding window. Essentially, the spectral energy over the high frequency components of AE waveforms, is related to the underlying microdynamics of the machining processes.

The statistical analysis based on a Gini index [156], as presented in the sequel, suggests that these energy values can serve as important features to discern between various pairs of cutting conditions.

Apart from the spectral energy distribution via the time-frequency analysis, we had considered a few advanced signal analysis approaches, such as wavelet decomposition [157], Hilbert-Huang transformation (HHT)/ empirical mode decomposition (EMD) and intrinsic time-scale decomposition (ITD). However, these methods have specific drawbacks in terms of being able to capture the energies across various bands. For example, as for wavelet decomposition, it has low resolution on high frequency components, especially those that capture the variations in the process microdynamics. A wavelet packet representation could provide fine resolution within specific frequency ranges [158]. However, most of the wavelet packet bases (especially, if the orthogonality condition is imposed) have an infinite support at time and/or frequency domain (i.e., every coefficient is estimated by taking all the samples of the AE signals). This complicates the extraction of the energies over various bands. For the HHT/EMD as well as ITD [159], it is not straightforward to extract frequency components from the intrinsic mode functions (IMFs). These representations introduce severe edge effects when decomposing the AE signals over multiple levels of IMFs, which amounts to losing the data points in the time domain.

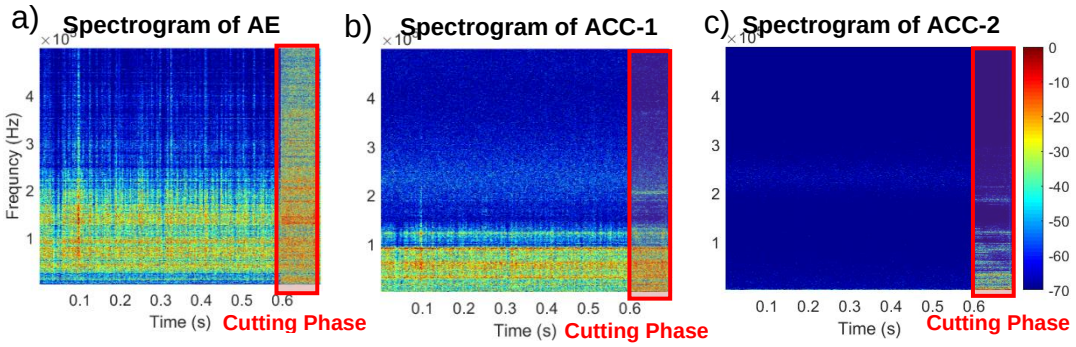

Figure V-6. The representative time-frequency domain spectrograms (in dB) gathered during an orthogonal cutting experiment ($v = 8$ m/min, FOA as 45°): a) the AE sensor, b) the Accelerometer-1, and c) the Accelerometer-2. Here, the rectangular (red) frame at the right side of every plot indicates the temporal-spectral information during the cutting phase. (reprinted with permission)

Figure V-6 a), b) and c) show the spectrograms of the AE and the two vibration signals, respectively, capturing the temporal-spectral features of the tool-approaching and the cutting phases. The spectrograms as shown in Figure V-5 were generated by the FFT with a sliding window of 0.125 ms and a 50% time step (i.e., $\vartheta = 0.5L$), which translates to a temporal resolution of 0.125 ms (x-axis), and we select 200 Hz as the spectral resolution (y-axis). Our choice of the window length and the overlap is based on the following rationale. AE sensor signals are composed of multiple AE pulses released from various events, such as fracture and dislocation avalanche that occur at frequency ranges of over 200kHz [i.e., these events last just for a fraction of a microsecond a up to a few microseconds (see Figure V-10)]. We selected a 0.125 ms long time window, which is of sufficient length to achieve the frequency resolution to discern the changes in the spectral shape, and at the same time, not too long to ignore the time variations of AE events (i.e., the transients). Similarly, a 50% was chosen to extract sufficient number of features and at the same time avoiding significant correlation (more specifically, multiple collinearity)

among the features to train the random forest model. Taken together, the window length and the overlap allow us to effectively extract the salient time and frequency characteristics of the measured AE signals. The edge effect due to the sliding window may be ignored as the window size (0.125 ms duration) is smaller than the durations of the overall recordings (which normally last for seconds) by 4~5 orders of magnitude. The dimensions of the temporal-spectral features are illustrated in Figure V-5. The energy of each element in the spectrogram matrix is represented in a color map, ranging from -70 dB (blue-colored) to 0 dB (red-colored). The sensitivity of the AE sensor can be validated by the high-frequency response of the AE signal [Figure V-6 a)] as compared to the vibration signals shown in Figure V-6 b) and c). In fact, only the spectrogram of the AE signals showed remarkable/noticeable differences in the high frequency ranges (> 100kHz).

Note that the multi-sensor setup allows a partition of the time-frequency features into cutting vs. non-cutting. Let τ_1 and τ_2 be the start and the end time stamps of the segment for the cutting phase [e.g., the start and the end points of the red frame shown in Figure V-6 a)]. Here we denote the cutting phase partition using a series of indicators $\left\{\delta_{cut}^{(t)}\right\} = \{\delta_{cut}^{(L)}, \delta_{cut}^{(L+\vartheta)}, \delta_{cut}^{(L+2\vartheta)}, \dots, \delta_{cut}^{(T)}\}$, where $\delta_{cut}^{(t)} = 1$ for $t \in [\tau_1, \tau_2]$ and $\delta_{cut}^{(t)} = 0$ otherwise. The response vector $\boldsymbol{Y}$ combines the cutting indicator with other control parameters for the experiments, i.e., $\boldsymbol{Y}^{(t)} = \left[\delta_{cut}^{(t)}, FOA^{(t)}, v^{(t)}\right]^{\top}$ for $t = L, L+\vartheta, L+2\vartheta \dots, T$, where T is the total length of the acquired data, $FOA \in \{0°, 45°, 90°\}$ and cutting speed $v \in \{2,4,6,8,10,12\}$ (units in m/min). Given the time duration T_0 (in seconds) of the recording, here $T = T_0 \times Fs$, where Fs is the sampling rate ($Fs = 1$MHz

for all experiment recordings). Then, the extracted features, $\boldsymbol{X}$'s, as well as the process responses, $\boldsymbol{Y}$'s, for a single recording Ω can be represented in the following format:

$$\boldsymbol{\Omega} = \left[\boldsymbol{X}^{(t)^{\top}}, \boldsymbol{Y}^{(t)^{\top}}\right]^{\top} = \begin{bmatrix} \boldsymbol{X}^{(L)} & \boldsymbol{X}^{(L+\vartheta)} & \boldsymbol{X}^{(L+2\vartheta)} & \dots & \boldsymbol{X}^{(T)} \\ \boldsymbol{Y}^{(L)} & \boldsymbol{Y}^{(L+2\vartheta)} & \boldsymbol{Y}^{(L+2\vartheta)} & \dots & \boldsymbol{Y}^{(T)} \end{bmatrix} \tag{2}$$

Random forest classifier for process condition monitoring

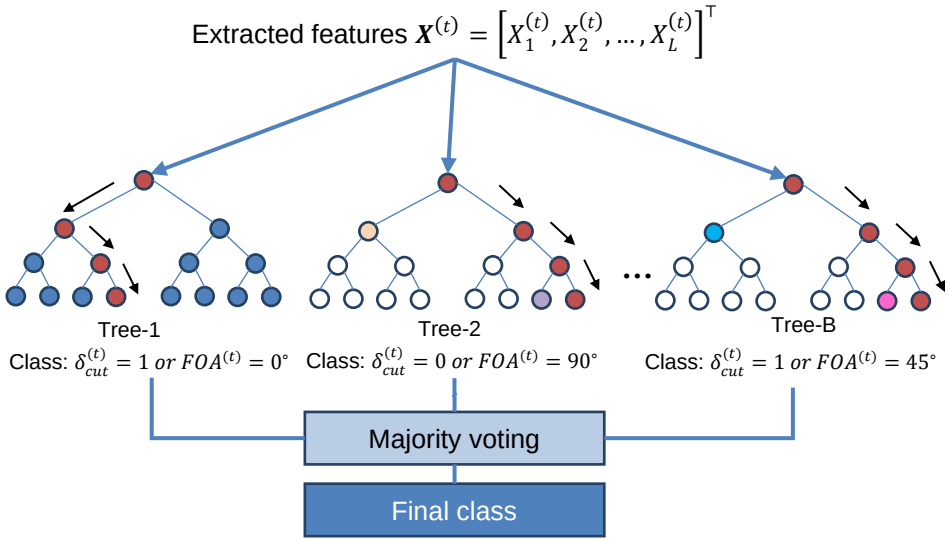

Figure V-7. The schematic diagram of the random forest machine learning approach. (reprinted with permission)

The random forest approach [160] is applied to capture the empirical relationships between the AE spectral features $\{\boldsymbol{X}^{(t)}\}$ and $\{y^{(t)}\}$, where $y^{(t)}$ is a subset of response $\{\boldsymbol{Y}^{(t)}\}$ (e.g., $y^{(t)} = \delta_{cut}^{(t)}$ for characterizing cutting vs. non-cutting phases and $y^{(t)} = FOA^{(t)}$ for classifying the fiber orientation). During the training phase, the random forest approach (in Figure V-7) employs samples obtained, with replacement, from the training set $\{\boldsymbol{X}^{(t)}\}$

and $\{y^{(t)}\}$ to build multiple tree learning models. The decision rule for each tree learning model was based on the randomly selected features $\{\boldsymbol{X}^{(t)}\}$ [161, 162]. Unlike conventional regression approaches [163], a random sampling and selection scheme allows a classification model to capture the underlying nonlinear relationships without imposing biased structures or overfitting issues. The detailed procedures on training the random forest models are stated as follows [164].

Given a training dataset $\Omega' = \left\{\left(\boldsymbol{X}^{(L)^\top}, y^{(L)^\top}\right), \left(\boldsymbol{X}^{(L+\vartheta)^\top}, y^{(L+\vartheta)^\top}\right), \dots, \left(\boldsymbol{X}^{(T)^\top}, y^{(T)^\top}\right)\right\}$ ($y^{(t)} = FOA^{(t)}$ for fiber orientation classification and $y^{(t)} = \delta_{cut}^{(t)}$ for the cutting vs. non-cutting phase), the random forest first generates B new training datasets Ω_i (for $i = 1, \dots, B$), which have the same sample size as the original Ω', with some samples replaced in the dataset (also called bootstrap sampling). Consequently, some observations may be repeated in the new dataset Ω_i.

For each bootstrapped sample, the decision tree is constructed by the following procedures: at each node of the tree model, m features are randomly sampled and the best split among these randomly selected predictors is chosen (also called a feature bagging scheme). The splitting criterion at the node is chosen to minimize the sum of the squares, which allows the partition of m predictors into M regions $R_1, R_2, \dots, R_M$. Assume that the splitting variable X_j is split at point x_j to segment the half plane as R_1 and R_2, where $R_1(j, x_j) = \{\boldsymbol{X} | X_j \leq x_j\}$ and $R_2(j, x_j) = \{\boldsymbol{X} | X_j > x_j\}$. The splitting variable X_j and the split point x_j should be the optimal solution to the following objective [164]:

$$\min_{j,x_j}\left[\min_{c_1}\sum_{X_k\in R_1(j,x_j)}(y_k-c_1)^2+\min_{c_2}\sum_{X_k\in R_2(j,x_j)}(y_k-c_2)^2\right] \quad (3)$$

where the constants c_1 and c_2 are the responses in region R_1 and R_2. Note that the overall expected output/response in each region can be formulated as $f(X)=\sum_{s=1}^{M}c_s\,I(X\in R_s)$. The optimal constant value, $\widehat{c_S}$, is the average of response $y^{(t)}$ in region R_s, i.e., $\widehat{c_S}=average\,(y^{(t)}|X^{(t)})$. Hence, the constants can be solved by $\widehat{c_1}=average\left(y^{(t)}\middle|X^{(t)}\in R_1(j,x_j)\right)$ and $\widehat{c_2}=average\left(y^{(t)}\middle|X^{(t)}\in R_2(j,x_j)\right)$. The splitting algorithm is stopped once a fully binary tree model of a certain number of levels (in the default setup, 8 levels) is built.

For our case study, the inputs of the feature space are from the extracted spectrogram $\{\boldsymbol{X}^{(t)}\}$, and the training outputs $\{y^{(t)}\}$ are selected from the responses $\{\boldsymbol{Y}^{(t)}\}$. For the parameter selection, we chose the number of trees as B =100 and 25 variables to randomly sample candidates at each decision split for all the cases tested, which results in a minimal out-of-bag (OOB) error.

The random forest generally performs an implicit feature selection by using a small subset of all variables $\{X_j\}$ for the classification problem. Such subsets are regarded as "strong variables" for superior performance in handling high-dimensional data/features. The associated Gini importance values are the measures that visualize the results from the implicit feature selection of the random forest model and are commonly used as the indicator(s) of the feature relevance to the classification results.

Let $p_{\kappa} = \frac{\mathbb{N}_{\kappa}}{\mathbb{N}}$ be the fraction of the $\mathbb{N}_{\kappa}$ samples from the class $FOA = \{0°, 45°, 90°\}$ or $\delta_{cut} = \{0,1\}$ ($\kappa \in FOA$ or δ_{cut}) of the total $\mathbb{N}$ samples at node ξ. The Gini impurity $Gini(\xi)$ is calculated as:

$$Gini(\xi) = 1 - \sum_{\kappa} p_{\kappa}^2 \tag{4}$$

The decrement $\Delta Gini$ is caused by the splitting and sending of the samples to two sub-nodes ξ_{ϖ} and ξ_{ς} (with fractions with respect to the two sub nodes $p_{\varpi} = \frac{\mathbb{N}_{\varpi}}{\mathbb{N}}$ and $p_{\varsigma} = \frac{\mathbb{N}_{\varsigma}}{\mathbb{N}}$). Threshold x_j on variable X_j is defined as

$$\Delta Gini(\xi) = Gini(\xi) - p_{\varpi} Gini(\xi_{\varpi}) - p_{\varsigma} Gini\left(\xi_{\varsigma}\right) \tag{5}$$

A search over all variables at node ξ and over all possible segmentation threshold obtains a pair $\{X_j, x_j\}$ that allows a maximal $\Delta Gini$ value. The decrease in Gini impurity is recorded for all node $\{\xi\}$'s for all trees B and accumulated for all variable X_j's as:

$$I_{Gini}\left(X_j\right) = \sum_{B} \sum_{\xi} \Delta Gini_{\{X_j\}}(\xi, B) \tag{6}$$

Intuitively, this Gini importance value I_{Gini} indicates how often a particular feature $X_k^{(t)}$ was selected for a split, and how large its overall discriminative value was for the classification problem [156].

AE based monitoring of the NFRP machining process

A random forest model to detect the start and end of the cutting process using AE signals

Given the extracted AE time-frequency features $\{\boldsymbol{X}^{(t)}\}$ and the response $\{y^{(t)}\} = \left\{\delta_{cut}^{(t)}\right\}$, a random forest model was trained to discern between the cutting and the non-cutting phases. Specifically, for both training and testing data sets 20% of the data was gathered during the cutting operation and the other 80% data during the non-cutting operation. The overall data set was split into five subgroups and each subgroup was tested with the random forest classification. Each data set selected around 1400 samples for training and about 600 samples for testing. We compared the present approach with Fisher's linear discriminant analysis (LDA). At the outset, conventional LDA approaches are effective only when the signal features gathered from every pair of process conditions (e.g., cutting vs. non-cutting, and fiber orientation angle - FOA) can be separated (in the feature space) using a linear boundary (as in a hyperplane). The LDA models also assume that the feature values from different conditions can be grouped into distinct Gaussian clusters with equal variance, and that they are well separated from each other. In contrast, a random forest can separate out the signal features from various conditions using complex nonlinear boundaries and does not make any assumptions on the clustering of the feature values. Table V-1 summarizes the classification results [in terms of overall accuracy, True Positive Rate (TPR) and True Negative Rate (TNR)] from the presented approach vs. LDA for the present case study. Here the TPR measures the proportion of actual samples that are correctly identified as from the cutting condition, TNR represents the percentage of the

samples correctly classified as from the non-cutting condition. It is evident that the average accuracy of the random forest model is ~94%, which is 20% higher than that of LDA. Additionally, the true positive rate (TPR) increases from 0.45 with LDA to 0.84 with the random forest model.

Table V-1. Cross-validation comparisons of random forest *vs.* LDA based for the study case of cutting *vs.* non-cutting. (adapted with permission)

		Accuracy	True Positive Rate (TPR)	True Negative Rate (TNR)
Random Forest	Mean	0.9427	0.8390	0.9819
	Std	0.0124	0.0455	0.0079
Fisher's LDA	Mean	0.7674	0.4443	0.8189
	Std	0.0264	0.0566	0.0340

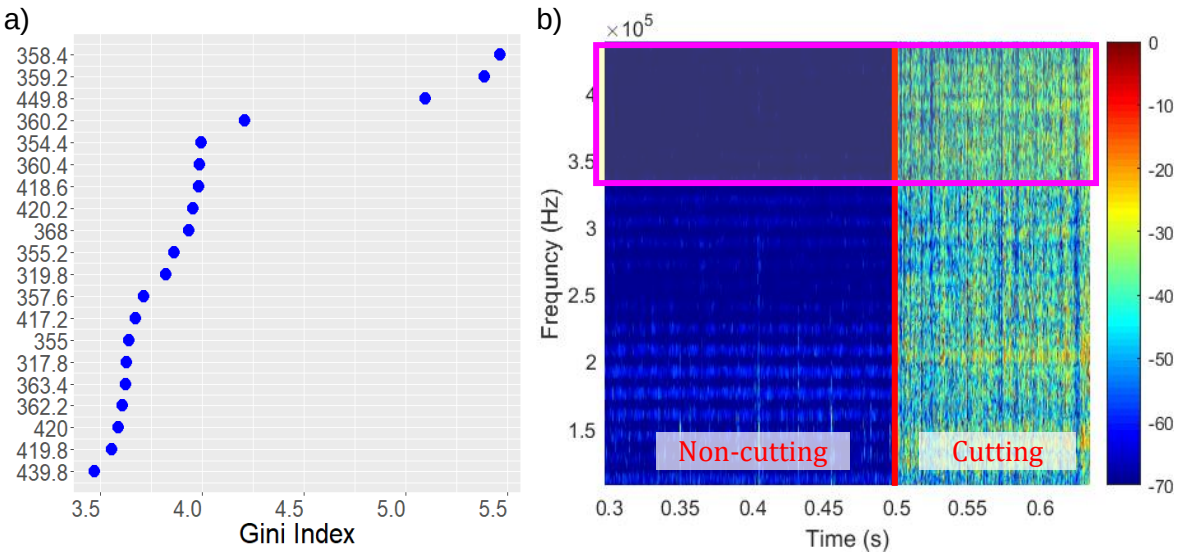

Figure V-8. Results for classifying cutting vs. non-cutting: a) the Gini importance plot with the significant features labeled (y-axis) by the frequency band (kHz) (e.g., the highest Gini value corresponds to the frequency response at 358.4kHz); b) a spectrogram representation of the non-cutting phase vs. the cutting phase (red-line segmented) with corresponding significant frequency bands highlighted in the pink frame. (reprinted with permission)

The resulting Gini importance values from the classification problem of the cutting vs. non-cutting phases are shown in Figure V-8 a). Note that each y-axis label refers to the frequency (kHz) in the temporal-spectral matrix (e.g., the first Gini index relates to the frequency response in 358.4kHz). A higher Gini importance value of a frequency range indicates a greater contribution of the spectral feature to improving the accuracy. Interestingly, the most significant frequency features determining the accuracy of the random forest based on Gini importance are in the frequency ranges of 350kHz to 440kHz. The spectrogram in Figure V-8 b) suggests that more energy is contained in such a frequency range (highlighted in the pink frame) during the cutting compared to the non-cutting phase. However, conventional vibration sensors are not suited for monitoring processes at such high frequencies, as they do not have an adequate dynamic response in this range. This high frequency response highlights the significance of using an AE sensor instead of the more commonly used vibration sensor for fast, high-frequency (> 100 kHz) detection of subtle changes during machining at microscales.

Supervisory monitoring for the fiber orientation effect

In the next case study, we investigated the effect of fiber orientation on machining microdynamics and the corresponding AE characteristics. Given the extracted time-frequency features $\{\boldsymbol{X}^{(t)}\}$ and the response $\{y^{(t)}\} = \{FOA^{(t)}\}$, a random forest model was trained to predict the fiber orientation based on the spectral features of AE. Here, spectral values above 100kHz in every column of the AE spectrogram (Figure V-9) were used as the features because the high-frequency spectral components have the time resolution needed to detect changes in their incipient states. As shown in Figure V-9, the AE time

portraits as well as the temporal spectral features show significant differences between the fiber orientation with 90 degrees and the others under the same cutting speed (4 m/min). In contrast, the signal variance between fiber orientations with 0 and 45 degrees are less noticeable in the time domain compared to the difference between their temporal-spectral features plotted in the spectrograms in Figure V-9.

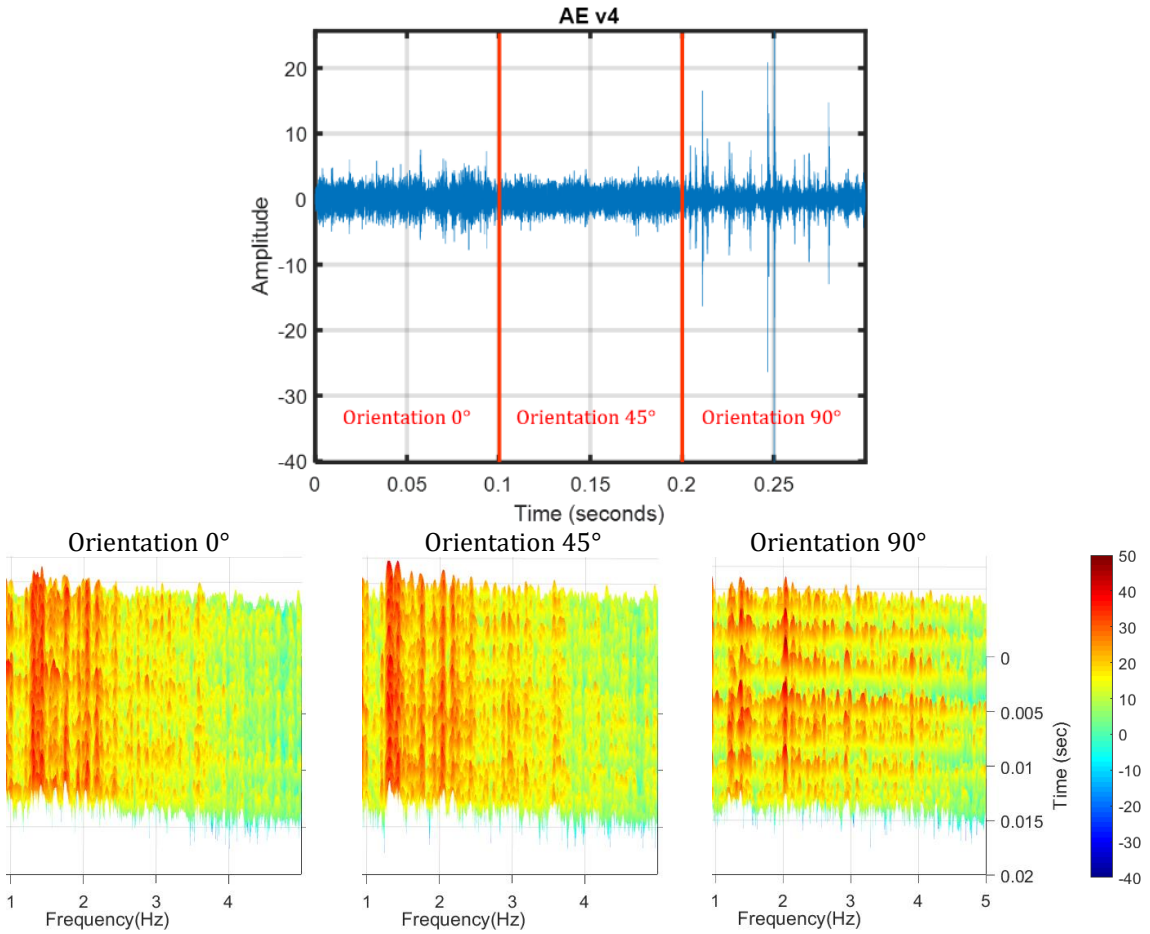

Figure V-9. The combined AE signals recorded during orthogonal cutting with different fiber orientation angles (*FOA*s) at the same cutting speed (4 m/min) and three spectrograms, one for each *FOA*. (reprinted with permission)

The results of classification accuracy are listed in Table V-2 (results are generated based on 5 computations on the combined data from different cutting speeds). Here in the confusion matrix, each row represents the actual class and the columns are the predicted results for three classes. The value inside each element $[\kappa_i, \kappa_j]$ of the confusion matrix represents the portion of samples from actual class κ_i that are identified as class κ_j ($\kappa_i, \kappa_j \in FOA = \{0^\circ, 45^\circ, 90^\circ\}$). The results suggest a statistically significant difference between study cases with 0 degrees of orientation and all others. This difference may be due to the cutting mechanisms of different fiber orientations. In the 0 degrees study case, the fibers are mostly aligned along the cutting direction. Therefore, for such an orientation, the cutting process is predominantly with the PP matrix removal, and with very few fibers sliding/shearing along interfacial areas during material removal. In contrast, the cutting mechanism in the 45- and 90-degree orientations involves more cutting and pulling of fibers. Even though the signal in the 90-degree orientation has significantly different time portraits, which exhibit strong transient behaviors, the random forest could recognize its difference compared to the other groups with around 60% accuracy. This result may indicate that other factors affecting the cutting mechanism and/or the material removal (e.g., varying cutting speeds) are not considered in the random forest model.

Table V-2. Cross-validation results for various fiber orientations using the random forest. (adapted with permission)

Confusion Matrix		Predicted		
		0°	45°	90°
Actual	0°	0.8531	0.1259	0.0210
	45°	0.1354	0.7446	0.1200
	90°	0.2047	0.1913	0.6040

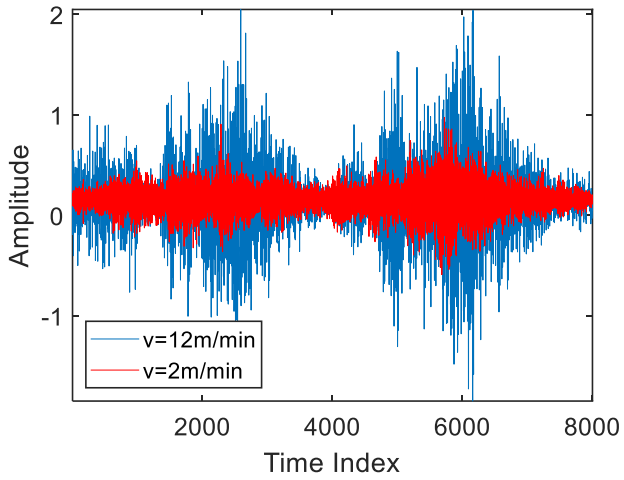

Figure V-10. Comparison of the waveforms of the AE signals between two cutting speeds: 2 m/min (red) vs. 12 m/min (blue) for $FOA = 90^{\circ}$. (adapted with permission)

Results from previous investigations [125, 165-167] into the machinability of fiber reinforced composites suggest that as the cutting speed increases, the surface integrity drops. This may be due to the viscoelastic property of the composite materials. Also, higher cutting speeds may increase the shear stress on the chip tool interface, which in turn increases the strain/elongation of the fibers nonlinearly. For all these reasons, more fiber failures may occur (fiber breakages, pull-out and some inefficient shearing causing microfiber failures of the cellulose structure), along with more plastic deformation of the matrix per unit time for higher speed cutting conditions, resulting in more energy released. The evidence can be found in the time portraits of the AE signals (see Figure V-10), which were recorded during two experiments with the same FOA but different cutting speeds. Here the blue lines refer to the AE signal gathered under machining parameters $v = 12m/min$ and $FOA = 90^{\circ}$, and the red-lined AE signal is from the experiment with $v =$

$2m/min$ and $FOA = 90°$. It may be noticed that even under the same fiber orientation angle, a higher cutting speed (12m/min) may result in a larger AE envelope. That is, when analyzing the cutting mechanisms with respect to different fiber orientations, the cutting speed also needs to be considered. Clearly, the increase in the AE amplitude due to an increase in the cutting speed may be attributed to the increase in the material shear rates, and hence the sources of AE increase with an increase in the cutting speed.

Table V-3. Accuracy of *FOA* classification for various fiber orientations under each cutting speed (*m/min*) (in comparisons with LDA). (adapted with permission)

Random Forest	$v = 2$	$v = 4$	$v = 6$	$v = 8$	$v = 10$	$v = 12$
0 vs 45	0.9719	0.9583	0.9313	0.9396	1.0000	0.9031
0 vs 90	0.9594	0.9656	0.9563	0.9492	0.9281	0.8750
45 vs 90	0.9938	0.9792	0.9478	0.9271	0.9667	0.9031

LDA	$v = 2$	$v = 4$	$v = 6$	$v = 8$	$v = 10$	$v = 12$
0 vs 45	0.7188	0.7125	0.6281	0.5688	0.7625	0.6219
0 vs 90	0.6469	0.7031	0.7656	0.6680	0.5688	0.5844
45 vs 90	0.6813	0.6901	0.5344	0.5625	0.6563	0.6875

The performance of the random forest model (in terms of classification accuracy) for identifying the correct FOA using AE signals collected at six different cutting speeds was compared with that of LDA (see Table V-3). Three cases of different FOAs (0° vs. 90°, 0° vs. 45°, and 45° vs. 90°) were investigated under each cutting speed. Compared with LDA, the random forest's accuracy for discerning fiber orientations increased by ~30% (from 65% to 94.8%). As noted earlier, such an improvement is a consequence of the random forest relaxing the strong assumption LDA makes on how features are clustered and distributed. Pertinently, the random forest employs an ensemble of decision trees, such

that each tree is trained using a different, random subset of the features at each split of the tree model. This avoids the correlation between selected features. Also, the random forest provides metrics that help with feature selection as well as interpretation of the classification results. Specifically, it generates the quantifiers, such as Gini Index, to statistically indicate the extent to which every feature contributes to the classification accuracy.

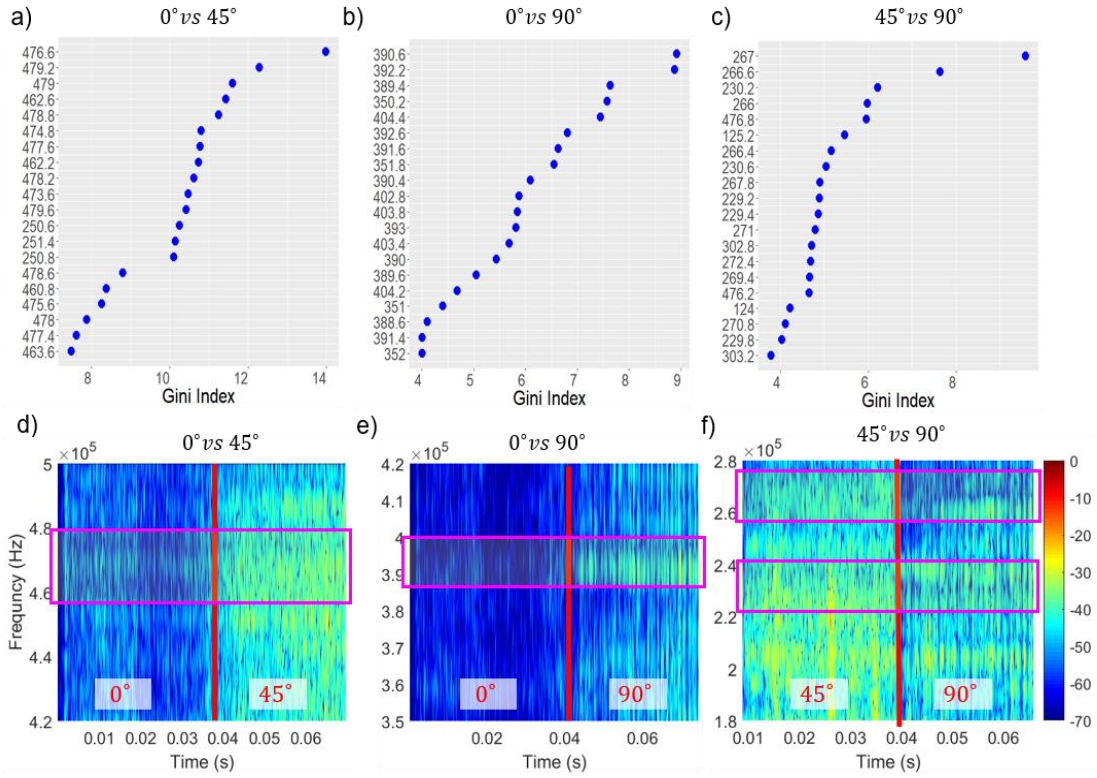

Figure V-11. GINI indices of the significant frequency components for three *FOA* classifiers: a) $0°vs.45°$, b) $0°vs.90°$, and c) $45°vs.90°$. The spectrograms of the juxtaposed AE signals show the differences in the frequency contents among these three cases, d) $0°vs\,45°$, e) $0°vs\,90°$, and f) $45°vs\,90°$). The most significant frequency features are highlighted by pink-colored frames. (reprinted with permission)

The Gini index values for three cases are listed in the Figure V-11 a), b) and c); Figure V-11 d) to f) depict the comparisons of the spectrograms corresponding to these three cases ($0^{\circ} vs. 45^{\circ}$, $0^{\circ} vs. 90^{\circ}$, and $45^{\circ} vs. 90^{\circ}$), where the vertical red line in each figure segments two orientation conditions. Note that here the pink blocks highlight the most significant frequency features (with highest Gini index values) suggested by the results from the random forest classification. Early work[168, 169] suggests that AE signals with a frequency response above 350kHz during failure tests of fiber reinforced composites are more related to fiber breakage. Our case clearly shows that the most significant spectral features that distinguish 0° from 45° and 90° are above 350kHz. This finding can be verified, as in the power spectrums of both Figure V-11 d) and e), more energy in high frequencies (above 350kHz) is observed for $FOAs = 45^{\circ}$ and 90° compared to $FOA = 0^{\circ}$. When we compare the cutting processes for 45° vs. 90°, the differences in the frequency components are less discernible, but the random forest model is able to select significant frequency features [frequency bands 260kHz~ 280Hz and 220~240kHz, as highlighted in Figure V-11 f)] to recognize different fiber orientations (45° vs. 90°) for cutting NFRPs. Such different features in certain high frequency bands suggest that the different responses of the AE sensor may be related to different types of failure modes/cutting mechanisms.

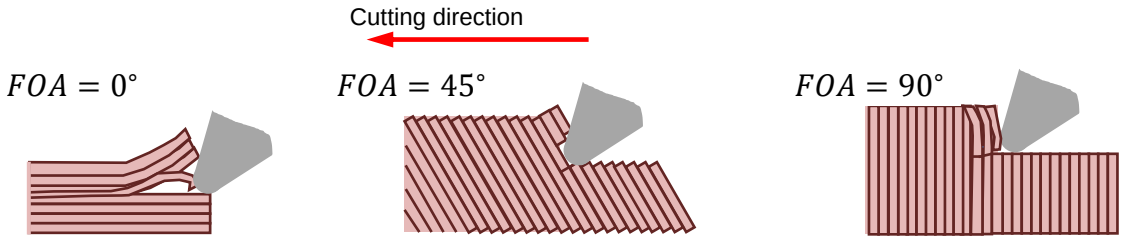

Figure V-12. A schematic diagram showing the cutting mechanisms under different fiber orientation angles (FOAs) [170]. (reprinted with permission)

Unlike the brittle failure mechanisms that occur when cutting synthetic fiber (e.g., carbon and glass fiber) reinforced composites with the thermoset polymer matrix, the NFRP sample with the thermoplastic polymer matrix possesses high flexibility and follows ductile deformation behavior when undergoing transverse shear stress during orthogonal cutting [128]. For $FOA = 0°$, the cutting process is dominated by the matrix deformation under the shearing zone with some amount of debonding of the fibers along the cutting direction (matrix-fiber shearing) with a few episodes of fiber pull-out and microfiber failures (see Figure V-12). At $FOA = 45°$ and $90°$, however, micro-failures across the fiber axis are prevalent, due to the shearing and tensile forces. Also, for the process under $FOA = 45°$, the interfacial shearing along the fiber orientation causes debonding between the fiber and the PP matrix. Moreover, intermittent fracture is one mechanism under $FOA = 90°$ that results in fiber tensile failure and/or pull-out towards the cutting direction with a sudden increase in cutting force.

Figure V-13 shows the schematic diagrams of the chip formation of NFRPs under different FOA's. It may be noticed that because of the different orientation of fibers, the microstructure (elementary/bundle fibers and matrix-fiber bounds) may undergo anisotropic stress/strain, resulting in the distinct failure modes of the NFRP components during the material removal process. Consequently, the internal failures of the composites may manifest as different modes (e.g., fiber breakage and fiber-matrix debonding). The fracture energy released from such different failure modes may contribute to the generated AE waveform. The following fracture energy analysis of the cutting processes for NFRPs provides a theoretical explanation of the differences in the released fracture energy due to different microstructure variations and cutting speeds under each fiber orientation condition.

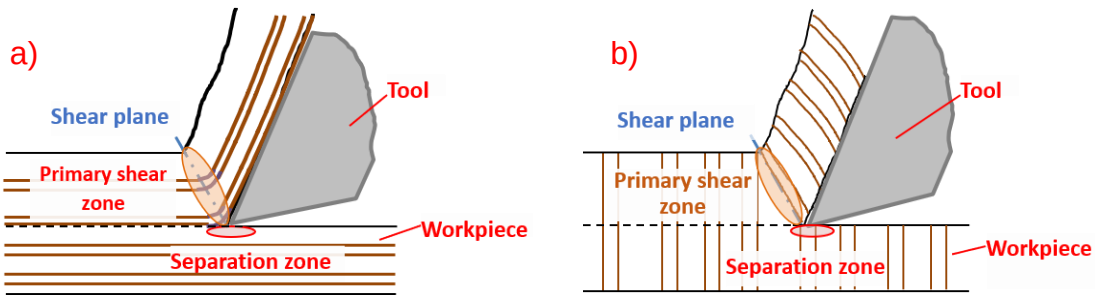

Figure V-13. The schematic diagrams showing the cutting modes and chip formation for different fiber orientations (FOAs): a) 0° and b) 90°. (reprinted with permission)

As for the orthogonal cutting processes only for thermoplastic composites such as the PP-matrix in the tested NFRP samples, the power released during the shear stress can be formulated as:

$$E_S = \frac{F_S \cdot V_S}{b \cdot t_u \cdot V} = \frac{F_S}{b \cdot t_u} \cdot \frac{cos\alpha}{\cos(\phi - \alpha)} \quad (7)$$

where V_S is the shearing speed, V is the cutting speed, b is the chip width, t_u is the uncut chip thickness (100 μm) and α is the rake angle. The shear angle, ϕ, is a function of the rake angle, α, and the friction angle, β, i.e., $\phi = \frac{\pi}{4} - \frac{1}{2}(\beta - \alpha)$. Then the shear force, F_S, around the shearing zone can be formulated as [165]:

$$F_s = A_s \cdot \tau = \frac{t_u b}{\sin(\phi)} \cdot \tau \quad (8)$$

Here τ refers to the shear strength of the matrix. Overall, the energy from the deformation of the thermoplastic composite is $E_S = \frac{cos\alpha}{\cos(\phi - \alpha) \cdot sin\phi} \cdot \tau$.

For different fiber orientation angles (FOAs), the cutting mechanism may vary, and in turn the total energy for each FOA may differ. In addition to the energy released from the plastic deformation of the PP matrix due to the combined shear and tensile forces, the following components may contribute to the fracture energy under different FOAs.

For the cutting condition when $FOA = 0°$, the cutting mechanism is related mainly to matrix deforming and very little fiber-matrix debonding and/or interfacial shearing of fibers. The matrix shear debonding energy is denoted by W_S , with the propagating failure at distance L, given by[171]:

$$W_S = 2\pi r_0 \tau_0 L/\gamma \quad (9)$$

Here r_0 is the fiber radius, τ_0 is the maximum boundary shear stress at the fracture and the stress concentration coefficient $\gamma = \left(\frac{2G}{E}\right)^{\frac{1}{2}} / r_0 \cdot \ln\left(\frac{r_1}{r_0}\right)$, where $r_1 - r_0$ is the matrix thickness, G is the matrix shear modulus and E is the elastic modulus of the fiber.

Based on a square packing geometry assumption, the fracture energy per unit area A of such a condition can be rewritten as [171]:

$$\frac{W^{(0)}}{A} = \frac{W_S^{(0)}}{A} = \tau_0 \left(\frac{E}{2G}\right)^{\frac{1}{2}} L_b f_1(V) f_2(V) \tag{10}$$

In contrast, for $FOA = 90°$ [shown in Figure V-13 b)], the flax fibers in the workpiece undergo stresses along the fiber matrix boundaries in the primary shear zone. Hence, the energy released during orthogonal cutting consists of 1) the matrix material deformation in the shear zone, 2) fiber failure (breakage and pull-out from the matrix), 3) interfacial friction between fiber matrix bonds, 4) chip motion and material entanglement on the rake face, and 5) the interaction between clearance face of the tool and the machined surface. In the following section we only consider the AE energy released from the sources 1-3. This is because these are considered as the primary sources of AE during NFRP machining, and they can be physically related to the underlying microdynamics, especially the material removal mechanisms prevailing under different fiber orientations.

The summation of the friction energy [171] between the fiber and the matrix boundary with a constant friction force, $\tau_f = \frac{f}{\pi d} dx$, between the fibers and the boundary of the matrix in the effective region/length of l is:

$$P_f = \pi d \tau_f l \tag{11}$$

When a debonded fiber separates off over length $l = L_f$ inside the matrix, the friction work, W_f, between the fiber and the matrix can be formulated as:

$$W_f = -\int_{l=L_f}^{l=0} 2\pi r_0 \tau_f dl = \pi r_0 \tau_f L_f^2 \tag{12}$$

The fracture energy for the fiber breakage/ pull-out is [171]:

$$W_D = \frac{\pi r_o^2}{2E}\int_{l=0}^{l=L_D}\left(\sigma - \frac{2\tau_f l}{r}\right)^2 dl \tag{13}$$

By substituting $L = r_0\sigma/2\tau_f$, we have

$$W_D = \frac{\pi r_o^2 \sigma^2 L}{6E} \tag{14}$$

Considering the cutting speed and the square packing geometry assumption, in addition to the energy released from the matrix deformation, the fracture energy under $FOA = 90^\circ$ contains the following: 1) the energy released from fiber tensile failure per unit area A, $\frac{W_D}{A} = \frac{\sigma_0^2}{12E} L_b f_2(V)$, and 2) the energy released from friction per unit area A, $\frac{W_f}{A} = \frac{\tau_f L_f}{2r_0} f_2(V)$. Here, the maximum debonding length $L_b = r_0$ and the volume fraction functions are $f_1(V) = \ln\left(\frac{r_1}{r_0}\right) = \left\{\ln\left[\left(\frac{\pi}{V}\right)^{\frac{1}{2}} - 1\right]\right\}^{\frac{1}{2}}$, $f_2(V) = V$, and $f_3(V) = \left(\frac{V}{\pi}\right)^{\frac{1}{2}}$ [172]. The maximum debonding length is $L_b = \frac{r_0}{\tau_f}[\frac{\sigma_b}{2} - \tau_0\left(\frac{E}{2G}\right)^{\frac{1}{2}} f_1(V)]$ and we assume that $L_f \approx L_b$. Hence, as the cutting speed, v, increases, more area, A, is machined per unit time ($A = b \cdot v$, where b is the width of the chip and is approximately equivalent to the width of the sample for all experiments). Consequently, more fracture energy is released at higher

cutting speeds, resulting in significantly different AE envelopes under different cutting speeds as suggested in Figure V-10.

Table V-4. Physical properties of the NFRPs materials. (adapted with permission)

List of physical properties	
Fiber radius r_0	~10μm
Fiber tensile strength σ_0	~500 MPa[173, 174]
PP matrix tensile strength	~29.5 MPa [174, 175]
Maximal shear stress debonding	~2 MPa[176]
Fiber Young Modulus E	~50 GPa [174]
PP matrix Young Modulus E	~1 GPa
Constant frictional stress τ_f	7~40 MPa
Possible range of shearing stress	30 MPa [177][58]
Fiber volume fracture V	0.4
Fiber packing	Square (4 nearest neighborhoods)
Volume fraction functions	$f_1(V) \approx 0.7676$, $f_2(V) = 0.4$ and $f_3(V) = 0.3568$

Relative to connecting the AE responses to various failure modes, earlier efforts [142, 168, 178] included extensive mechanical tests on the composite materials and applied frequency analysis to the resulting acoustic emission signals for different types of failures. A summary of the frequency responses of AE signals to different failure mechanisms of fiber reinforced composites is listed in Table V-5. Matching significant frequency features (results from random forest classifications with the highest Gini coefficients) with the AE characteristics (frequency responses) for different failures modes allows us to identify the

different failure modes related to the prevalent cutting mechanisms under distinct fiber orientations.

Table V-5. Dominant range of frequency response (kHz) to fracture energy [178-180].

Failure mode	Frequency response (kHz)
Matrix failure	90~180
Fiber-matrix debonding	240~310
Fiber breakage	>350

As shown in Figure V-11 a), b) and d), the AE frequency responses ranging from 350kHz to 440kHz distinguish $FOA = 0^{\circ}$ from the other angles. That is, compared to the fiber debonding (which has an AE frequency response in the range from 240kHz to 310kHz) which is prevalent under orthogonal cutting with 0° FOA, the frequency responses related to fiber breakage (350kHz to 440kHz) are more significant for both $FOA = 45^{\circ}$ and 90°. When we compare the results of $FOA = 45^{\circ}$ vs. 90°, even though the differences in frequency components are less noticeable as seen in Figure V-11 f), the random forest approach is capable of picking up most significant frequency features (within frequency ranges of 260kHz~ 280Hz and 220~240kHz) to achieve a classification accuracy around 95.3%. Table V-5 suggests that these frequency features determining the classification accuracy for $FOA = 45^{\circ}$ vs. 90° are related to fiber-matrix debonding and fiber pull-out [142], which are the fundamental cutting mechanisms that distinguish the machining processes between $FOA = 45^{\circ}$ and 90° [170]. As for the 45° orientation

position, the cutting mechanism consists of compression induced interfacial shearing along the fiber orientation direction that causes fiber-matrix debonding; for $FOA = 90^{\circ}$, the fractures that contribute predominantly to fiber pull-out emerge intermittently (this may be one reason that the AE waveform under 90 degrees shows a significant transient pattern compared to the others). Moreover, fiber breakage is prevalent for both $FOA = 45^{\circ}$ and 90° cases. This prevalence may be one reason that the AE frequency responses (350kHz to 440kHz) to the fiber breakage are less significant in discerning the changes between cutting mechanisms under $FOA = 45^{\circ}$ and 90° conditions.

Conclusions

This chapter presented the framework of an in-process monitoring scheme for machining processes of NFRP materials. Using a random forest model, we showed that the AE signals contain relevant information pertaining to the process. The main contributions of this chapter are as follows.

- An in-process monitoring scheme with a multiple-sensor setup for gathering the vibrations as well as the acoustic emission information during orthogonal cutting of the NFRP has been discussed. Different machining conditions and material removal routes were analyzed using the AE signals, namely, a) cutting vs. no cutting, and b) cutting with different fiber orientations;
- A random forest algorithm was applied for supervised monitoring of the processes with accuracy around 95% to distinguish various fiber orientations towards the cutting direction that are related to distinct cutting mechanisms. Results from the

random forest approach indicate that the high frequency information from the captured acoustic emission signals reflects fundamental cutting mechanism changes;

- Further analysis shows that the most significant frequency responses determining the accuracy of the random forest model are highly related to the distinct failure modes under various fiber orientation conditions. Hence, the presented approach connects the AE characteristics to the microdynamics of machining NFRPs.

We note that the AE features considered in the present work aggregates multiple mechanisms prevalent during the machining of NFRP composites. Process conditions, especially the cutting speed determines the material deformation rate. Since AE is released from the various material deformation and fracture mechanisms during NFRP machining, the time and frequency characteristics of the AE waveform varies with the cutting speed. The cutting speed also affects the dynamics of fiber deformation and fracture, matrix failure as well as the actions at the primary and the secondary and tertiary deformation zones. Particularly, this variation in the AE waveform characteristics in the 50-100 kHz band (as noted by the Gini index) can be used to identify the process condition, including the cutting speed and FOA. The AE waveforms, as gathered, is a composition of elementary AE pulses released from the various different sources. Towards using the results of these predictions for process control, it would be desirable to isolate the contributions of individual source in the measured AE signal. Also, for future work, other factors, such as the effect of fiber (bundle) distributions and chip formations, need to be considered for further AE analysis. Further advances in the analytical approach is needed

for identifying how the various transient components from specific sources are composed in the measured AE signals to diagnose incipient anomalies during the machining of NFRPs. We also note that the present approach can be applied for predicting process conditions during machining of different types of composite materials. Further experimental studies within machining of alternative composites materials (e.g., synthetic fiber-reinforced plastics or bio-composites) are needed to identify the chief material removal and surface modification mechanism, characterize the resulting AE waveforms, as well as to develop practical methods to monitor in machining process performance and surface quality in real-time.

References

[6] Wang, Z., and Bukkapatnam, S. T., 2018, "A Dirichlet process Gaussian state machine model for change detection in transient processes", Technometrics, **60**(3), pp: 373--385. https://doi.org/10.1080/00401706.2017.1371079.

[8] Cheng, C., Wang, Z., Hung, W., Bukkapatnam, S. T., and Komanduri, R., 2015, "Ultra-precision machining process dynamics and surface quality monitoring", Procedia Manufacturing, **1**, pp: 607-618.

[120] Chegdani, F., Takabi, B., Tai, B. L., El Mansori, M., and Bukkapatnam, S. T., 2018, "Thermal Effects on Tribological Behavior in Machining Natural Fiber Composites", Procedia Manufacturing, **26**, pp: 305-316.

[121] Chegdani, F., Wang, Z., El Mansori, M., and Bukkapatnam, S. T., 2018, "Multiscale tribo-mechanical analysis of natural fiber composites for manufacturing applications", Tribology International, **122**, pp: 143-150.

[122] Holbery, J., and Houston, D., 2006, "Natural-fiber-reinforced polymer composites in automotive applications", Jom, **58**(11), pp: 80-86.

[123] Al-Oqla, F. M., and Sapuan, S., 2014, "Natural fiber reinforced polymer composites in industrial applications: feasibility of date palm fibers for sustainable automotive industry", Journal of Cleaner Production, **66**, pp: 347-354.

[124] Ramulu, M., 1997, "Machining and surface integrity of fibre-reinforced plastic composites", Sadhana, **22**(3), pp: 449-472.

[125] Herrera-Franco, P., and Valadez-Gonzalez, A., 2005, "A study of the mechanical properties of short natural-fiber reinforced composites", Composites Part B: Engineering, **36**(8), pp: 597-608.

[126] Ku, H., Wang, H., Pattarachaiyakoop, N., and Trada, M., 2011, "A review on the tensile properties of natural fiber reinforced polymer composites", Composites Part B: Engineering, **42**(4), pp: 856-873. https://doi.org/10.1016/j.compositesb.2011.01.010.

[127] Nassar, M. M., Arunachalam, R., and Alzebdeh, K. I., 2017, "Machinability of natural fiber reinforced composites: a review", Int J Adv Manuf Technol, **88**(9-12), pp: 2985-3004.

[128] Chegdani, F., and El Mansori, M., 2018, "Mechanics of material removal when cutting natural fiber reinforced thermoplastic composites", Polymer Testing, **67**, pp: 275-283.

[129] De Rosa, I. M., Santulli, C., and Sarasini, F., 2009, "Acoustic emission for monitoring the mechanical behaviour of natural fibre composites: A literature review", Composites Part A: Applied Science and Manufacturing, **40**(9), pp: 1456-1469. https://doi.org/10.1016/j.compositesa.2009.04.030.

[130] Herrera-Franco, P., and Valadez-Gonzalez, A., 2004, "Mechanical properties of continuous natural fibre-reinforced polymer composites", Composites Part A: applied science and manufacturing, **35**(3), pp: 339-345.

[131] Romhány, G., Karger ‐ Kocsis, J., and Czigány, T., 2003, "Tensile fracture and failure behavior of thermoplastic starch with unidirectional and cross ‐ ply flax fiber reinforcements", Macromolecular Materials and Engineering, **288**(9), pp: 699-707.

[132] Babu, G. D., Babu, K. S., and Gowd, B. U. M., 2013, "Effect of machining parameters on milled natural fiber-reinforced plastic composites", J. Adv. Mech. Eng, **1**, pp: 1-12.

[133] George, J., Sreekala, M., and Thomas, S., 2001, "A review on interface modification and characterization of natural fiber reinforced plastic composites", Polymer Engineering & Science, **41**(9), pp: 1471-1485.

[134] Valadez-Gonzalez, A., Cervantes-Uc, J. M., Olayo, R., and Herrera-Franco, P. J., 1999, "Effect of fiber surface treatment on the fiber–matrix bond strength of natural fiber reinforced composites", Composites Part B: Engineering, **30**(3), pp: 309-320. https://doi.org/10.1016/S1359-8368(98)00054-7.

[135] Teti, R., Jemielniak, K., O'Donnell, G., and Dornfeld, D., 2010, "Advanced monitoring of machining operations", CIRP Annals-Manufacturing Technology, **59**(2), pp: 717-739.

[136] Chegdani, F., Mezghani, S., El Mansori, M., and Mkaddem, A., 2015, "Fiber type effect on tribological behavior when cutting natural fiber reinforced plastics", Wear, **332**, pp: 772-779.

[137] Lee, D.-E., Hwang, I., Valente, C. M., Oliveira, J., and Dornfeld, D. A., 2006, "Precision manufacturing process monitoring with acoustic emission", International Journal of Machine Tools and Manufacture, **46**(2), pp: 176-188.

[138] Uehara, K., and Kanda, Y., 1984, "Identification of chip formation mechanism through acoustic emission measurements", CIRP Annals-Manufacturing Technology, **33**(1), pp: 71-74.

[139] Bhuiyan, M. S. H., Choudhury, I. A., and Nukman, Y., 2012, "An innovative approach to monitor the chip formation effect on tool state using acoustic emission in turning", International Journal of Machine Tools and Manufacture, **58**, pp: 19-28. https://doi.org/10.1016/j.ijmachtools.2012.02.001.

[140] Margueres, P., Meraghni, F., and Benzeggagh, M., 2000, "Comparison of stiffness measurements and damage investigation techniques for a fatigued and post-impact fatigued GFRP composite obtained by RTM process", Composites Part A: Applied Science and Manufacturing, **31**(2), pp: 151-163.

[141] Davidovitz, M., Mittelman, A., Roman, I., and Marom, G., 1984, "Failure modes and fracture mechanisms in flexure of Kevlar-epoxy composites", J Mater Sci, **19**(2), pp: 377-384.

[142] Mizutani, Y., Nagashima, K., Takemoto, M., and Ono, K., 2000, "Fracture mechanism characterization of cross-ply carbon-fiber composites using acoustic emission analysis", Ndt & E International, **33**(2), pp: 101-110.

[143] Dornfeld, D., and Kannatey-Asibu, E., 1980, "Acoustic emission during orthogonal metal cutting", International Journal of Mechanical Sciences, **22**(5), pp: 285-296.

[144] Kannatey-Asibu, E., and Dornfeld, D. A., 1981, "Quantitative relationships for acoustic emission from orthogonal metal cutting", Journal of Engineering for Industry, **103**(3), pp: 330-340.

[145] Kamarthi, S. V., Kumara, S. R., and Cohen, P. H., 1995, "Wavelet representation of acoustic emission in turning process", Proc. of The 1995 Artificial Neural Networks in Engineering (ANNIE'95),St. Louis, Missouri, USA, ASME, pp: 861-866.

[146] Pittner, S., Kamarthi, S. V., and Gao, Q., 1998, "Wavelet networks for sensor signal classification in flank wear assessment", Journal of Intelligent Manufacturing, **9**(4), pp: 315-322.

[147] Pittner, S., and Kamarthi, S. V., 1999, "Feature extraction from wavelet coefficients for pattern recognition tasks", IEEE Transactions on pattern analysis and machine intelligence, **21**(1), pp: 83-88.

[148] Bukkapatnam, S. T., Kumara, S. R., and Lakhtakia, A., 2000, "Fractal estimation of flank wear in turning", Journal of dynamic systems, measurement, and control, **122**(1), pp: 89-94.

[149] Rao, P., Bukkapatnam, S., Beyca, O., Kong, Z. J., and Komanduri, R., 2014, "Real-time identification of incipient surface morphology variations in ultraprecision machining process", Journal of Manufacturing Science and Engineering, **136**(2), pp: 021008.

[150] Kannatey-Asibu Jr, E., and Dornfeld, D., 1982, "A study of tool wear using statistical analysis of metal-cutting acoustic emission", Wear, **76**(2), pp: 247-261.

[151] Chang, D.-C., and Bukkapatnam, S., 2004, "Towards characterizing the microdynamics of AE generation in machining", Machining science and technology, **8**(2), pp: 235-261.

[152] Bukkapatnam, S., and Chang, D.-C., 2005, "A statistical mechanistic model of acoustic emission generation in shear zone of machining", Transactions of NAMRI/SME, **33**, pp: 597-604.

[153] Arul, S., Vijayaraghavan, L., and Malhotra, S., 2007, "Online monitoring of acoustic emission for quality control in drilling of polymeric composites", Journal of materials processing technology, **185**(1-3), pp: 184-190.

[154] Velayudham, A., Krishnamurthy, R., and Soundarapandian, T., 2005, "Acoustic emission based drill condition monitoring during drilling of glass/phenolic polymeric composite using wavelet packet transform", Materials Science and Engineering: A, **412**(1), pp: 141-145. https://doi.org/10.1016/j.msea.2005.08.036.

[155] Hase, A., Wada, M., Koga, T., and Mishina, H., 2014, "The relationship between acoustic emission signals and cutting phenomena in turning process", Int J Adv Manuf Technol, **70**(5-8), pp: 947-955.

[156] Menze, B. H., Kelm, B. M., Masuch, R., Himmelreich, U., Bachert, P., Petrich, W., and Hamprecht, F. A., 2009, "A comparison of random forest and its Gini importance with standard chemometric methods for the feature selection and classification of spectral data", BMC bioinformatics, **10**(1), pp: 213.

[157] Bukkapatnam, S. T., Kumara, S. R., and Lakhtakia, A., 1999, "Local eigenfunctions based suboptimal wavelet packet representation of contaminated chaotic signals", IMA Journal of Applied Mathematics, **63**(2), pp: 149-162.

[158] Bukkapatnam, S. T., Kumara, S., and Lakhtakia, A., 1999, "Analysis of acoustic emission signals in machining", Journal of manufacturing science and engineering, **121**(4), pp: 568-576.

[159] Iquebal, A. S., Bukkapatnam, S. T. S., and Srinivasa, A., 2017, "Change detection in complex dynamical systems using intrinsic phase and amplitude synchronization", arXiv preprint arXiv:1701.00610.

[160] Liaw, A., and Wiener, M., 2002, "Classification and regression by randomForest", R news, **2**(3), pp: 18-22.

[161] Botcha, B., Rajagopal, V., Babu N, R., and Bukkapatnam, S. T. S., 2018, "Process-machine interactions and a multi-sensor fusion approach to predict surface roughness in cylindrical plunge grinding process", Procedia Manufacturing, **26**, pp: 700-711. https://doi.org/10.1016/j.promfg.2018.07.080.

[162] Arumugam, J., Bukkapatnam, S. T., Narayanan, K. R., and Srinivasa, A. R., 2016, "Random forests are able to identify differences in clotting dynamics from kinetic models of thrombin generation", PloS one, **11**(5), pp: e0153776.

[163] Afrin, K., Illangovan, G., Srivatsa, S. S., and Bukkapatnam, S. T., 2018, "Balanced Random Survival Forests for Extremely Unbalanced, Right Censored Data", arXiv preprint arXiv:1803.09177.

[164] Wu, D., Jennings, C., Terpenny, J., Gao, R. X., and Kumara, S., 2017, "A comparative study on machine learning algorithms for smart manufacturing: tool wear prediction using random forests", Journal of Manufacturing Science and Engineering, **139**(7), pp: 071018.

[165] Wambua, P., Ivens, J., and Verpoest, I., 2003, "Natural fibres: can they replace glass in fibre reinforced plastics?", composites science and technology, **63**(9), pp: 1259-1264.

[166] Mahdi, M., and Zhang, L., 2001, "A finite element model for the orthogonal cutting of fiber-reinforced composite materials", Journal of materials processing technology, **113**(1-3), pp: 373-377.

[167] Eriksen, E., 1999, "Influence from production parameters on the surface roughness of a machined short fibre reinforced thermoplastic", International Journal of Machine Tools and Manufacture, **39**(10), pp: 1611-1618. https://doi.org/10.1016/S0890-6955(99)00017-6.

[168] Nazmdar Shahri, M., Yousefi, J., Fotouhi, M., and Ahmadi Najfabadi, M., 2016, "Damage evaluation of composite materials using acoustic emission features and Hilbert transform", Journal of Composite Materials, **50**(14), pp: 1897-1907.

[169] Park, J.-M., Son, T. Q., Jung, J.-G., and Hwang, B.-S., 2006, "Interfacial evaluation of single Ramie and Kenaf fiber/epoxy resin composites using micromechanical test and nondestructive acoustic emission", Composite Interfaces, **13**(2-3), pp: 105-129.

[170] Ramulu, M., Kim, D., and Choi, G., 2003, "Frequency analysis and characterization in orthogonal cutting of glass fiber reinforced composites", Composites Part A: Applied Science and Manufacturing, **34**(10), pp: 949-962.

[171] Kaelble, D., 1973, "Theory and Analysis of Fracture Energy in Fiber Reinforced Composites", The Journal of Adhesion, **5**(3), pp: 245-264.

[172] Wells, J., and Beaumont, P., 1985, "Debonding and pull-out processes in fibrous composites", J Mater Sci, **20**(4), pp: 1275-1284.

[173] Alves Fidelis, M. E., Pereira, T. V. C., Gomes, O. d. F. M., de Andrade Silva, F., and Toledo Filho, R. D., 2013, "The effect of fiber morphology on the tensile strength of natural

fibers", Journal of Materials Research and Technology, **2**(2), pp: 149-157. https://doi.org/10.1016/j.jmrt.2013.02.003.

[174] Chegdani, F., Mezghani, S., and El Mansori, M., 2015, "Experimental study of coated tools effects in dry cutting of natural fiber reinforced plastics", Surface and Coatings Technology, **284**, pp: 264-272.

[175] Shubhra, Q. T., Alam, A., and Quaiyyum, M., 2013, "Mechanical properties of polypropylene composites: A review", Journal of thermoplastic composite materials, **26**(3), pp: 362-391.

[176] Khalil, H. P. S. A., Ismail, H., Rozman, H. D., and Ahmad, M. N., 2001, "The effect of acetylation on interfacial shear strength between plant fibres and various matrices", European Polymer Journal, **37**(5), pp: 1037-1045. https://doi.org/10.1016/S0014-3057(00)00199-3.

[177] Hsueh, C.-H., 1990, "Interfacial debonding and fiber pull-out stresses of fiber-reinforced composites", Materials Science and Engineering: A, **123**(1), pp: 1-11. https://doi.org/10.1016/0921-5093(90)90203-F.

[178] Nimdum, P., and Renard, J., 2012, "Use of acoustic emission to discriminate damage modes in carbon fibre reinforced epoxy laminate during tensile and buckling loading", Proc. of 15th European Conference on Composite Materials (ECCM 15),Venice, Italy, p. 8p.

[179] De Groot, P. J., Wijnen, P. A. M., and Janssen, R. B. F., 1995, "Real-time frequency determination of acoustic emission for different fracture mechanisms in carbon/epoxy

composites", Composites Science and Technology, **55**(4), pp: 405-412. https://doi.org/10.1016/0266-3538(95)00121-2.

[180] Park, J.-M., Kim, P.-G., Jang, J.-H., Wang, Z., Hwang, B.-S., and DeVries, K. L., 2008, "Interfacial evaluation and durability of modified Jute fibers/polypropylene (PP) composites using micromechanical test and acoustic emission", Composites Part B: Engineering, **39**(6), pp: 1042-1061. https://doi.org/10.1016/j.compositesb.2007.11.004.

CHAPTER VI

BIDIRECTIONAL GATED RECURRENT NEURAL NETWORKS (GRNNS) BASED SMART ACOUSTIC EMISSION (AE) SENSING OF NATURAL FIBER REINFORCED PLASTIC (NFRP) COMPOSITE MACHINING PROCESS

Preface

This chapter investigates an in-process monitoring approach using Acoustic Emission (AE)—elastic waves sourced from various plastic deformation and fracture mechanisms—to characterize the variations in the NFRP machining process. Existing analytic tools are incapable of handling the transient dynamic patterns in AE signals, and how process conditions and the underlying material removal mechanisms affect these patterns. To address this gap, two types of the bidirectional gated recurrent neural network (BD-GRNN) models are developed to predict the process conditions based on dynamic AE patterns. The AE signals gathered from orthogonal cutting experiments on NFRPs samples performed at 6 different cutting speeds and 3 fiber orientations are used for testing the performance of the models. The results from the experimental study suggest that BD-GRNNs can correctly predict (around 87% accuracy) the cutting conditions based on the extracted temporal-spectral features of AE signals.

Introduction

Natural Fiber Reinforced Polymer (NFRP) composites are becoming increasingly attractive for various industrial applications for industries such as automotive, construction and aerospace [181] as NFRPs offer an attractive balance between cost, carbon footprint and performance. Most of the emerging industrial applications necessitate machining of these NFRP composite panels to dimensional tolerances of $\pm$1mm and surface roughness

within 1 μm. Currently, machining process is crucial for realizing NFRPs' functionality as the machined surface quality is highly related to the bearing of mechanical property of the NFRP products. However, NFRPs possess complex material characteristics, such as viscoelastic behaviors and thermal effect [182]. Especially, their complex multi-scale structure poses significant challenges for machining. Due to the natural fibers' cellulose structure and their orientations in the composites, these randomly distributed elementary/bundle fibers within the matrix basis introduce distinct material removal mechanisms, create surface conformity issues and consequently influence the overall machinability of such a material for industrial applications.

Researchers have been investigating smart sensing approaches for real-time monitoring and anomaly diagnosis[137]. For NFRP machining, such a real-time sensing approach may facilitate the machining process characterization, the evaluation of machined surface quality, and timely intervention for in-process quality assurance. Among various sensor candidates, acoustic emission (AE) sensor shows potentials for in-process monitoring of the cutting processes at precision level (depth of cut within tens of micrometers). The AE waves gathered during the machining process are sourced from the (elasto-)plastic deformation, fracture and friction at interfaces between cutting tool, workpiece and chip of machining processes [143, 183, 184]. Besides, AE waveforms are also related to the crack formation and chip breakage and/or entanglement during the material removal process. However, such elastic transient waves during machining processes may be highly interfered by the environmental noises, and consequently they are

with low signal-to-noise ratio (SNR). The challenge stays as to how to analyze such nonstationary signals with strong transient behaviors.

Two representative time portraits of the AE's transient patterns are listed in the Figure VI-1 a) shows a continuous AE signal with low energy and long decaying time, while Figure VI-1 b) depicts a burst patterned AE waveform which oftentimes contains higher frequency responses with sharp rising and decaying times[185]. During a NFRP cutting process, fast streamed AE data may exhibit both types of behaviors, continuous waveforms combined with (irregular) intermittent bursts. Each of the waveform patterns may be due to the energy released from a distinct material removal mechanism. Hence, the prominent thrusts towards analyzing the AE waveforms may be related to how to connect the short-time dependent waveform patterns (intermittent bursts and resultant time-varying frequency responses) with different cutting conditions that result in changes of the fundamental cutting mechanisms.

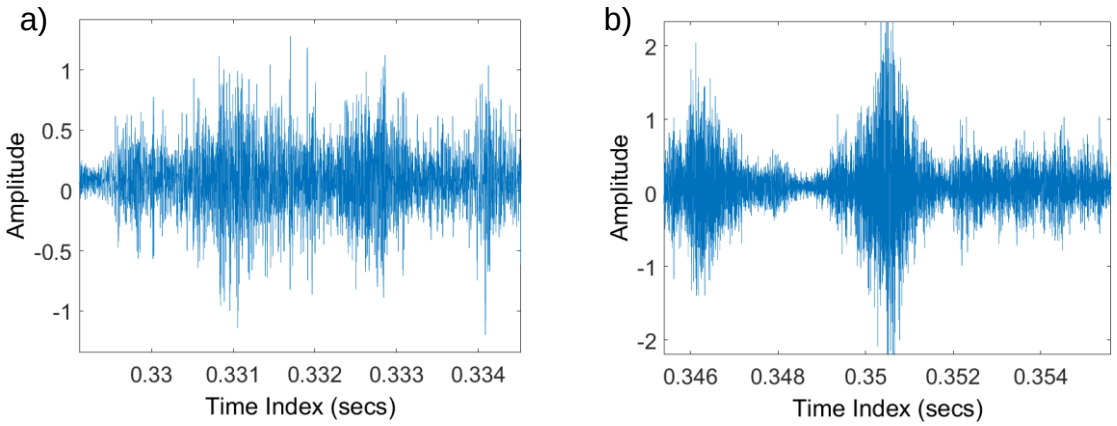

Figure VI-1. The representative AE waveforms showing a) AE bursts and b) stationary emission [185].

From the perspective of the dynamic system, this transient behavior is referred to as dynamic intermittency [5]. The transitions between intermittent bursts and laminar phases from such a system create nonstationarity with time-variant dependency. Thus far, analyzing the intermittent AE signals is still challenging. In this chapter, we present a sensor-based monitoring approach for smart sensing and AE characterizations for machining NFRPs. To address this gap, we investigate the Gated Recurrent Neural Network (GRNN) models to relate the AE waveform features to different process conditions and the underlying material removal mechanisms of machining NFRPs. During the orthogonal cutting experiments, AE signals were gathered from the testbed equipped with multi-sensor data acquisition system. To connect the AE signal patterns to the machining mechanisms of NFRPs cutting, we employ GRNN models for characterizing the temporal-spectral features of AE signals. The rest of this chapter is organized as follows: the framework of the presented approach is introduced in Sec. 2. The experiment details about orthogonal cutting experimental setup, implementation of GRNN models and the results for AE characterizations are presented in Sec. 3. Sec. 4 provides concluding remarks.

Recurrent Deep Learning Approaches

This section shows the framework of Gated Recurrent Neural Network (GRNN) for characterizations of AE signals for NFRP cutting. Figure VI-2 summarizes the schematic diagram for implementing GRNNs. First, sensor signals were recorded with various cutting conditions [varying cutting speeds (v) and fiber orientation angles (FOA)]. The temporal-spectral features were extracted using a sliding-windowed time-frequency

analysis over specified micron-seconds long time windows. To handle the time-varying frequency response of the AE signal and relate it to different machining conditions during NFRPs cutting, the temporal-spectral features are directly treated as the input series in the GRNN for characterizing the cutting processes. Hence, it avoids ad-hoc feature selection. The GRNNs were then developed for characterizing the time-spectral features of AE waveforms.

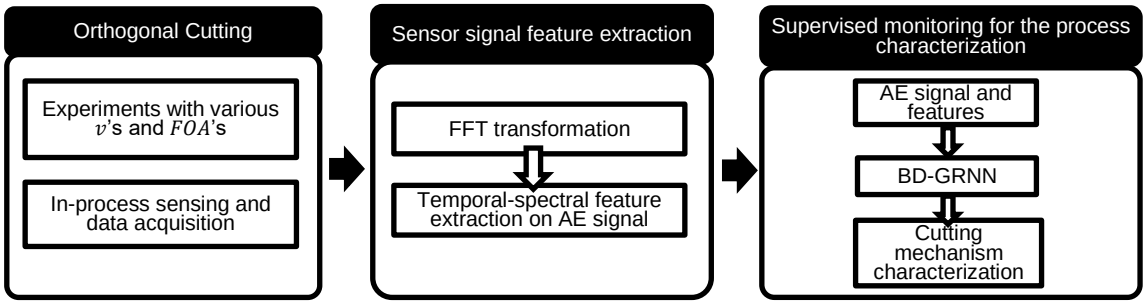

Figure VI-2. A schematic diagram of the presented research approach.

General Structure of LSTM and GRU

The general recurrent neural network (RNN) can be presented as follows:

$$\boldsymbol{h_t = \mathcal{H}(W_{xh}x_t + W_{hh}h_{t-1} + b_h)} \quad (1)$$

$$\boldsymbol{y_t = W_{hy}h_t + b_y} \quad (2)$$

where x_t's, y_t's and h_t's are the inputs, outputs and the hidden states, the matrices W's are weight matrices, $\mathcal{H}$ is the hidden layer function and the b's are the bias vectors (b_h is hidden bias vector and b_y is output bias vector). Here two models of the GRNNs, namely

Long-Short Time Memory (LSTM) cell and Gated Recurrent Unit (GRU), are introduced. The LSTM uses the input, forget and output gates, and the GRU model uses the reset and update gated units. Both LSTM and GRU apply these gated units to track time-dependent recurrence relations while mitigating the issues of vanishing and/or exploding gradient problems [186]. In this chapter, we developed both LSTM and GRU based approaches for constructing the gated recurrent neural network to capture the transient nature of AE, and based on the comparisons between two presented GRNN approaches using numerical and experimental case studies, we further applied the optimal model for characterizations of AE signals during the machining processes on the NFRPs. The details about these two models are described in the following subsections.

Long Short-Term Memory (LSTM) Cell

The LSTM considers the dependencies on previous states at different timescales by applying input, forget and output gates. This feature may help capture the intermittent transient data with time-variant long-short time dependencies. One can formulate the structure of the LSTM cell as follows:

$$\boldsymbol{i_t} = \boldsymbol{\sigma}(\boldsymbol{W_{xi}x_t} + \boldsymbol{W_{hi}h_{t-1}} + \boldsymbol{W_{ci}c_{t-1}} + \boldsymbol{b_i}) \tag{3}$$

$$\boldsymbol{f_t} = \boldsymbol{\sigma}(\boldsymbol{W_{xf}x_t} + \boldsymbol{W_{hf}h_{t-1}} + \boldsymbol{W_{cf}c_{t-1}} + \boldsymbol{b_f}) \tag{4}$$

$$\boldsymbol{c_t} = \boldsymbol{f_t c_{t-1}} + \boldsymbol{i_t}\,\mathbf{tanh}\,(\boldsymbol{W_{xc}x_t} + \boldsymbol{W_{hc}h_{t-1}} + \boldsymbol{b_c}) \tag{5}$$

$$\boldsymbol{o_t} = \boldsymbol{\sigma}(\boldsymbol{W_{xo}x_t} + \boldsymbol{W_{ho}h_{t-1}} + \boldsymbol{W_{co}c_t} + \boldsymbol{b_o}) \tag{6}$$

$$\boldsymbol{h_t} = \boldsymbol{o_t}\mathbf{tanh}\,(\boldsymbol{c_t}) \tag{7}$$

where σ is the activation function (which often time is selected as the logistic sigmoid function), and i, f, o and c are respectively the input gate, forget gate, output gate and cell activation vectors (with the same size as the hidden vector h). The matrices W's are the weight parameters for different memory cells: W_{xi} is the weight matrix for the input gate, W_{hi} is the matrix connecting hidden layer and the input gate, and W_{ci} connects the cell activation and the input gate. W_{xf}, W_{hf} and W_{cf} are the matrices connecting the inputs, the hidden layers and the activation vector to the forget gate, and similarly, W_{xo} , W_{ho} , W_{co} are the matrices connecting inputs, hidden layers, and activation vector to the output gate. b's are the bias vectors (e.g., b_i is input gate bias vector and b_f is forget gate bias vector).

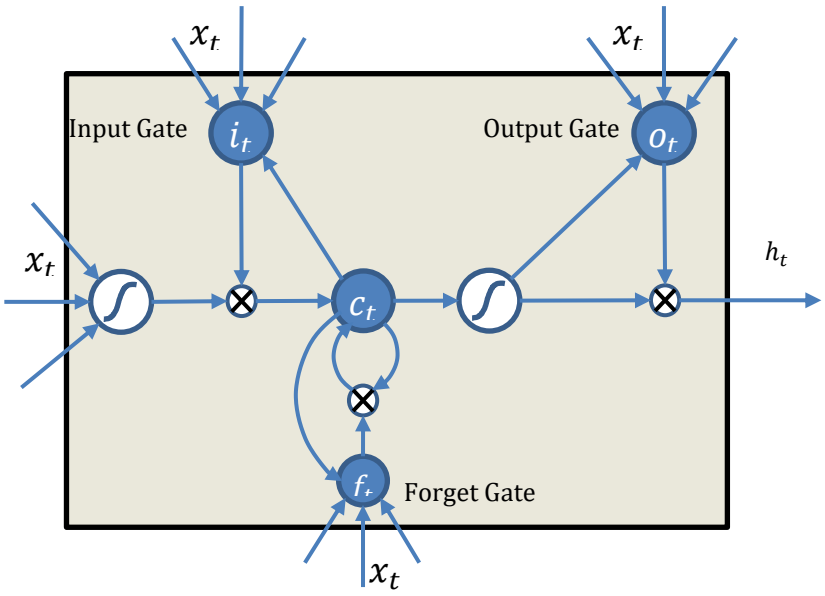

Figure VI-3. A schematic diagram showing the structure of a LSTM cell [187].

Gated Recurrent Unit (GRU)

Compared to the LSTM cell, the general GRU unit does not possess a separated memory (c_t) or the output gate. Instead, it applies recurrent reset and update units for capturing the time dependent features at different time scales [186]. A general GRU can be formulated as follows:

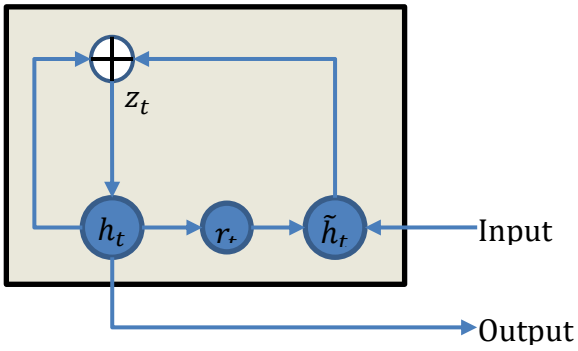

Figure VI-4. A schematic diagram showing the structure of a GRU unit [187].

$$\boldsymbol{z_t = \sigma(W_{xz}x_t + W_{hz}h_{t-1} + b_z)} \quad (8)$$

$$\boldsymbol{r_t = \sigma(W_{xr}x_t + W_{hr}h_{t-1} + b_r)} \quad (9)$$

$$\boldsymbol{\tilde{h}_t = \tanh\left(W_{x\tilde{h}}x_t + W_{r\tilde{h}}(r_t \circ h_{t-1}) + b_{\tilde{h}}\right)} \quad (10)$$

$$\boldsymbol{h_t = (1 - z_t)h_{t-1} + z_t\tilde{h}_t} \quad (11)$$

Here z_t and r_t are respectively update gate and reset gate vectors, the activation h_t at time t is a linear interpolation between the previous activation h_{t-1} and the candidate activation $\tilde{h}_t$, b's are the bias vectors for different cells (b_z, b_z and $b_{\tilde{h}}$ are the bias terms for the update gate, the reset gate and the candidate activation $\tilde{h}_.$, respectively), W's are the weight

matrices (e.g., W_{xz} is the matrix between the inputs x and the update gate z) and the activation function σ is chosen with the sigmoid kernel. The operator $\circ$ denotes a Hadamard product.

Bidirectional LSTM and GRU

As one drawback of the RNNs, they only consider the previous information for inferencing the system outputs, the bidirectional gated recurrent neural network (BD-GRNN) is applied to characterize the AE signal with the transient nature by considering the forward and backward states for inferencing the transient burst and jumps between sojourns/ stationary segments. In general, the BD-GRNN contains two sets of layers (one for forward information and the other from the backward direction). One can extend the formulas to a BD-GRNN as follows:

$$\vec{\boldsymbol{h}}_{\boldsymbol{t}} = \mathcal{H}(\boldsymbol{W}_{\boldsymbol{x}\vec{\boldsymbol{h}}}\boldsymbol{x}_{\boldsymbol{t}} + \boldsymbol{W}_{\vec{\boldsymbol{h}}\vec{\boldsymbol{h}}}\vec{\boldsymbol{h}}_{\boldsymbol{t-1}} + \boldsymbol{b}_{\vec{\boldsymbol{h}}}) \tag{12}$$

$$\overleftarrow{\boldsymbol{h}}_{\boldsymbol{t}} = \mathcal{H}(\boldsymbol{W}_{\boldsymbol{x}\overleftarrow{\boldsymbol{h}}}\boldsymbol{x}_{\boldsymbol{t}} + \boldsymbol{W}_{\overleftarrow{\boldsymbol{h}}\overleftarrow{\boldsymbol{h}}}\overleftarrow{\boldsymbol{h}}_{\boldsymbol{t-1}} + \boldsymbol{b}_{\overleftarrow{\boldsymbol{h}}}) \tag{13}$$

$$\boldsymbol{y}_{\boldsymbol{t}} = \boldsymbol{W}_{\vec{\boldsymbol{h}}\boldsymbol{y}}\vec{\boldsymbol{h}}_{\boldsymbol{t}} + \boldsymbol{W}_{\overleftarrow{\boldsymbol{h}}\boldsymbol{y}}\overleftarrow{\boldsymbol{h}}_{\boldsymbol{t}} + \boldsymbol{b}_{\boldsymbol{y}} \tag{14}$$

The BD-GRNN contains the forward hidden sequence $\vec{h}$, the backward hidden sequence $\overleftarrow{h}$ and the output sequence y. The matrices $W_{\cdot}$'s are different weights for the associated layers (e.g., $W_{x\overleftarrow{h}}$ connects the inputs x and the backward hidden layer $\overleftarrow{h}$). $b_{\vec{h}}$, $b_{\overleftarrow{h}}$ and b_y are the bias vectors for forward hidden layer, backward hidden layer and the output layer, respectively.

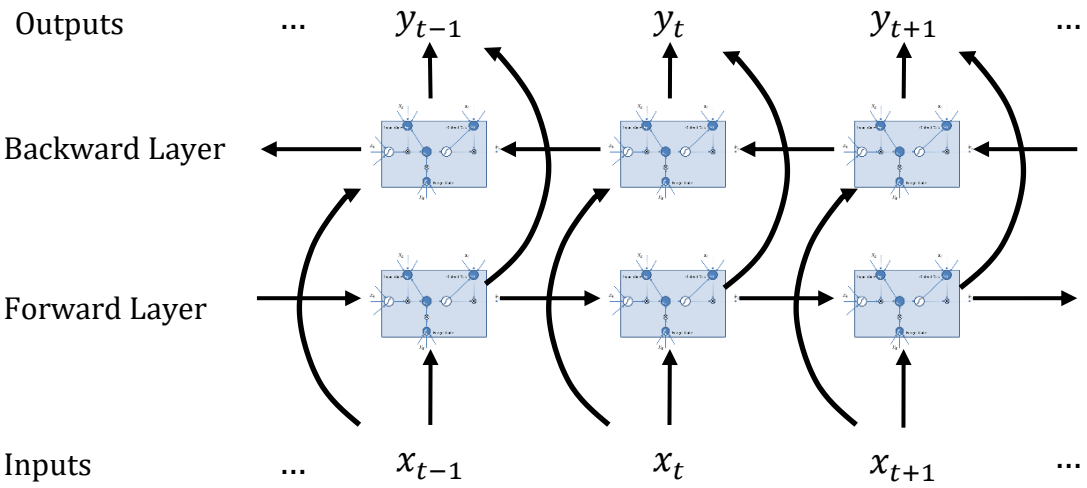

Figure VI-5. A schematic diagram of a BD-GRNN neural network where each blue colored box represents a gated unit.

As suggested by the schematic diagrams of LSTM and GRU in Figures 3 and 4, it may be noticed that, compared to the conventional RNN, the gate units in LSTM and GRU (e.g., the memory cell of the LSTM and the update/reset gate of the GRU) keep the present states and add the new content on top of it, which in turn constructs the recurrent relations (similar to the iterative map for modeling the nonstationary dynamic systems). Such a scheme provides prominent feature towards capturing the transient behaviors of the input data.

Capturing transient behaviors using LSTM and GRU

An illustrative example based on the chord progression of major pentatonic scale is presented to demonstrate the capability of the presented approach for characterizations of transient processes. As noted earlier, such a chord progression follows an intermittent

dynamics [6], and is therefore well-suited to illustrating the performance of our approach. Figure VI-6 shows a representative snippet of the symbolic sequence of chord progressions. Here the *y* axis represents different chords (each chord is tokenized with a unique number) and *x* axis is the time index. It may be noticed that the simulated chord sequences are with intermittent transitions between different scales.

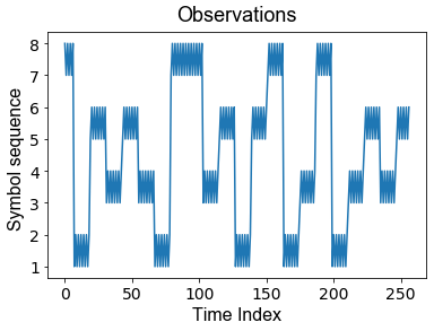

Figure VI-6. A plot of the symbolic sequence showing the tokenized chord progressions. Each chord is encoded with a unique number, i.e., {1: 'B', 2: 'E', 3: 'B^{b}', 4: 'F', 5: 'A', 6: 'D', 7: 'G', 8: 'C'}.

The implemented model has two layers of the gated units for both forward and backward directions with a detailed structure as plotted in Figure VI-7 b). Each layer is set with neuron nodes as 100, the batch size is set as 40, and the training epoch is selected around 30 to ensure that the loss function value during training converges to its minimal. The prediction performance on the trained BD-LSTM as well as BD-GRU is tested on simulated chord progressions.

The results of BD-LSTM for one-step and 5-step look ahead predictions (i.e., forecasts) are correspondingly shown in Figures 8 a) and c). In comparison, Figures 8 b) and d) include the prediction results from BD-GRU for one and 5-step forecasting. The observations (symbolic sequence) are plotted using blue solid lines while the dash red lines represent the estimated sequences. Remarkably, as illustrated in the magnified block (green-colored) in Figure VI-8, the BD-GRNN model is able to capture the transitions between scales as it accurately predicts the jumps among multiple sojourns (in-between segments of the chord progressions). It is evident that both one-step and 5-step predictions for both BD-LSTM and BD-GRU models possess high accuracies demonstrated by nearly 100% for the R-squared values as shown in Table VI-1.

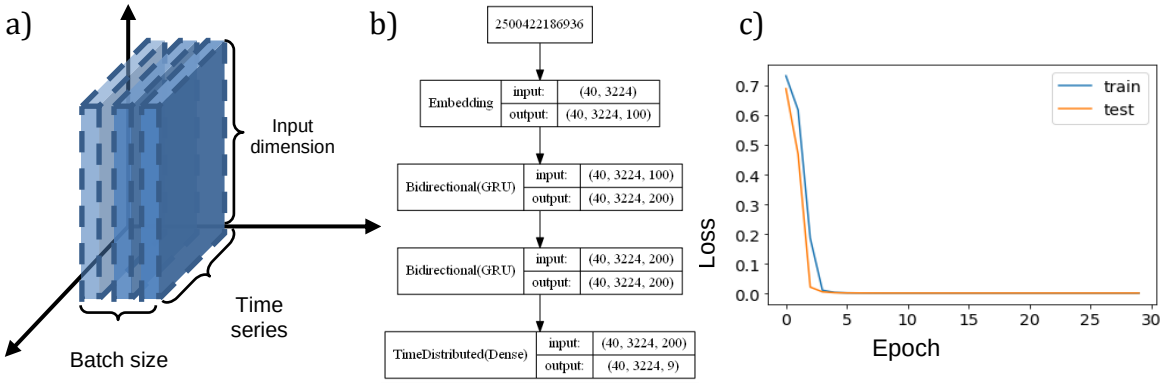

Figure VI-7. a) a schematic diagram for the structure of input variables, b) the hierarchical structure of the bidirectional neural network and c) the losses with training and cross-validation.

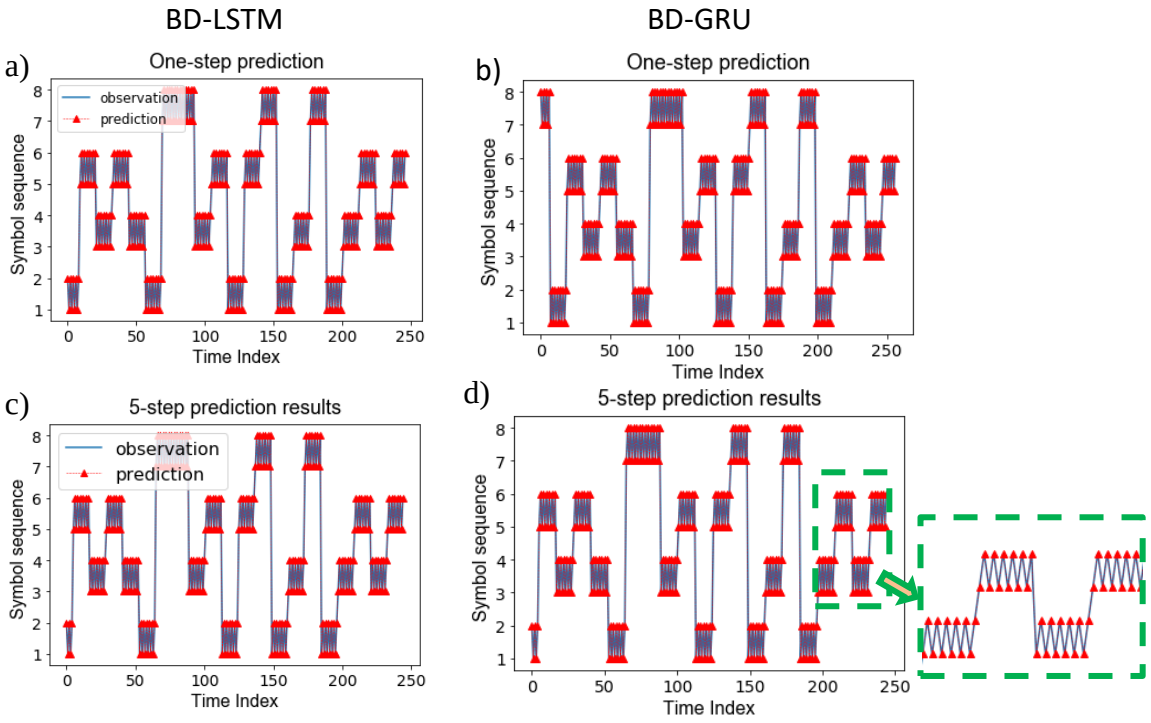

Figure VI-8. Result comparisons of one(multi)-step ahead of predictions where a) and c) are generated from BD-LSTM and b) & d) list the results from the BD-GRU model. Here the predicted sequences are plotted with red dash lines, the ground truth is shown using the blue lines, and the green colored dash squares magnify the snip of prediction result. Both one-step [a) BD-LSTM vs. b) BD-GRU] and multi-step [c) BD-LSTM vs. d) BD-GRU] predictions suggest that two developed models can finely capture the jumps between stationary segments of the chord progression transitions.

Table VI-1. Accuracy for symbolic sequence prediction.

R-squared	One step	Five steps
BD-LSTM	0.99	0.99
BD-GRU	0.99	0.99

From the numerical case study, one can conclude that the developed BD-GRNNs can properly capture the complicated recurrence relations between states. The transient AE signals may exhibit similar recurrent patterns, which combines irregular bursts and stationary segments caused by the material fracture and intermittent dislocations during machining. Hence, the presented approaches have prominent application merits towards capturing the intermittent AE waveform signals for monitoring machining process: as the model trains the gates to construct the recurrence relations using the sequential data, it captures the transient behaviors of the AE signals under different machining conditions. To test the presented approach towards smart sensing for AE characterizations, an experimental case study on machining NFRP processes was further investigated. Details on the experiment setup as well as the case study results are presented in the following sections.

The Temporal-spectral based GRNN for AE Characterizations

Experimental setup, signal processing and feature extraction

Multiple sets of experiments were conducted on an orthogonal cutting testbed as shown in the schematic diagram in Figure VI-9. The configuration is applied with the same setup described in Chapter V.

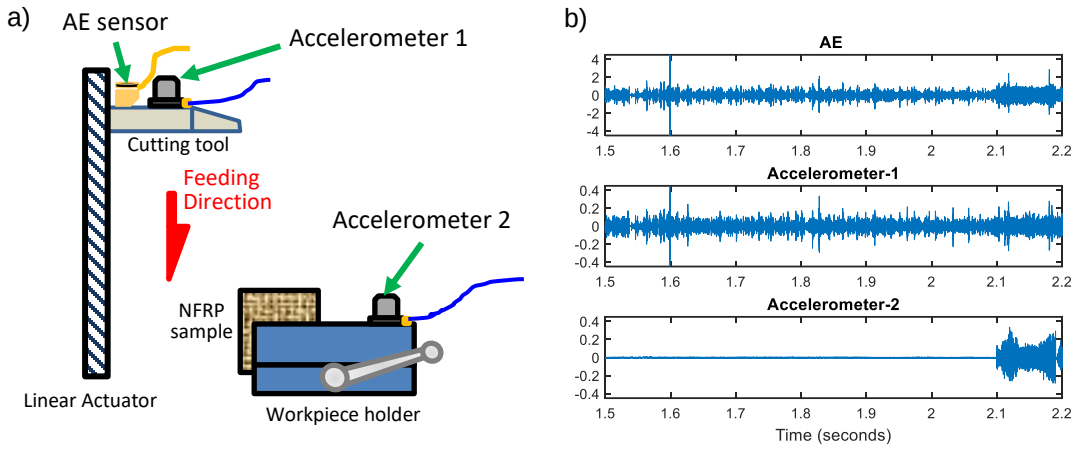

Figure VI-9. A schematic diagram showing the experimental setup: a) the orthogonal cutting process with mounted AE and vibration sensors, and b) the collected signals from AE sensor and two vibration sensors during an orthogonal cutting experiment ($FOA = 0^{\circ}$ and $v = 4\ m/min$).

A set of the representative sensor signals synchronously collected from the two accelerometers (separately mounted on the tool holder and the workpiece holder) and the AE sensor (on the tool holder) is shown in Figure VI-9 b). It may be noticed that the Accelerometer 2 (attached to the workpiece holder) can properly separate the dynamics of the cutting and the non-cutting stages due to its sudden increase in amplitude when the cutting initiates. This allows us to isolate the signals of the cutting and the non-cutting stages.

Here the feature extraction is similar as described in Sec.4.2 of Chapter V. Note that the multi-sensor setup segments the cutting and the non-cutting phases for the time-frequency features. τ_1 and τ_2 are the start and end time stamps of the segment for the cutting phase. The response vector $\boldsymbol{Y}$, during the cutting phase, contains the control parameters for the designed experiments, i.e., $\boldsymbol{Y}^{(t)} = \left[FOA^{(t)}, v^{(t)}\right]^{\mathsf{T}}$ for $t = \tau_1 + L, \tau_1 +$

$L+\vartheta, \tau_1+L+2\vartheta \ldots, \min(T, \tau_2)$, where $FOA \in \{0°, 45°, 90°\}$ and the cutting speed $v \in \{2,4,6,8,10,12\}$ (m/min). Given the time duration T_0 (in seconds) of the recording, let $T = T_0 \times Fs$, where Fs is the sampling rate ($Fs = 1$ MHz for all experiment recordings). Then, the extracted features $\boldsymbol{X}$'s as well as the process responses $\boldsymbol{Y}$'s for a single recording Ω could be represented in the following format:

$$\boldsymbol{\Omega} = \left[\boldsymbol{X}^{(t)\top}, \boldsymbol{Y}^{(t)\top}\right]^{\top} = \begin{bmatrix} \boldsymbol{X}^{(L)} & \boldsymbol{X}^{(L+\vartheta)} & \boldsymbol{X}^{(L+2\vartheta)} & \ldots & \boldsymbol{X}^{(T)} \\ \boldsymbol{Y}^{(L)} & \boldsymbol{Y}^{(L+2\vartheta)} & \boldsymbol{Y}^{(L+2\vartheta)} & \ldots & \boldsymbol{Y}^{(T)} \end{bmatrix} \quad \textbf{(16)}$$

The GRNN model is applied to capture the empirical relationships of the AE spectral features $\{\boldsymbol{X}^{(t)}\}$ with$\{y^{(t)}\}$, where $y^{(t)}$ is a subset of the response $\{\boldsymbol{Y}^{(t)}\}$ (e.g., $y^{(t)} = FOA^{(t)}$ for classification of the fiber orientations). To create the GRNN models [188], the data augmentation is needed to ensure that all the input sequences for both training and testing data to have the same lengths. One straightforward way is to repeat the temporal-spectral feature data $\{\boldsymbol{X}^{(t)}\}$ and responses $\{y^{(t)}\}$ in the testing data set until the length of $\{\boldsymbol{X}^{(t)}\}$ in testing set is equal to $\{\boldsymbol{X}^{(t)}\}$ in training set. To ensure the training data set for each set of parameters has the same data length, we subtract around 250 ms information for each cutting experiment. For those recordings with less time duration, a sequential looping is applied until such a recording is filled with 250 ms duration.

BD-LSTM and BD-GRU for monitoring the cutting condition variations with respect to fiber orientations

Given the extracted time-frequency features $\{\boldsymbol{X}^{(t)}\}$ and the response $\{y^{(t)}\} = \left\{FOA^{(t)}\right\}$, the BD-LSTM & GRU models are applied for classifying the cutting conditions. The details of the structure of the BD- LSTM & BD-GRU are described as follows.

The input as the extracted temporal-spectral features is with the dimension as $T \times 2499$ where T is the length/duration of the temporal spectral data with 2499 rows of the frequency component ranging from 0 to 500kHz (with 200Hz resolution). Here the number of hidden nodes is selected as 40 to predict the outputs (different fiber orientations). The batch size is selected as 36. The results from an 18-fold cross validation (which ensures the test data contains every condition from 6 cutting speeds × 3 FOA's) in terms of the confusion matrix is listed in Table VI-2. In total, the classification accuracy is around 88% for different fiber orientation conditions using BD-GRU.

Table VI-2. Confusion matrices for various fiber orientations (BD-GRU vs. BD-LSTM).

BD-GRU		Predicted		
		0°	45°	90°
Actual	0°	0.9997	0.0000	0.0003
	45°	0.0481	0.9519	0.0000
	90°	0.0045	0.0000	0.9955

BD-LSTM		Predicted		
		0°	45°	90°
Actual	0°	0.8247	0.1139	0.0615
	45°	0.0156	0.8179	0.1665
	90°	0.0144	0.0024	0.9832

Both BD-LSTM & BD-GRU were then applied to test the prediction accuracy on the sequence of each recording. In total, 36 experiment recordings (with various cutting speed and fiber orientations) were selected in training sets and 18 recordings were included in testing set. The classification results are listed in the Table VI-3.

Table VI-3. Testing results for various fiber orientations (BD-GRU vs. BD-LSTM).

BD-GRU		Predicted		
		0°	45°	90°
Actual	0°	1.0000	0.0000	0.0000
	45°	0.3333	0.6667	0.0000
	90°	0.0000	0.0000	1.0000

BD-LSTM		Predicted		
		0°	45°	90°
Actual	0°	0.8333	0.1667	0.0000
	45°	0.0000	0.8333	0.1667
	90°	0.0000	0.0000	1.0000

We then compare the results with an earlier investigation on analyzing AE characteristics using random forest (RF) model[13] listed in Table VI-4. Though the result from the RF model suggests a statistically significant difference between the study cases with $FOA = 0^{\circ}$ and all others, it could only recognize the difference for $FOA = 45^{\circ}$ and 90° with around 60% accuracy. Comparatively, both BD-LSTM and BD-GRU outperform the RF model with consistent accuracy over 87% towards characterizations of AE signals related to different cutting conditions (FOA's), while BD-GRU consistently achieve higher accuracy for both training and testing.

Table VI-4. Cross-validation results for various FOA's using the random forest.

Confusion Matrix		Predicted		
		0°	45°	90°
Actual	0°	0.8531	0.1259	0.0210
	45°	0.1354	0.7446	0.1200
	90°	0.2047	0.1913	0.6040

AE Characterizations under different cutting conditions

The presented approach was then applied to classify cutting conditions considering the effects of both FOA's and cutting speeds for machining NFRP. The Gate Recurrent Unit (GRU) was applied to construct the BD-GRNN since it achieves higher classification accuracy (compared with LSTM) towards characterizations of AE temporal-frequency features. The number of nodes N_h is selected as

$$N_h = \frac{\#\ total\ samples}{\eta \cdot (\#output\ neurons + \#input\ neurons)} \tag{17}$$

where the scaling factor η is set as 2 [189]. Hence, the number of hidden nodes were selected as 30 for both the forward and backward hidden layers. The activation function uses the *tanh* function and the batch size equals to 36. The parameters were selected based on numerical case studies towards multiple settings of the neural network for achieving the highest accuracy.

Classification results in terms of recall/TPR values for both cutting speeds and fiber orientations (in total 18 conditions) are shown in Table VI-5. Each row represents an FOA and columns are the collection of different cutting speeds. It may be noticed that for the higher speed conditions ($v = 10$ and $12\ m/min$), most cases achieve high TPR (nearly 100%) for connecting the AE temporal-frequency features to the cutting conditions.

However, the classification errors increase when discerning conditions with minor changes in cutting speeds under the same FOA's.

Table VI-5. Cross-validation results (Recall/TPR)

Recall	Cutting speed (m/min)					
FOA	2	4	6	8	10	12
0	0.9912	0.9621	0.8801	0.6169	0.9231	0.9975
45	0.8893	0.8001	0.6611	0.8598	0.7470	0.9902
90	0.7795	0.7064	0.9951	0.9956	0.9804	0.9581

Details about TPR/Recall values given these 18 conditions are listed in Table VI-6, where the first column (or row) lists the FOA's and the second column (or row) enumerates different cutting speeds (m/min), the diagonal elements (salmon colored) are the true positive rates (TPR), and all the non-diagonal ones represent the false negative rates (FNR). Now we investigate the classification errors under each condition. Taking the machining condition $FOA = 0^{\circ}$ and $v = 10\ m/min$ as one example, note that even though such a condition achieves a high accuracy (over 90% of the TPR), it still has the misclassified portion(s) sourced from the condition $FOA = 0^{\circ}$ and $v = 8\ m/min$. Similarly, as for the condition as $FOA = 0^{\circ}$ and $v = 2$ m/min, its false negatives are mostly classified as the conditions with the same orientation ($FOA = 0^{\circ}$) but the different cutting speed as v =4 m/min.

Table VI-6. Confusion matrix for 18 conditions with varying cutting speeds (2, 4, 6, 8, 10, 12 m/min) and FOA (0°, 45°, 90°)

	FOA	0	45	90	0	45	90	0	45	90	0	45	90	0	45	90	0	45	90
FOA	Cutting Speed	10	10	10	12	12	12	2	2	2	4	4	4	6	6	6	8	8	8
0	10	0.923	0	0	0.05	0	0	0	0	0	0.009	0	0	0.005	0	0	0.011	0	0
45	10	0.084	0.746	0	0.002	0	0	0	0.001	0	0	0	0	0.111	0	0	0.044	0.007	0
90	10	0	0	0.98	0	0	0	0	0	0	0	0	0	0.014	0	0	0.002	0	0.001
0	12	0	0.001	0	0.997	0	0	0	0	0	0	0	0	0	0	0	0	0	0
45	12	0	0.006	0	0.002	0.99	0	0	0	0	0	0	0	0	0	0	0	0	0
90	12	0	0	0.041	0	0	0.958	0	0	0	0	0	0	0	0	0	0	0	0
0	2	0	0	0	0	0	0	0.991	0.002	0	0.005	0	0	0	0	0	0	0	0
45	2	0	0.002	0	0	0	0	0	0.889	0	0.036	0.023	0	0.048	0	0	0	0	0
90	2	0	0	0	0	0	0	0	0	0.779	0	0	0.209	0	0	0.01	0	0	0
0	4	0	0	0	0	0	0	0.031	0.002	0	0.962	0.001	0	0	0	0	0	0	0
45	4	0	0	0	0	0	0	0	0	0	0	0.8	0	0	0.199	0	0	0	0
90	4	0	0	0	0	0	0	0	0	0.252	0	0	0.706	0	0	0.04	0	0	0
0	6	0	0	0	0.002	0	0	0	0.003	0	0	0	0	0.88	0.016	0	0.096	0	0
45	6	0	0.001	0	0	0	0	0	0.01	0	0	0.007	0	0.145	0.661	0	0.001	0.173	0
90	6	0	0	0	0	0	0	0	0	0.004	0	0	0	0	0	0.995	0	0	0
0	8	0.175	0	0	0.006	0	0	0	0	0	0	0	0	0.195	0	0	0.616	0.005	0
45	8	0	0.042	0	0.001	0	0	0	0.003	0	0	0	0	0.06	0.013	0	0.018	0.859	0
90	8	0	0	0	0	0	0	0	0	0	0	0	0	0	0	0.004	0	0	0.995

It may suggest that most false negatives are misclassified in adjacent groups with different cutting speeds but the same FOA. The reason why AE signatures are more distinguishable under different FOA's is because that different FOA's lead to distinct combinations of cutting mechanisms [13]: under all $FOA = 0°$ conditions, the cutting mechanisms are predominantly with the PP matrix removal, and with some fibers sliding/shearing along interfacial areas during the material removal; as for the 45° orientation position, the cutting mechanism consists of compression induced interfacial shearing along the fiber orientation direction that causes fiber-matrix debonding; for $FOA = 90°$, the fractures that contribute predominantly to fiber pull-out emerge intermittently. Different failure modes during material removal may attribute to different frequency responses of the AE sensor signals. However, classification results also suggest

that minor changes in the cutting speed is still less influential on the variations of the resultant temporal-spectral AE features compared to the fiber orientations (FOA's).

Despite those groups with comparatively higher false positives (conditions misclassified in adjacent cutting speeds), the presented BD-GRU could achieve an overall ~87% accuracy while the preciously investigated random forest could not correctly classified the AE characteristics with respect to the FOA's.

Summary and Concluding Remarks

This chapter presented a framework using recurrent deep learning approach for real-time monitoring and characterization of sensor signals under transient phase. The temporal-spectral features of AE signals during the NFRPs machining processes were selected to test the performance of the presented BD-GRNNs. Admittedly, the feature extraction and selection for the temporal spectral components remain a major challenge, and investigations into advanced machine learning approach may be needed for efficiently selecting energy components within specific frequency band(s). However, the developed GRNNs allows a selection of useful information from the time-frequency features (by training the weights of each neuron) and uses gated units to capture the underlying process dynamics on the time-varying spectral information. Thus, it avoids ad-hoc feature selection and extraction. The contributions of this chapter are listed below:

- A case study for multi-step prediction is presented to show the performance of the BD-RNN for capturing the transient nature of signals. The numerical case study

results indicate that the GRNN can capture transients (intermittent jumps) between stationary segments;

- The GRNNs (both LSTM and GRU models) are presented for characterizing the AE signals with different transient phase patterns (laminar phases, and variations on the modulated time series coefficients). The presented approach achieves around 87% accuracy, which outperforms other advanced machine learning approaches such as random forest classification. Thus, GRNNs allow the real-time process characterizations for machining NFRPs with changes of machining parameters as well as the microstructure variations.

For the future work, other factors, such as the heterogeneity of the fiber distribution over the matrix and chip formations, need to be further considered for characterizations of the AE signals for NFRP machining processes.

References

[5] Wang, Z., Bukkapatnam, S. T. S., Kumara, S. R. T., Kong, Z., and Katz, Z., 2014, "Change detection in precision manufacturing processes under transient conditions", CIRP Annals - Manufacturing Technology, **63**(1), pp: 449-452. http://dx.doi.org/10.1016/j.cirp.2014.03.123.

[6] Wang, Z., and Bukkapatnam, S. T., 2018, "A Dirichlet process Gaussian state machine model for change detection in transient processes", Technometrics, **60**(3), pp: 373--385. https://doi.org/10.1080/00401706.2017.1371079.

[13] Wang, Z., Chegdani, F., Yalamarti, N., Takabi, B., Tai, B., Mansori, M. E., and Bukkapatnam, S. T., 2020, "Acoustic Emission (AE) characterization of natural fiber reinforced plastic (NFRP) composite machining using a random forest machine learning model", Journal of Manufacturing Science and Engineering, **142**(3), pp: 031003.

[137] Lee, D.-E., Hwang, I., Valente, C. M., Oliveira, J., and Dornfeld, D. A., 2006, "Precision manufacturing process monitoring with acoustic emission", International Journal of Machine Tools and Manufacture, **46**(2), pp: 176-188.

[143] Dornfeld, D., and Kannatey-Asibu, E., 1980, "Acoustic emission during orthogonal metal cutting", International Journal of Mechanical Sciences, **22**(5), pp: 285-296.

[181] Peças, P., Carvalho, H., Salman, H., and Leite, M., 2018, "Natural fibre composites and their applications: a review", Journal of Composites Science, **2**(4), pp: 66.

[182] Hollaway, L., and Head, P., 2000, "Composite materials and structures in civil engineering", Comprehensive Composite Materials, Elsevier Ltd, pp: 489-527.

[183] Barry, J., Byrne, G., and Lennon, D., 2001, "Observations on chip formation and acoustic emission in machining Ti–6Al–4V alloy", International Journal of Machine Tools and Manufacture, **41**(7), pp: 1055-1070.

[184] Bukkapatnam, S. T., Kumara, S. R., and Lakhtakia, A., 1999, "Analysis of acoustic emission signals in machining", Journal of manufacturing science and engineering, **121**(4), pp: 568-576.

[185] Kelly, A., and Zweben, C., 2000, Comprehensive Composite Materials, Elsevier Ltd.

[186] Chung, J., Gulcehre, C., Cho, K., and Bengio, Y., 2014, "Empirical evaluation of gated recurrent neural networks on sequence modeling", arXiv preprint arXiv:1412.3555.

[187] Hochreiter, S., and Schmidhuber, J., 1997, "Long short-term memory", Neural computation, **9**(8), pp: 1735-1780.

[188] François, C., 2015, "Keras", GitHub repository.

[189] Stathakis, D., 2009, "How many hidden layers and nodes?", International Journal of Remote Sensing, **30**(8), pp: 2133-2147.

CHAPTER VII

CONCLUSIONS

In this dissertation, smart sensing approaches and their implementations in different advanced manufacturing processes are provided.

First, I investigated the nature of dynamics of precision manufacturing processes to address associated quality assurance problems. A nonparametric Bayesian model was presented to model the inherent nonstationarity (i.e., dynamic intermittency) borne in the (ultra)precision machining processes. Such an approach allows timely diagnosis (anomaly detection) and intervention for incipient anomalies causing quality issues for precision machining processes.

For in-process surface quality inspection, the vision based approaches are presented to 1) quantitively predict the impacts of surface defects on the surface morphology and 2) capture the evolution of surface evolution in real-time and implement it in the cyber-physical environment to realize close-loop control for laser origami sheet forming processes.

Towards advancing the smart sensing/manufacturing, I investigated the capability of advanced sensor-based monitoring setup to characterize the manufacturing processes at micro-metric level. Extensive experimental case studies suggest that the presented sensor-based approaches enable connecting the characteristics of AE sensor signals to the microdynamics of the machining processes that reflect distinct failure modes. Hence, the

presented approach is able to characterize the process for machining NFRPs with changes of machining parameters as well as the microstructure variations in real-time.

There are several topics could be explored in my future research.

For the real-time vision-based approach, future work could be extended towards creating digital-twin of the processes for real-time monitoring, characterizations and control with potential applications in other machining processes, such as shaping processes. The advanced vision-based approach extended from this project would also be also applied to create augmented reality of the shop floor, which offers tremendous advantages towards creating cyber-physical smart material handling system/ platform for the shop floor.

As for in-process monitoring approaches for manufacturing processes, this dissertation discusses the approach for characterizations of the dynamics for the processes (Chapter II). Furthermore, the investigations into AE sensor (in Chapters V, VI and VII) shed significant light on capturing the machining processes using AE features related to the microdynamics as well as variations on material microstructure. Future work can focus on real-time characterizations of the mechanical property (as such materials possess heterogeneity/variations in their microstructures) and/or predictions of achieved surface morphology by analyzing the characteristics of AE data related to different material removal mechanisms and microdynamics of the processes.

BIBLIOGRAPHY

Kim, K.-D., and Kumar, P. R., 2012, "Cyber–physical systems: A perspective at the centennial", Proceedings of the IEEE, **100**, pp: 1287-1308.

Lee, J., Bagheri, B., and Jin, C., 2016, "Introduction to cyber manufacturing", Manufacturing Letters, **8**, pp: 11-15.

Monostori, L., 2014, "Cyber-physical production systems: Roots, expectations and R&D challenges", Procedia CIRP, **17**, pp: 9-13.

Jeschke, S., Brecher, C., Meisen, T., Özdemir, D., and Eschert, T., 2017, "Industrial internet of things and cyber manufacturing systems", Industrial internet of things, Springer, Cham, pp: 3-19.

Wang, Z., Bukkapatnam, S. T. S., Kumara, S. R. T., Kong, Z., and Katz, Z., 2014, "Change detection in precision manufacturing processes under transient conditions", CIRP Annals - Manufacturing Technology, **63**(1), pp: 449-452. http://dx.doi.org/10.1016/j.cirp.2014.03.123.

Wang, Z., and Bukkapatnam, S. T., 2018, "A Dirichlet process Gaussian state machine model for change detection in transient processes", Technometrics, **60**(3), pp: 373--385. https://doi.org/10.1080/00401706.2017.1371079.

Iquebal, A. S., El Amri, S., Shrestha, S., Wang, Z., Manogharan, G. P., and Bukkapatnam, S., 2017, "Longitudinal milling and fine abrasive finishing operations to improve surface integrity of metal am components", Procedia Manufacturing, **10**, pp: 990-996.

Cheng, C., Wang, Z., Hung, W., Bukkapatnam, S. T., and Komanduri, R., 2015, "Ultra-precision machining process dynamics and surface quality monitoring", Procedia Manufacturing, **1**, pp: 607-618.

Wang, Z., Iquebal, A. S., and Bukkapatnam, S. T., 2018, "A vision-based monitoring approach for real-time control of laser origami cybermanufacturing processes", Procedia Manufacturing, **26**, pp: 1307-1317.

Iquebal, A. S., Wang, Z., Ko, W.-H., Wang, Z., Kumar, P., Srinivasa, A., and Bukkapatnam, S. T., 2018, "Towards realizing cybermanufacturing Kiosks: quality assurance challenges and opportunities", Procedia Manufacturing, **26**, pp: 1296-1306.

Wang, Z., Kovvuri, V., Araujo, A., Bacci, M., Hung, W., and Bukkapatnam, S., 2016, "Built-up-edge effects on surface deterioration in micromilling processes", Journal of Manufacturing Processes, **24**, pp: 321-327.

Botcha, B., Wang, Z., Rajan, S., Gautam, N., Bukkapatnam, S. T., Manthanwar, A., Scott, M., Schneider, D., and Korambath, P., 2018, "Implementing the transformation of discrete part manufacturing systems into smart manufacturing platforms", Proc. of ASME 2018 13th International Manufacturing Science and Engineering Conference,College Station, Texas, USA, American Society of Mechanical Engineers Digital Collection.

Wang, Z., Chegdani, F., Yalamarti, N., Takabi, B., Tai, B., Mansori, M. E., and Bukkapatnam, S. T., 2020, "Acoustic Emission (AE) characterization of natural fiber reinforced plastic (NFRP) composite machining using a random forest machine learning model", Journal of Manufacturing Science and Engineering, **142**(3), pp: 031003.

Wang, Z., Dixit, P., Chegdani, F., Takabi, B., Tai, B. L., El Mansori, M., and Bukkapatnam, S., 2020, "Bidirectional Gated Recurrent Deep Learning Neural Networks for Smart Acoustic Emission Sensing of Natural Fiber–Reinforced Polymer Composite Machining Process ", Smart and Sustainable Manufacturing Systems (In press). https://doi.org/10.1520/SSMS20190042.

Raghavan, V., and Veeravalli, V. V., 2010, "Quickest Change Detection of a Markov Process Across a Sensor Array", IEEE Transactions on Information Theory, **56**(4), pp: 1961-1981. https://dx.doi.org/10.1109/TIT.2010.2040869.

Érdi, P., and Lente, G., 2014, Stochastic chemical kinetics: Theory and (Mostly) Systems Biological Applications, vol. 1, Springer, New York.

Cheng, C., Sa-ngasoongsong, A., Beyca, O., Le, T., Yang, H., Kong, Z., and Bukkapatnam, S. T. S., 2015, "Time Series Forecasting for Nonlinear and Nonstationary Processes: A Review and Comparative Study", IIE Transactions, **47**(10), pp: 1053-1071. https://dx.doi.org/10.1080/0740817X.2014.999180.

Noé, F., and Fischer, S., 2008, "Transition networks for modeling the kinetics of conformational change in macromolecules", Current Opinion in Structural Biology, **18**(2), pp: 154-162. http://dx.doi.org/10.1016/j.sbi.2008.01.008.

Montes De Oca, V., Jeske, D. R., Zhang, Q., Rendon, C., and Marvasti, M., 2010, "A cusum change-point detection algorithm for non-stationary sequences with application to data network surveillance", Journal of Systems and Software, **83**(7), pp: 1288-1297. http://dx.doi.org/10.1016/j.jss.2010.02.006.

Last, M., and Shumway, R., 2008, "Detecting abrupt changes in a piecewise locally stationary time series", Journal of Multivariate Analysis, **99**(2), pp: 191-214. http://dx.doi.org/10.1016/j.jmva.2007.06.010.

Choi, H., Ombao, H., and Ray, B., 2008, "Sequential change-point detection methods for nonstationary time series", Technometrics, **50**(1), pp: 40-52.

Killick, R., Eckley, I., and Jonathan, P., 2013, "A wavelet-based approach for detecting changes in second order structure within nonstationary time series", Electronic Journal of Statistics, **7**, pp: 1167-1183.

Zbilut, J. P., Thomasson, N., and Webber, C. L., 2002, "Recurrence quantification analysis as a tool for nonlinear exploration of nonstationary cardiac signals", Medical Engineering & Physics, **24**(1), pp: 53-60. http://dx.doi.org/10.1016/S1350-4533(01)00112-6.

Alippi, C., and Roveri, M., 2008, "Just-in-time adaptive classifiers—Part I: Detecting nonstationary changes", IEEE Transactions on Neural Networks, **19**(7), pp: 1145-1153.

Lai, Y.-C., 1996, "Distinct small-distance scaling behavior of on-off intermittency in chaotic dynamical systems", Physical Review E, **54**(1), pp: 321.

Zhang, M., Xu, S., and Fulcher, J., 2002, "Neuron-adaptive higher order neural-network models for automated financial data modeling", IEEE Transactions on Neural Networks, **13**(1), pp: 188-204.

Ghazali, R., Hussain, A. J., Nawi, N. M., and Mohamad, B., 2009, "Non-stationary and stationary prediction of financial time series using dynamic ridge polynomial neural network", Neurocomputing, **72**(10-12), pp: 2359-2367.

Cvitanovic, P., Artuso, R., Mainieri, R., Tanner, G., Vattay, G., and Whelan, N., 2005, Chaos: Classical and Quantum, Niels Bohr Institute, Copenhagen.

Genç, M. S., Karasu, I., Acikel, H. H., Akpolat, M. T., and Genc, M., 2012, "Low Reynolds number flows and transition", Low Reynolds Number Aerodynamics and Transition, Genc, MS Ed.; InTech: Rijeka, Croatia, pp: 1-28.

Wang, X.-J., 1989, "Statistical physics of temporal intermittency", Physical Review A, **40**(11), pp: 6647.

Isola, S., 1999, "Renewal sequences and intermittency", Journal of Statistical Physics, **97**(1-2), pp: 263-280.

Sturman, R., and Ashwin, P., 2004, "Internal dynamics of intermittency", Dynamics and Bifurcation of Patterns in Dissipative Systems, **12**, pp: 357.

Kawabata, T., and Nishikawa, K., 2000, "Protein structure comparison using the markov transition model of evolution", Proteins: Structure, Function, and Bioinformatics, **41**(1), pp: 108-122.

Bertuccelli, L. F., and How, J. P., 2008, "Estimation of non-stationary Markov chain transition models", Proc. of 47th IEEE Conference on Decision and Control,Cancun, Mexico, IEEE, pp: 55-60.

Guo, H., Paynabar, K., and Jin, J., 2012, "Multiscale monitoring of autocorrelated processes using wavelets analysis", IIE Transactions, **44**(4), pp: 312-326.

Dai, A. M., and Storkey, A. J., 2015, "The Supervised Hierarchical Dirichlet Process", IEEE Transactions on Pattern Analysis and Machine Intelligence, **37**(2), pp: 243-255. 10.1109/TPAMI.2014.2315802.

Marwan, N., Romano, M. C., Thiel, M., and Kurths, J., 2007, "Recurrence plots for the analysis of complex systems", Physics reports, **438**(5), pp: 237-329.

Bukkapatnam, S. T., and Cheng, C., 2010, "Forecasting the evolution of nonlinear and nonstationary systems using recurrence-based local Gaussian process models", Physical Review E, **82**(5), pp: 056206.

Katok, A., and Hasselblatt, B., 1997, Introduction to the modern theory of dynamical systems, vol. 54, Cambridge university press.

Liu, C.-S., 2007, "A study of type I intermittency of a circular differential equation under a discontinuous right-hand side", Journal of Mathematical Analysis and Applications, **331**(1), pp: 547-566.

Neal, R. M., 2000, "Markov chain sampling methods for Dirichlet process mixture models", Journal of Computational and Graphical Statistics, **9**(2), pp: 249-265.

Crommelin, D. T., and Vanden-Eijnden, E., 2006, "Fitting timeseries by continuous-time Markov chains: A quadratic programming approach", Journal of Computational Physics, **217**(2), pp: 782-805. http://dx.doi.org/10.1016/j.jcp.2006.01.045.

Hinrichs, N. S., and Pande, V. S., 2007, "Calculation of the distribution of eigenvalues and eigenvectors in Markovian state models for molecular dynamics", The Journal of chemical physics, **126**(24), pp: 244101.

Ghosal, S., Ghosh, J. K., and van der Vaart, A. W., 2000, "Convergence rates of posterior distributions", Annals of Statistics, **28**(2), pp: 500-531. https://doi.org/10.1214/aos/1016218228.

Ma, J., Xu, L., and Jordan, M. I., 2000, "Asymptotic convergence rate of the EM algorithm for Gaussian mixtures", Neural Computation, **12**(12), pp: 2881-2907.

Genovese, C. R., and Wasserman, L., 2000, "Rates of convergence for the Gaussian mixture sieve", The Annals of Statistics, **28**(4), pp: 1105-1127.

Ghosal, S., and Van Der Vaart, A. W., 2001, "Entropies and rates of convergence for maximum likelihood and Bayes estimation for mixtures of normal densities", Annals of Statistics, pp: 1233-1263.

Shen, W., Tokdar, S. T., and Ghosal, S., 2013, "Adaptive Bayesian multivariate density estimation with Dirichlet mixtures", Biometrika, **100**(3), pp: 623-640.

Ghosal, S., and Van Der Vaart, A., 2007, "Posterior convergence rates of Dirichlet mixtures at smooth densities", The Annals of Statistics, **35**(2), pp: 697-723.

Kristan, M., Leonardis, A., and Skočaj, D., 2011, "Multivariate online kernel density estimation with Gaussian kernels", Pattern Recognition, **44**(10–11), pp: 2630-2642. http://dx.doi.org/10.1016/j.patcog.2011.03.019.

Davis, R. A., Lee, T. C. M., and Rodriguez-Yam, G. A., 2006, "Structural break estimation for nonstationary time series models", Journal of the American Statistical Association, **101**(473), pp: 223-239.

Nakano, M., Le Roux, J., Kameoka, H., Ono, N., and Sagayama, S., 2011, "Infinite-state spectrum model for music signal analysis", Proc. of 2011 IEEE International Conference on Acoustics, Speech and Signal Processing (ICASSP),Prague, Czech Republic, 22-27 May 2011, pp: 1972-1975.

Chordia, P., and Rae, A., 2008, "Real-time Raag recognition for interactive music", Proc. of 8 th International Conference on New Interfaces for Musical Expression NIME08,Genova, Italy, pp: 331-336.

Rao, P. K., Bhushan, M. B., Bukkapatnam, S. T. S., Zhenyu, K., Byalal, S., Beyca, O. F., Fields, A., and Komanduri, R., 2014, "Process-Machine Interaction (PMI) Modeling and Monitoring of Chemical Mechanical Planarization (CMP) Process Using Wireless Vibration Sensors", IEEE Transactions on Semiconductor Manufacturing, **27**(1), pp: 1-15. https://doi.org/10.1109/TSM.2013.2293095.

Bissacco, G., Hansen, H. N., and De Chiffre, L., 2005, "Micromilling of hardened tool steel for mould making applications", Journal of Materials Processing Technology, **167**(2–3), pp: 201-207. http://dx.doi.org/10.1016/j.jmatprotec.2005.05.029.

Adams, D. P., Vasile, M. J., Benavides, G., and Campbell, A. N., 2001, "Micromilling of metal alloys with focused ion beam–fabricated tools", Precision Engineering, **25**(2), pp: 107-113. http://dx.doi.org/10.1016/S0141-6359(00)00064-7.

Liu, X., DeVor, R. E., and Kapoor, S. G., 2007, "Model-based analysis of the surface generation in microendmilling—part II: experimental validation and analysis", Journal of manufacturing science and engineering, **129**(3), pp: 461-469.

Sreeram, S., Kumar, A. S., Rahman, M., and Zaman, M., 2006, "Optimization of cutting parameters in micro end milling operations in dry cutting condition using genetic algorithms", Int J Adv Manuf Technol, **30**(11-12), pp: 1030-1039.

Jin, X., and Altintas, Y., 2012, "Prediction of micro-milling forces with finite element method", Journal of Materials Processing Technology, **212**(3), pp: 542-552.

Lauro, C., Brandão, L., Panzera, T., and Davim, J., 2015, "Surface Integrity In the Micromachining: A Review", Rev. Adv. Mater. Sci, **40**, pp: 227-234.

Huo, D., 2013, Micro-cutting: fundamentals and applications, John Wiley & Sons.

Ng, C. K., Melkote, S. N., Rahman, M., and Kumar, A. S., 2006, "Experimental study of micro-and nano-scale cutting of aluminum 7075-T6", International Journal of Machine Tools and Manufacture, **46**(9), pp: 929-936.

Ozcatalbas, Y., 2003, "Chip and built-up edge formation in the machining of in situ Al4C3–Al composite", Materials & Design, **24**(3), pp: 215-221. http://dx.doi.org/10.1016/S0261-3069(02)00146-2.

Dogra, M., Sharma, V. S., and Dureja, J., 2011, "Effect of tool geometry variation on finish turning–A Review", Journal of Engineering Science and Technology Review, **4**(1), pp: 1-13.

Masounave, J., Youssef, Y. A., Beauchamp, Y., and Thomas, M., 1997, "An experimental design for surface roughness and built-up edge formation in lathe dry turning", International Journal of Quality Science, **2**(3), pp: 167-180.

Jackson, M., 2005, "Primary chip formation during the micromachining of engineering materials", Proceedings of the Institution of Mechanical Engineers, Part B: Journal of Engineering Manufacture, **219**(3), pp: 245-254.

Selvam, M. S., and Radhakrishnan, V., 1973, "Influence of side-flow and built-up edge on the roughness and hardness of the surface machined with a single point tool", Wear, **26**(3), pp: 393-403. http://dx.doi.org/10.1016/0043-1648(73)90189-0.

Childs, T., 2011, "Towards simulating built-up-edge formation in the machining of steel", CIRP Journal of Manufacturing Science and Technology, **4**(1), pp: 57-70.

Heginbotham, W., and Gogia, S., 1961, "Metal cutting and the built-up nose", Proceedings of the Institution of Mechanical Engineers, **175**(1), pp: 892-917.

Boothroyd, G., 1988, Fundamentals of metal machining and machine tools, vol. 28, CRC Press.

Zorev, N. N., 1966, Metal cutting mechanics, Pergamon, headington Hill Hall, Oxford, England.

Shahabi, H., and Ratnam, M., 2010, "In-cycle detection of built-up edge (BUE) from 2-D images of cutting tools using machine vision", The International Journal of Advanced Manufacturing Technology, **46**(9-12), pp: 1179-1189.

Fang, N., Pai, P. S., and Edwards, N., 2010, "Prediction of built-up edge formation in machining with round edge and sharp tools using a neural network approach", International Journal of Computer Integrated Manufacturing, **23**(11), pp: 1002-1014. https://dx.doi.org/10.1080/0951192X.2010.511651.

Ucun, İ., Aslantaş, K., Gökçe, B., and Bedir, F., 2014, "Effect of tool coating materials on surface roughness in micromachining of Inconel 718 super alloy", Proceedings of the Institution of Mechanical Engineers, Part B: Journal of Engineering Manufacture, **228**(12), pp: 1550-1562.

Shaw, M., 1942, "The chemico-physical role of the cutting fluid", Metal Progress, **42**, pp: 85-91.

Chan, K. C., Cheung, C. F., Ramesh, M. V., Lee, W. B., and To, S., 2001, "A theoretical and experimental investigation of surface generation in diamond turning of an Al6061/SiCp metal matrix composite", International Journal of Mechanical Sciences, **43**(9), pp: 2047-2068. http://dx.doi.org/10.1016/S0020-7403(01)00028-5.

Kovvuri, V. R., 2015, "Experimental Study of Built-up-edge Formation in Micro Milling," Master of Science, Texas A&M University, College Station (TX).

Berestovskyi, D., Hung, W., and Lomeli, P., 2014, "Surface Finish of Ball-End Milled Microchannels", Journal of Micro and Nano-Manufacturing, **2**(4), pp: 041005.

Shaw, M. C., and Cookson, J., 2005, Metal cutting principles, 2nd ed., vol. 2, Oxford university press Oxford, UK.

Wang, M.-Y., and Chang, H.-Y., 2004, "Experimental study of surface roughness in slot end milling AL2014-T6", International Journal of Machine Tools and Manufacture, **44**(1), pp: 51-57.

Rao, P. K., Beyca, O. F., Kong, Z., Bukkapatnam, S. T. S., Case, K. E., and Komanduri, R., 2015, "A graph-theoretic approach for quantification of surface morphology variation and its application to chemical mechanical planarization process", IIE Transactions, **47**(10), pp: 1088-1111. https://dx.doi.org/10.1080/0740817X.2014.1001927.

Komanduri, R., 1993, "Machining and grinding: A historical review of the classical papers", Appl. Mech. Rev, **46**(3), pp: 80-132.

Weule, H., Hüntrup, V., and Tritschler, H., 2001, "Micro-Cutting of Steel to Meet New Requirements in Miniaturization", CIRP Annals - Manufacturing Technology, **50**(1), pp: 61-64. http://dx.doi.org/10.1016/S0007-8506(07)62071-X.

Venkatachalam, S., and Liang, S. Y., 2007, "Effects of ploughing forces and friction coefficient in microscale machining", Journal of manufacturing science and engineering, **129**(2), pp: 274-280.

Ramaswami, R., 1971, "The effect of the built-up-edge(BUE) on the wear of cutting tools", Wear, **18**(1), pp: 1-10. http://dx.doi.org/10.1016/0043-1648(71)90059-7.

Munro, B. H., 2005, Statistical methods for health care research, vol. 1, Lippincott Williams & Wilkins.

Aldrich, J., 1995, "Correlations genuine and spurious in Pearson and Yule", Statistical science, pp: 364-376.

Granger, C. W., 1969, "Investigating causal relations by econometric models and cross-spectral methods", Econometrica: Journal of the Econometric Society, pp: 424-438.

Bukkapatnam, S., and Srinivasa, A., 2015, http://tees.tamu.edu/media/197462/cyber-manufacturing-primer.pdf.

Everton, S. K., Hirsch, M., Stravroulakis, P., Leach, R. K., and Clare, A. T., 2016, "Review of in-situ process monitoring and in-situ metrology for metal additive manufacturing", Materials & Design, **95**, pp: 431-445.

Krishnan, M., Atzeni, E., Canali, R., Manfredi, D., Calignano, F., Ambrosio, E., and Iuliano, L., 2013, "Influence of post‐processing operations on mechanical properties of AlSi10Mg Parts by DMLS", Proc. of The 6th International Conference on High Value Manufacturing: Advanced Research in Virtual and Rapid Prototyping,Leiria, Portugal, CRC Press, p. 243.

Miyashita, S., Guitron, S., Li, S., and Rus, D., 2017, "Robotic metamorphosis by origami exoskeletons", Science Robotics, **2**(10), pp: eaao4369. https://dx.doi.org/10.1126/scirobotics.aao4369.

Wang, W., Li, C., Rodrigue, H., Yuan, F., Han, M. W., Cho, M., and Ahn, S. H., 2017, "Kirigami/Origami ‐ Based Soft Deployable Reflector for Optical Beam Steering", Advanced Functional Materials, **27**(7), pp: 1604214.

Onal, C. D., Tolley, M. T., Wood, R. J., and Rus, D., 2015, "Origami-inspired printed robots", IEEE/ASME Transactions on Mechatronics, **20**(5), pp: 2214-2221.

Piqué, A., Mathews, S. A., Charipar, N. A., and Birnbaum, A. J., 2012, "Laser origami: a new technique for assembling 3D microstructures", Proc. of Proceedings of SPIE, pp: 82440B-82440B.

Mueller, S., Kruck, B., and Baudisch, P., 2013, "LaserOrigami: laser-cutting 3D objects", Proc. of Proceedings of the SIGCHI Conference on Human Factors in Computing Systems, ACM, pp: 2585-2592.

Yang, H., Shao, L., Zheng, F., Wang, L., and Song, Z., 2011, "Recent advances and trends in visual tracking: A review", Neurocomputing, **74**(18), pp: 3823-3831.

Yu, G., and Morel, J.-M., 2011, "ASIFT: An algorithm for fully affine invariant comparison", Image Processing On Line, **1**, pp: 11-38.

Pan, B., Qian, K., Xie, H., and Asundi, A., 2009, "Two-dimensional digital image correlation for in-plane displacement and strain measurement: a review", Measurement science and technology, **20**(6), pp: 062001.

Garrido-Jurado, S., Muñoz-Salinas, R., Madrid-Cuevas, F. J., and Marín-Jiménez, M. J., 2014, "Automatic generation and detection of highly reliable fiducial markers under occlusion", Pattern Recognition, **47**(6), pp: 2280-2292. https://doi.org/10.1016/j.patcog.2014.01.005.

Lim, H., and Lee, Y. S., 2009, "Real-time single camera SLAM using fiducial markers", Proc. of ICCAS-SICE, 2009, IEEE, pp: 177-182.

Muñoz-Salinas, R., Marín-Jimenez, M. J., Yeguas-Bolivar, E., and Medina-Carnicer, R., 2016, "Mapping and Localization from Planar Markers", arXiv preprint arXiv:1606.00151.

Migliore, D., Rigamonti, R., Marzorati, D., Matteucci, M., and Sorrenti, D. G., 2009, "Use a single camera for simultaneous localization and mapping with mobile object tracking in dynamic environments", Proc. of ICRA Workshop on Safe navigation in open and dynamic environments: Application to autonomous vehicles, pp: 12-17.

Ceriani, S., Marzorati, D., Matteucci, M., and Sorrenti, D. G., 2014, "Single and multi camera simultaneous localization and mapping using the extended Kalman Filter", Journal of Mathematical Modelling and Algorithms in Operations Research, **13**(1), pp: 23-57.

Garrido-Jurado, S., Muñoz-Salinas, R., Madrid-Cuevas, F. J., and Medina-Carnicer, R., 2016, "Generation of fiducial marker dictionaries using Mixed Integer Linear Programming", Pattern Recognition, **51**(Supplement C), pp: 481-491. https://doi.org/10.1016/j.patcog.2015.09.023.

Guérin, F., Guinand, F., Brethé, J.-F., Pelvillain, H., and Zentout, A., 2015, "Vision based target tracking using an unmanned aerial vehicle", Proc. of Advanced Robotics and its Social Impacts (ARSO), 2015 IEEE International Workshop on, IEEE, pp: 1-6.

Borstell, H., Pathan, S., Cao, L., Richter, K., and Nykolaychuk, M., 2013, "Vehicle positioning system based on passive planar image markers", Proc. of Indoor Positioning and Indoor Navigation (IPIN), 2013 International Conference on, IEEE, pp: 1-9.

Achtelik, M., Tianguang, Z., Kuhnlenz, K., and Buss, M., 2009, "Visual tracking and control of a quadcopter using a stereo camera system and inertial sensors", Proc. of 2009 International Conference on Mechatronics and Automation, 9-12 Aug. 2009, pp: 2863-2869.

Hartley, R., and Zisserman, A., 2004, "Epipolar geometry and the fundamental matrix", Multiple View Geometry in Computer Vision, Cambridge University Press, pp: 239-261.

ISO, 1989, "Tolerances for linear and angular dimensions without individual tolerance indications (ISO 2768-1)," https://www.iso.org/standard/7748.html.

Ida, T., Takahashi, H., Marin, M., and Ghourabi, F., 2007, "Modeling origami for computational construction and beyond", Proc. of International Conference on Computational Science and Its Applications, Springer, pp: 653-665.

Bradski, G., 2000, "The OpenCV Library", Dr. Dobb's Journal of Software Tools. citeulike-article-id:2236121.

Zhang, Z., 2000, "A flexible new technique for camera calibration", IEEE Transactions on pattern analysis and machine intelligence, **22**(11), pp: 1330-1334.

Golub, G. H., and Van Loan, C. F., 2012, Matrix computations, vol. 3, JHU Press.

Schweighofer, G., and Pinz, A., 2006, "Robust pose estimation from a planar target", IEEE transactions on pattern analysis and machine intelligence, **28**(12), pp: 2024-2030.

Horn, B. K., 1987, "Closed-form solution of absolute orientation using unit quaternions", Journal of the Optical Society of America A, **4**(4), pp: 629-642.

Familton, J. C., 2015, "Quaternions: a history of complex noncommutative rotation groups in theoretical physics", arXiv preprint arXiv:1504.04885.

Thomas, F., 2014, "Approaching dual quaternions from matrix algebra", IEEE Transactions on Robotics, **30**(5), pp: 1037-1048.

Eggert, D. W., Lorusso, A., and Fisher, R. B., 1997, "Estimating 3-D rigid body transformations: a comparison of four major algorithms", Machine vision and applications, **9**(5-6), pp: 272-290.

Chegdani, F., Takabi, B., Tai, B. L., El Mansori, M., and Bukkapatnam, S. T., 2018, "Thermal Effects on Tribological Behavior in Machining Natural Fiber Composites", Procedia Manufacturing, **26**, pp: 305-316.

Chegdani, F., Wang, Z., El Mansori, M., and Bukkapatnam, S. T., 2018, "Multiscale tribo-mechanical analysis of natural fiber composites for manufacturing applications", Tribology International, **122**, pp: 143-150.

Holbery, J., and Houston, D., 2006, "Natural-fiber-reinforced polymer composites in automotive applications", Jom, **58**(11), pp: 80-86.

Al-Oqla, F. M., and Sapuan, S., 2014, "Natural fiber reinforced polymer composites in industrial applications: feasibility of date palm fibers for sustainable automotive industry", Journal of Cleaner Production, **66**, pp: 347-354.

Ramulu, M., 1997, "Machining and surface integrity of fibre-reinforced plastic composites", Sadhana, **22**(3), pp: 449-472.

Herrera-Franco, P., and Valadez-Gonzalez, A., 2005, "A study of the mechanical properties of short natural-fiber reinforced composites", Composites Part B: Engineering, **36**(8), pp: 597-608.

Ku, H., Wang, H., Pattarachaiyakoop, N., and Trada, M., 2011, "A review on the tensile properties of natural fiber reinforced polymer composites", Composites Part B: Engineering, **42**(4), pp: 856-873. https://doi.org/10.1016/j.compositesb.2011.01.010.

Nassar, M. M., Arunachalam, R., and Alzebdeh, K. I., 2017, "Machinability of natural fiber reinforced composites: a review", Int J Adv Manuf Technol, **88**(9-12), pp: 2985-3004.

Chegdani, F., and El Mansori, M., 2018, "Mechanics of material removal when cutting natural fiber reinforced thermoplastic composites", Polymer Testing, **67**, pp: 275-283.

De Rosa, I. M., Santulli, C., and Sarasini, F., 2009, "Acoustic emission for monitoring the mechanical behaviour of natural fibre composites: A literature review", Composites Part A: Applied Science and Manufacturing, **40**(9), pp: 1456-1469. https://doi.org/10.1016/j.compositesa.2009.04.030.

Herrera-Franco, P., and Valadez-Gonzalez, A., 2004, "Mechanical properties of continuous natural fibre-reinforced polymer composites", Composites Part A: applied science and manufacturing, **35**(3), pp: 339-345.

Romhány, G., Karger ‐ Kocsis, J., and Czigány, T., 2003, "Tensile fracture and failure behavior of thermoplastic starch with unidirectional and cross ‐ ply flax fiber reinforcements", Macromolecular Materials and Engineering, **288**(9), pp: 699-707.

Babu, G. D., Babu, K. S., and Gowd, B. U. M., 2013, "Effect of machining parameters on milled natural fiber-reinforced plastic composites", J. Adv. Mech. Eng, **1**, pp: 1-12.

George, J., Sreekala, M., and Thomas, S., 2001, "A review on interface modification and characterization of natural fiber reinforced plastic composites", Polymer Engineering & Science, **41**(9), pp: 1471-1485.

Valadez-Gonzalez, A., Cervantes-Uc, J. M., Olayo, R., and Herrera-Franco, P. J., 1999, "Effect of fiber surface treatment on the fiber–matrix bond strength of natural fiber reinforced composites", Composites Part B: Engineering, **30**(3), pp: 309-320. https://doi.org/10.1016/S1359-8368(98)00054-7.

Teti, R., Jemielniak, K., O'Donnell, G., and Dornfeld, D., 2010, "Advanced monitoring of machining operations", CIRP Annals-Manufacturing Technology, **59**(2), pp: 717-739.

Chegdani, F., Mezghani, S., El Mansori, M., and Mkaddem, A., 2015, "Fiber type effect on tribological behavior when cutting natural fiber reinforced plastics", Wear, **332**, pp: 772-779.

Lee, D.-E., Hwang, I., Valente, C. M., Oliveira, J., and Dornfeld, D. A., 2006, "Precision manufacturing process monitoring with acoustic emission", International Journal of Machine Tools and Manufacture, **46**(2), pp: 176-188.

Uehara, K., and Kanda, Y., 1984, "Identification of chip formation mechanism through acoustic emission measurements", CIRP Annals-Manufacturing Technology, **33**(1), pp: 71-74.

Bhuiyan, M. S. H., Choudhury, I. A., and Nukman, Y., 2012, "An innovative approach to monitor the chip formation effect on tool state using acoustic emission in turning", International Journal of Machine Tools and Manufacture, **58**, pp: 19-28. https://doi.org/10.1016/j.ijmachtools.2012.02.001.

Margueres, P., Meraghni, F., and Benzeggagh, M., 2000, "Comparison of stiffness measurements and damage investigation techniques for a fatigued and post-impact fatigued GFRP composite obtained by RTM process", Composites Part A: Applied Science and Manufacturing, **31**(2), pp: 151-163.

Davidovitz, M., Mittelman, A., Roman, I., and Marom, G., 1984, "Failure modes and fracture mechanisms in flexure of Kevlar-epoxy composites", J Mater Sci, **19**(2), pp: 377-384.

Mizutani, Y., Nagashima, K., Takemoto, M., and Ono, K., 2000, "Fracture mechanism characterization of cross-ply carbon-fiber composites using acoustic emission analysis", Ndt & E International, **33**(2), pp: 101-110.

Dornfeld, D., and Kannatey-Asibu, E., 1980, "Acoustic emission during orthogonal metal cutting", International Journal of Mechanical Sciences, **22**(5), pp: 285-296.

Kannatey-Asibu, E., and Dornfeld, D. A., 1981, "Quantitative relationships for acoustic emission from orthogonal metal cutting", Journal of Engineering for Industry, **103**(3), pp: 330-340.

Kamarthi, S. V., Kumara, S. R., and Cohen, P. H., 1995, "Wavelet representation of acoustic emission in turning process", Proc. of The 1995 Artificial Neural Networks in Engineering (ANNIE'95),St. Louis, Missouri, USA, ASME, pp: 861-866.

Pittner, S., Kamarthi, S. V., and Gao, Q., 1998, "Wavelet networks for sensor signal classification in flank wear assessment", Journal of Intelligent Manufacturing, **9**(4), pp: 315-322.

Pittner, S., and Kamarthi, S. V., 1999, "Feature extraction from wavelet coefficients for pattern recognition tasks", IEEE Transactions on pattern analysis and machine intelligence, **21**(1), pp: 83-88.

Bukkapatnam, S. T., Kumara, S. R., and Lakhtakia, A., 2000, "Fractal estimation of flank wear in turning", Journal of dynamic systems, measurement, and control, **122**(1), pp: 89-94.

Rao, P., Bukkapatnam, S., Beyca, O., Kong, Z. J., and Komanduri, R., 2014, "Real-time identification of incipient surface morphology variations in ultraprecision machining process", Journal of Manufacturing Science and Engineering, **136**(2), pp: 021008.

Kannatey-Asibu Jr, E., and Dornfeld, D., 1982, "A study of tool wear using statistical analysis of metal-cutting acoustic emission", Wear, **76**(2), pp: 247-261.

Chang, D.-C., and Bukkapatnam, S., 2004, "Towards characterizing the microdynamics of AE generation in machining", Machining science and technology, **8**(2), pp: 235-261.

Bukkapatnam, S., and Chang, D.-C., 2005, "A statistical mechanistic model of acoustic emission generation in shear zone of machining", Transactions of NAMRI/SME, **33**, pp: 597-604.

Arul, S., Vijayaraghavan, L., and Malhotra, S., 2007, "Online monitoring of acoustic emission for quality control in drilling of polymeric composites", Journal of materials processing technology, **185**(1-3), pp: 184-190.

Velayudham, A., Krishnamurthy, R., and Soundarapandian, T., 2005, "Acoustic emission based drill condition monitoring during drilling of glass/phenolic polymeric composite

using wavelet packet transform", Materials Science and Engineering: A, **412**(1), pp: 141-145. https://doi.org/10.1016/j.msea.2005.08.036.

Hase, A., Wada, M., Koga, T., and Mishina, H., 2014, "The relationship between acoustic emission signals and cutting phenomena in turning process", Int J Adv Manuf Technol, **70**(5-8), pp: 947-955.

Menze, B. H., Kelm, B. M., Masuch, R., Himmelreich, U., Bachert, P., Petrich, W., and Hamprecht, F. A., 2009, "A comparison of random forest and its Gini importance with standard chemometric methods for the feature selection and classification of spectral data", BMC bioinformatics, **10**(1), pp: 213.

Bukkapatnam, S. T., Kumara, S. R., and Lakhtakia, A., 1999, "Local eigenfunctions based suboptimal wavelet packet representation of contaminated chaotic signals", IMA Journal of Applied Mathematics, **63**(2), pp: 149-162.

Bukkapatnam, S. T., Kumara, S., and Lakhtakia, A., 1999, "Analysis of acoustic emission signals in machining", Journal of manufacturing science and engineering, **121**(4), pp: 568-576.

Iquebal, A. S., Bukkapatnam, S. T. S., and Srinivasa, A., 2017, "Change detection in complex dynamical systems using intrinsic phase and amplitude synchronization", arXiv preprint arXiv:1701.00610.

Liaw, A., and Wiener, M., 2002, "Classification and regression by randomForest", R news, **2**(3), pp: 18-22.

Botcha, B., Rajagopal, V., Babu N, R., and Bukkapatnam, S. T. S., 2018, "Process-machine interactions and a multi-sensor fusion approach to predict surface roughness in cylindrical

plunge grinding process", Procedia Manufacturing, **26**, pp: 700-711. https://doi.org/10.1016/j.promfg.2018.07.080.

Arumugam, J., Bukkapatnam, S. T., Narayanan, K. R., and Srinivasa, A. R., 2016, "Random forests are able to identify differences in clotting dynamics from kinetic models of thrombin generation", PloS one, **11**(5), pp: e0153776.

Afrin, K., Illangovan, G., Srivatsa, S. S., and Bukkapatnam, S. T., 2018, "Balanced Random Survival Forests for Extremely Unbalanced, Right Censored Data", arXiv preprint arXiv:1803.09177.

Wu, D., Jennings, C., Terpenny, J., Gao, R. X., and Kumara, S., 2017, "A comparative study on machine learning algorithms for smart manufacturing: tool wear prediction using random forests", Journal of Manufacturing Science and Engineering, **139**(7), pp: 071018.

Wambua, P., Ivens, J., and Verpoest, I., 2003, "Natural fibres: can they replace glass in fibre reinforced plastics?", composites science and technology, **63**(9), pp: 1259-1264.

Mahdi, M., and Zhang, L., 2001, "A finite element model for the orthogonal cutting of fiber-reinforced composite materials", Journal of materials processing technology, **113**(1-3), pp: 373-377.

Eriksen, E., 1999, "Influence from production parameters on the surface roughness of a machined short fibre reinforced thermoplastic", International Journal of Machine Tools and Manufacture, **39**(10), pp: 1611-1618. https://doi.org/10.1016/S0890-6955(99)00017-6.

Nazmdar Shahri, M., Yousefi, J., Fotouhi, M., and Ahmadi Najfabadi, M., 2016, "Damage evaluation of composite materials using acoustic emission features and Hilbert transform", Journal of Composite Materials, **50**(14), pp: 1897-1907.

Park, J.-M., Son, T. Q., Jung, J.-G., and Hwang, B.-S., 2006, "Interfacial evaluation of single Ramie and Kenaf fiber/epoxy resin composites using micromechanical test and nondestructive acoustic emission", Composite Interfaces, **13**(2-3), pp: 105-129.

Ramulu, M., Kim, D., and Choi, G., 2003, "Frequency analysis and characterization in orthogonal cutting of glass fiber reinforced composites", Composites Part A: Applied Science and Manufacturing, **34**(10), pp: 949-962.

Kaelble, D., 1973, "Theory and Analysis of Fracture Energy in Fiber Reinforced Composites", The Journal of Adhesion, **5**(3), pp: 245-264.

Wells, J., and Beaumont, P., 1985, "Debonding and pull-out processes in fibrous composites", J Mater Sci, **20**(4), pp: 1275-1284.

Alves Fidelis, M. E., Pereira, T. V. C., Gomes, O. d. F. M., de Andrade Silva, F., and Toledo Filho, R. D., 2013, "The effect of fiber morphology on the tensile strength of natural fibers", Journal of Materials Research and Technology, **2**(2), pp: 149-157. https://doi.org/10.1016/j.jmrt.2013.02.003.

Chegdani, F., Mezghani, S., and El Mansori, M., 2015, "Experimental study of coated tools effects in dry cutting of natural fiber reinforced plastics", Surface and Coatings Technology, **284**, pp: 264-272.

Shubhra, Q. T., Alam, A., and Quaiyyum, M., 2013, "Mechanical properties of polypropylene composites: A review", Journal of thermoplastic composite materials, **26**(3), pp: 362-391.

Khalil, H. P. S. A., Ismail, H., Rozman, H. D., and Ahmad, M. N., 2001, "The effect of acetylation on interfacial shear strength between plant fibres and various matrices",

European Polymer Journal, **37**(5), pp: 1037-1045. https://doi.org/10.1016/S0014-3057(00)00199-3.

Hsueh, C.-H., 1990, "Interfacial debonding and fiber pull-out stresses of fiber-reinforced composites", Materials Science and Engineering: A, **123**(1), pp: 1-11. https://doi.org/10.1016/0921-5093(90)90203-F.

Nimdum, P., and Renard, J., 2012, "Use of acoustic emission to discriminate damage modes in carbon fibre reinforced epoxy laminate during tensile and buckling loading", Proc. of 15th European Conference on Composite Materials (ECCM 15),Venice, Italy, p. 8p.

De Groot, P. J., Wijnen, P. A. M., and Janssen, R. B. F., 1995, "Real-time frequency determination of acoustic emission for different fracture mechanisms in carbon/epoxy composites", Composites Science and Technology, **55**(4), pp: 405-412. https://doi.org/10.1016/0266-3538(95)00121-2.

Park, J.-M., Kim, P.-G., Jang, J.-H., Wang, Z., Hwang, B.-S., and DeVries, K. L., 2008, "Interfacial evaluation and durability of modified Jute fibers/polypropylene (PP) composites using micromechanical test and acoustic emission", Composites Part B: Engineering, **39**(6), pp: 1042-1061. https://doi.org/10.1016/j.compositesb.2007.11.004.

Peças, P., Carvalho, H., Salman, H., and Leite, M., 2018, "Natural fibre composites and their applications: a review", Journal of Composites Science, **2**(4), pp: 66.

Hollaway, L., and Head, P., 2000, "Composite materials and structures in civil engineering", Comprehensive Composite Materials, Elsevier Ltd, pp: 489-527.

Barry, J., Byrne, G., and Lennon, D., 2001, "Observations on chip formation and acoustic emission in machining Ti–6Al–4V alloy", International Journal of Machine Tools and Manufacture, **41**(7), pp: 1055-1070.

Bukkapatnam, S. T., Kumara, S. R., and Lakhtakia, A., 1999, "Analysis of acoustic emission signals in machining", Journal of manufacturing science and engineering, **121**(4), pp: 568-576.

Kelly, A., and Zweben, C., 2000, Comprehensive Composite Materials, Elsevier Ltd.

Chung, J., Gulcehre, C., Cho, K., and Bengio, Y., 2014, "Empirical evaluation of gated recurrent neural networks on sequence modeling", arXiv preprint arXiv:1412.3555.

Hochreiter, S., and Schmidhuber, J., 1997, "Long short-term memory", Neural computation, **9**(8), pp: 1735-1780.

François, C., 2015, "Keras", GitHub repository.

Stathakis, D., 2009, "How many hidden layers and nodes?", International Journal of Remote Sensing, **30**(8), pp: 2133-2147.

APPENDIX-A

ALGORITHM PSEUDOCODE FOR VISION-BASED MONITORING APPROACH

ALGORITHM PSEUDOCODE

For folding sequence n=1 to N

Select crease $l(n)$ and determine the facets M_k and M_t affected by the nth folding, i.e. $\mathcal{F}_n = \{M_k, M_t\}$;

Apply defocused laser beam on crease $l(n)$;

Initialize $\mathcal{C}$ cameras

$fr \leftarrow 0$;

$\hat{\theta}_{\mathcal{F}_n}^{(fr)} \leftarrow \vartheta_{\mathcal{F}_n}^{0}$;

While $\hat{\theta}_{\mathcal{F}_n}^{(fr)} < \vartheta_{\mathcal{F}_n}^{\tau}$ **do**

Extract the frth frame image from each camera;

For c=c_1 to $c_{\mathcal{C}}$

For $j = 1\ to\ J$

Detected vertices of marker m_j, $p_i = (u_i, v_i)$ in the image plane. $(i = 1\ to\ 4)$;

Find the optimal solution Π that minimizes the negative loglikelihood as stated in Eq. 8 using the Levenberg-Marquardt algorithm;

Extract the camera pose in terms of R and T from the optimal solution Π using QR decomposition;

Generate the projections $[P_{m_j,i,c}]$'s from camera c by Eq. 1;

End j

End c

APPENDIX-B

38 EXPERIMENTS OF THE AE RECORDINGS WITH DIFFERENT FIBER ORIENTATIONS AND TOOL SPEEDS

SAMPLE. NO	VELOCITY (M/MIN)	ORIENTATION (DEGREES)	EXPERIMENT (REPETITION NO.)
1	2	0	Exp-2
2			Exp-3
3		45	Exp-1
4			Exp-3
5			Exp-4
6		90	Exp-1
7	4	0	Exp-1
8			Exp-2
9			Exp-3
10		45	Exp-1
11		90	Exp-1
12	6	0	Exp-1
13			Exp-2
14		45	Exp-1
15			Exp-2
16			Exp-3
17		90	Exp-1

18	8	0	Exp-1
19			Exp-2
20			Exp-3
21		45	Exp-1
22			Exp-2
23			Exp-3
24		90	Exp-1
25	10	0	Exp-1
26			Exp-2
27			Exp-3
28		45	Exp-1
29			Exp-2
30			Exp-3
31		90	Exp-1
32	12	0	Exp-1
33			Exp-2
34			Exp-3
35		45	Exp-1
36			Exp-2
37			Exp-3
38		90	Exp-1